

2018

Biomechanical Models of Human Upper and Tracheal Airway Functionality

Don Nadun Kuruppumullage
University of Central Florida



Part of the [Mechanical Engineering Commons](#)

Find similar works at: <https://stars.library.ucf.edu/etd>

University of Central Florida Libraries <http://library.ucf.edu>

This Doctoral Dissertation (Open Access) is brought to you for free and open access by STARS. It has been accepted for inclusion in Electronic Theses and Dissertations, 2004-2019 by an authorized administrator of STARS. For more information, please contact STARS@ucf.edu.

STARS Citation

Kuruppumullage, Don Nadun, "Biomechanical Models of Human Upper and Tracheal Airway Functionality" (2018). *Electronic Theses and Dissertations, 2004-2019*. 5828.
<https://stars.library.ucf.edu/etd/5828>



BIOMECHANICAL MODELS OF HUMAN UPPER AND TRACHEAL AIRWAY
FUNCTIONALITY

by

DON NADUN SACHINTHAKA KURUPPUMULLAGE
B.S. University of Moratuwa, Sri Lanka, 2010

A dissertation submitted in partial fulfillment of the requirements
for the degree of Doctor of Philosophy
in the Department of Mechanical and Aerospace Engineering
in the College of Engineering and Computer Science
at the University of Central Florida
Orlando, Florida

Spring Term
2018

Major Professor: Olusegun Ilegbusi

© 2018 DON NADUN SACHINTHAKA KURUPPUMULLAGE

ABSTRACT

The respiratory tract, in other words, the airway, is the primary airflow path for several physiological activities such as coughing, breathing, and sneezing. Diseases can impact airway functionality through various means including cancer of the head and neck, Neurological disorders such as Parkinson's disease, and sleep disorders and all of which are considered in this study. In this dissertation, numerical modeling techniques were used to simulate three distinct airway diseases: a weak cough leading to aspiration, upper airway patency in obstructive sleep apnea, and tongue cancer in swallow disorders. The work described in this dissertation, therefore, divided into three biomechanical models, of which fluid and particulate dynamics model of cough is the first. Cough is an airway protective mechanism, which results from a coordinated series of respiratory, laryngeal, and pharyngeal muscle activity. Patients with diminished upper airway protection often exhibit cough impairment resulting in aspiration pneumonia. Computational Fluid Dynamics (CFD) technique was used to simulate airflow and penetrant behavior in the airway geometry reconstructed from Computed Tomography (CT) images acquired from participants. The second study describes Obstructive Sleep Apnea (OSA) and the effects of dilator muscular activation on the human retro-lingual airway in OSA. Computations were performed for the inspiration stage of the breathing cycle, utilizing a fluid-structure interaction (FSI) method to couple structural deformation with airflow dynamics. The spatiotemporal deformation of the structures surrounding the airway wall was predicted and found to be in general agreement with observed changes in luminal opening and the distribution of airflow from upright to supine posture. The third study describes the effects of cancer of the tongue base on tongue motion during swallow. A three-dimensional biomechanical model was developed and used to calculate the spatiotemporal deformation of the tongue under a sequence of movements which simulate the oral stage of swallow.

ACKNOWLEDGMENTS

- Foremost, I would like to express my sincerest acknowledgment to my advisor, Prof. Dr. Olusegun Ilegbusi. His mentorship, wisdom and constant guidance through five years of my Ph.D. life were the key driving force behind this dissertation. I sincerely owe to him for my intellectual gains and knowledge I learned during these years.
- I would also like to sincerely acknowledge my co-advisor Prof. Dr. Bari Hoffman Ruddy for making me understand the physiological aspects of the research project and giving vital suggestions during the meetings.
- Special thanks go to my Ph.D. committee members: Prof. Dr. Alain Kassab, Prof. Dr. Faisal Moshely, Prof. Dr. Hansen Mansy, and Prof. Dr. Anand Santhanam for serving in my committee.
- I owe special gratitude for Dr. Kingman Strohl for his suggestions and support in Sleep Apnea research. Without his support, this research would not have completed.
- I would also like to thanks my colleagues, Amir Roullahi and Sreesarin Vasu Sumathi for providing me a good office environment with their good mood and humor. I would also thank my former colleagues Dr. Behnaz Sefy Noeforest, Dr. Navid Khatami and Fuad Ismaylov for making years at Biomedical Process Modeling Lab at UCF truly fun and enjoyable.
- I would like to thank my family, especially mom, dad, brother, and sister-in-law for their constant love, motivation and unlimited support throughout my education.
- Special word of affection goes to my sister, Dr. Prabhani Kuruppumullage for support, motivation and the belief in me.

TABLE OF CONTENTS

LIST OF FIGURES	x
LIST OF TABLES	xiv
CHAPTER 1: INTRODUCTION	1
1.1 Motivation	1
1.2 Research Objectives	3
1.3 Dissertation Structure and Approaches	4
CHAPTER 2: LITERATURE REVIEW	7
2.1 Overview	7
2.2 Anatomy and Physiology of Upper Airway and Airway Tract.....	7
2.2.1 Airflow Dynamics in Upper Airway and Airway Tract	9
2.3 Cough	10
2.3.1 Physiology of Cough	10
2.3.2 Biomechanical Modeling of Cough.....	13
2.3.3 Cough Strength Evaluation.....	15
2.4 Obstructive Sleep Apnea.....	16
2.4.1 Physiology of Obstructive Sleep Apnea.....	16
2.4.2 Biomechanical Modeling of Obstructive Sleep Apnea	17
2.5 Swallow	18
2.5.1 Physiology of Swallow	18

2.5.2 Biomechanical Modeling of Swallow	20
2.6 Summary	21
CHAPTER 3: MODELING COUGH IN TRACHEAL AIRWAY.....	23
3.1 Overview	23
3.2 Materials and Methods	23
3.2.1 Biomechanical Model.....	23
3.2.2 Parametric Study.....	28
3.3 Results	31
3.3.1 Velocity Distribution	31
3.3.2 Penetrant Trajectory	32
3.3.3 Penetrant Break-up	35
3.4 Discussion	38
3.4.1 Airflow Velocity.....	38
3.4.2 Penetrant Trajectory	39
3.4.3 Penetrant Break-up Pattern.....	40
3.5 Summary	42
CHAPTER 4: MODELING COUGH AND AIRWAY CLEARANCE IN THE AIRWAY WITH WALL REMODELING	43
4.1 Overview	43
4.2 Materials and Methods	43
4.2.1 Geometry Reconstruction and Mesh Generation.....	43

4.2.2 Governing Equations for Fluid Flow	46
4.2.3 Penetrant Dynamics	48
4.2.4 Design of Penetrant Study	51
4.2.5 Initial and Boundary Conditions.....	52
4.2.6 Airway Wall Remodeling	54
4.2.7 Monitored Locations.....	55
4.2.8 Assessment of Aspiration Risk.....	56
4.2.9 Computational Details	57
4.3 Results and Discussion.....	58
4.3.1 Velocity Distribution	58
4.3.2 Penetrant Trajectory	61
4.3.3 Penetrant Behaviour Outcome.....	66
4.3.4 Assessment of Modeling improvements.....	68
4.4 Summary	70
 CHAPTER 5: MODELING DROPLETS BREAKUP UNDER COUGH IN HUMAN	
AIRWAY	71
5.1 Overview	71
5.2 Materials and Methods	71
5.2.1 Formulation of Droplets Behavior in Cough Flow.....	71
5.2.2 Design of Droplet Study	72
5.3 Results	73

5.3.1 Droplet Breakup Characteristics.....	73
5.4 Discussion	77
5.4.1 Droplet Characteristics	77
5.5 Summary	78
CHAPTER 6: FINITE ELEMENT MODEL OF OBSTRUCTIVE SLEEP APNEA WITH MUSCULAR COUPLING	79
6.1 Overview	79
6.2 Materials and Methods	80
6.2.1 Reconstruction of Relevant Upper Airway Anatomy.....	80
6.2.2 Mathematical Formulation	82
6.2.3 Material Properties	84
6.2.4 Boundary and Loading Conditions.....	86
6.2.5 Computational Details	87
6.3 Results	88
6.4 Sensitivity Analysis.....	94
6.4.1 Structural Deformation	95
6.4.2 Airflow.....	95
6.5 Discussion	96
CHAPTER 7: MATHEMATICAL MODELLING OF TONGUE DEFORMATION IN ORAL PHASE OF SWALLOW IN PATIENTS WITH HEAD AND NECK CANCER....	100
7.1 Overview	100

7.2 Materials and Methods	101
7.2.1 Reconstruction of Three-Dimensional Tongue Geometry	101
7.2.2 Mathematical Formulation	102
7.2.3 Material Properties	105
7.2.4 Loading and Boundary Conditions.....	107
7.2.5 Representation of Localized Cancer.....	109
7.2.6 Computational Details	110
7.2.7 Mesh Sensitivity Analysis	111
7.3 Results	112
7.4 Discussion	118
CHAPTER 8: CONCLUSIONS AND FUTURE WORK.....	122
8.1 Summary of Chapters.....	122
8.2 Challenges and Future Direction.....	124
8.2.1 Improvements to Cough CFD Model	124
8.2.2 Improvements to Obstructive Sleep Apnea Model.....	125
8.2.3 Improvements to Swallow Model.....	126
APPENDIX: AUTHOR’S BIOGRAPHY	127
REFERENCES	129

LIST OF FIGURES

Figure 1: Regions of the respiratory system	8
Figure 2: A typical cough profile of a human subject	11
Figure 3: The four stages of swallow [4]: oral preparatory stage (a); oral stage (b); pharyngeal stage (c); and esophageal stage (d)	19
Figure 4: Reconstruction of airway geometry showing sagittal and coronal planes of CT image.....	24
Figure 5: Mesh generated for the airway geometry and used for numerical computation	25
Figure 6: Airway geometry indicating inlet and outlet boundary surfaces and other landmarks	28
Figure 7: Cough waveform obtained from human subject and used as input data for the simulation.....	29
Figure 8: Four simulated cases used	31
Figure 9: Predicted velocity magnitude at the level of the vocal folds.....	32
Figure 10: Predicted trajectories of liquid penetrants released at P1 above the larynx	33
Figure 11: Penetrant trajectories for two penetrants (P6: anterior and P5: posterior)	35
Figure 12: Predicted fate of liquid penetrant released from location P5 for Case showing cough-induced disintegration into small droplets	36
Figure 13: A droplet break-up event visualized at 6 instances	37
Figure 14: Droplet diameter variation.....	38
Figure 15: The reconstructed airway geometry in sagittal plane, and final geometry.....	44
Figure 16: Mesh generated in the airway geometry.....	45
Figure 17: The mesh skewness histogram	46
Figure 18: Locations of the penetrant ejection at the laryngeal vestibule level.....	51

Figure 19: Cough profiles used in this study	53
Figure 20: Airway geometry with inlet and outlet boundary surfaces.....	53
Figure 21: Airway wall deformation.....	55
Figure 22: Vertical plane (a), seven monitored locations in the airway (b)	56
Figure 23: Decision-making criteria used in PAS score defined by (a) airway depth; and (b) schematic of numerical values	57
Figure 24: Predicted velocity magnitude for strong cough event	58
Figure 25: Predicted velocity magnitude for weak cough event.....	59
Figure 26: Predicted velocity magnitude with time at 6 monitored locations	59
Figure 27: Predicted velocity magnitude with time at 6 monitored locations	61
Figure 28: Predicted penetrant trajectory of six penetrants under strong cough (Penetrant diameter = 1mm, density = 500 kg/m ³).....	62
Figure 29: Predicted penetrant trajectory of six penetrants under weak cough (Penetrant diameter = 1mm, density = 500 kg/m ³).....	62
Figure 30: Monitored Parameters for Penetrant P5	63
Figure 31: Comparison of velocity distribution in two airway geometries	68
Figure 32: Variation of velocity magnitude at three locations within the airway for rigid and deforming walls	69
Figure 33: Droplet breakup under a strong cough	74
Figure 34: Droplet breakup under a weak cough.....	75
Figure 35: Droplet diameter variation under a strong cough event	76
Figure 36: Droplet diameter variation under a weak cough event.....	76
Figure 37: CT scan of the midsagittal plane representing airway structure and the reconstructed upper airway anatomy	81

Figure 38: Finite Element meshes used for the FE model	82
Figure 39: Time-Force activation of the genioglossus in the simulation.....	86
Figure 40: Predicted dimensional changes in the width of airway lumen at four reference levels. The width was measured in a lateral plane between the posterior wall of the oropharynx and the relevant anterior structure of the airway	89
Figure 41: Predicted displacement magnitude in millimeters for three cases: (a) standing position; (b) deformed structure due to gravity in the supine position; (c) recovery with dilator muscle activation.	90
Figure 42: Hyoid bone highlighted in black before activation (a), Hyoid bone elevated during activation (b). Two horizontal reference lines are drawn to show the relative movement of the hyoid bone without and with activation.....	91
Figure 43: Predicted velocity magnitude in meters per second for three cases: (a) standing position; (b) deformed airway due to gravity in the supine position; (c) recovery with dilator muscle activation. The highest velocity magnitude is represented by the red.....	92
Figure 44: Predicted pressure magnitude in cmH ₂ O for three cases: (a) standing position; (b) deformed structure due to gravity in the supine position; (c) recovery with dilator muscle activation.....	94
Figure 45: Steps involved in reconstruction of 3D tongue geometry	101
Figure 46: volumetric mesh generated (a), and cut-out view (b).....	102
Figure 47: Stress-strain curves used for the three parametric cases considered in the study	107
Figure 48: Applied stress at different sections of tongue surface during propulsion stage of swallowing	108
Figure 49: schematic sketch indicating sections of tongue surface on which pressure or fixity is applied	109

Figure 50: Schematic sketch indicating location of localized cancer in (a) external view, and (b) sagittal view.....	110
Figure 51: Displacement of tongue tip for different mesh sizes.....	112
Figure 52: Predicted evolution of tongue deformation during propulsion stage of swallowing for normal tongue (Case 1)	113
Figure 53: Predicted evolution of tongue deformation during propulsion stage of swallowing for tongue with mild cancer (Case 2).....	114
Figure 54: Predicted evolution of tongue deformation during propulsion stage of swallowing for tongue with severe cancer (Case 3).....	114
Figure 55: Predicted tongue deformation from initial rest state to intermediate state at $t = 100\text{ms}$ for normal tongue (Case 1), tongue with mild cancer (Case 2) and tongue with severe cancer (Case 3).....	115
Figure 56: Three monitored locations on the tongue	116
Figure 57: Displacement at three monitored locations for three cases: Case 1 (no cancer), Case 2 (early-stage cancer) and Case 3 (late-stage cancer)	117

LIST OF TABLES

Table 1: Penetrant trajectory outcomes and evaluated indices (Key: R-Retained in airway, E-Escaped to oral cavity, and A-Aspirated to lungs)	34
Table 2: Input parameters used for the penetrant study	61
Table 3: Parametric study of penetrant size (diameter variation) under strong cough event ..	64
Table 4: Parametric study of penetrant size (diameter variation) under weak cough event	65
Table 5: Drag force on penetrant under strong cough event.....	66
Table 6: Drag force on penetrant under weak cough event	66
Table 7: Penetrant trajectory outcome for penetrant diameter variation under strong cough event.....	67
Table 8: Penetrant trajectory outcome for penetrant diameter variation under weak cough event.....	67
Table 9: Penetrant trajectory outcome for penetrant density variation under strong cough event.....	67
Table 10: Penetrant trajectory outcome for penetrant density variation under weak cough event.....	68
Table 11: Summary of the Droplet Study	77
Table 12: Material constants used in the computation for hyperelastic model of soft tissues.	85
Table 13: Airflow rate evaluated for three cases with the 2D model	93
Table 14: Sensitivity analysis for deformation assessed as change in airway width at tongue level.....	95
Table 15: Sensitivity analysis for air flow rate assessed at a location close to the center of the airway lumen at epiglottis level	96
Table 16: Material constants used in the computation (values in kPa).....	107

Table 17: Details of meshes used for sensitivity analysis.....111

Table 18: Predicted maximum displacement at three monitored locations on the tongue117

CHAPTER 1: INTRODUCTION

1.1 Motivation

The purpose of this chapter is to introduce the biomechanical models developed and applied to three distinct upper and tracheal airway diseases. The functionality and diseases of the airway diseases were investigated by simulating flow-particulate and structural dynamics in the airway. We have focused on three physiological functions: (i) cough; (ii) airway patency in obstructive sleep apnea; and (iii) swallow. Each physiological function was considered with an associated chronic disease such as aspiration in cough, obstructive sleep apnea in breathing, and cancer of the head and neck in swallow.

Cough:

Cough is a corrective mechanism of airway protection that uses high velocity, high volume air flows to produce a shearing effect that forcibly removes foreign matter from the lower airways. It is a response to the presence of unwanted penetrants in the lower airways, producing high-velocity air flow that clears the aspirate and mucus from the airway. Typically the particulate is entrained and transported in the mucus layer lining the inner surface of the airway. The contraction of the trachea further enhances the shearing air flow under cough. Failure to protect the lungs from unwanted penetrants and excessive mucus exert catastrophic consequences to health and quality of life. Over 60,000 Americans die as a result of conditions relating to deficient airway protection which is mostly from aspiration pneumonia, i.e., inability to expel penetrants. Cough airflow is a complex multiphase system involving the interaction and transport of airflow, a viscoelastic surface layer of mucus, and particulates. These observations underscore the significance of research directed toward understanding the fundamental scientific principles involved in cough flow-particulate interaction and dynamics of the airway.

Airway Patency in Obstructive Sleep Apnea (OSA):

Obstructive Sleep Apnea (OSA) is characterized by repeated occlusion of the oropharyngeal airway during sleep and can have a significant impact on quality of life. OSA is extremely problematic as breathing disruption results in decreased oxygen delivery to the body's tissues, causing long-term damage to vital organs. Additionally, people with OSA can experience significant fatigue from the associated sleep disturbance and exhibit the reduced quality of life, restricting their social activities. Various aetiologies can cause OSA. These include anatomical and physiological variables of the head and neck, obesity, inherent neck mass, hypertension, narrow airway, chronic nasal congestion, diabetes, being male, being African-American, age, family history, smoking, and alcohol use among some other extrinsic and intrinsic factors. The cause for the OSA is weakening of dilator forces responsible for both passive and active muscle contraction (e.g., genioglossus) in the pharyngeal airway. The dilator muscles have an important function in the maintenance of upper airway patency during sleep by maintaining tongue position and oropharyngeal patency during sleep. The anatomic elements for neuromechanical control are known, but the degree of detail needed to predict and individualize pathogenesis and therapy is lacking.

Swallow:

Normal swallow facilitates safe transfer of food and liquid through the oropharynx and into the digestive tract while simultaneously preventing this material from invading the lower airways. Disordered swallowing or dysphagia represents a failure of this preventative mechanism of airway protection and is common in patients with head and neck cancer (HNC), potentially resulting in respiratory illness and lower self-reported quality of life. A recent report indicated 59% of patients with HNC demonstrate dysphagia symptoms. The presence of dysphagia in

those with HNC likely contributes to high observed rates of aspiration pneumonia (directly implicated in 19% of fatalities) in this population. Fatigue, shortness of breath, sensory loss, and reduced tongue strength all increase the risk of developing dysphagia that is characterized by reduced laryngeal displacement during swallow and increased pharyngeal transit time. Dysphagia leaves the airway vulnerable to injury and infection and can exert devastating effects on overall health (including increased risk of choking, infection, malnutrition, dehydration, muscle wasting, physical debilitation, and death from asphyxia). These observations underscore the importance of research directed toward the improvement of swallow function in subjects with HNC

1.2 Research Objectives

The ultimate goal of this research is to use biomechanical modeling approach as a predictive tool to evaluate impaired airway functionality in three distinct physiological conditions. These predictive tools will improve the understanding of each function under pathological conditions. In order to achieve the stated goal, we itemize the specific objectives of the research below.

Cough

- Develop a biomechanical model for computation of spatio-temporal flow-particulate distribution under cough event.
- Predict behavior of penetrants under cough as a function of particle size, density, and texture (solid and liquid).
- Test hypothesis that the fate of liquid droplets depends on droplet size, location, and break-up pattern, as well as cough strength.
- Quantify cough strength and aspiration risk.

Sleep Apnea

- Develop and apply 2D finite element model to predict flow distribution and structural deformation of upper airway under obstructive sleep apnea with or without muscle activation.
- Investigate dimensional change in retroglossal anatomy and gain in airflow under activation of pharyngeal dilator muscles under obstructive sleep apnea.

Swallow

- Develop finite element based biomechanical model for spatio-temporal deformation of the tongue during pharyngeal phase of swallow.
- Investigate deformation change in tongue due to the effect of tissue fibrosis from head and neck cancer.

1.3 Dissertation Structure and Approaches

The following chapters of this dissertation are organized to provide the concepts, details and the implementation of the research objectives listed above. The dissertation is therefore divided into eight chapters as described below.

Chapter 1: Introduction – This chapter presents the motivation for the research, objectives and contributions made to the body of knowledge.

Chapter 2: Literature Review – This chapter provides an overview of the state-of-the-art on biomedical modeling of each of the functionalities considered in this dissertation. Mainly, it describes the upper airway anatomy and physiology, mathematical models used to describe the

physiological functions and the current knowledge of biomechanical models, and the different approaches used in biomechanical modeling.

Chapter 3: Modeling Cough in Tracheal Airway – This chapter presents a biomechanical model to simulate cough strength and aspiration. Two primary cough variables are examined to determine their impact on the characteristics that impact airway compromise.

Chapter 4: Modeling Cough and Airway Clearance in the Airway with Wall Remodeling – The focus of this chapter is the development of a biomechanical model to calculate the spatio-temporal flow-particulate behavior under cough. The materials and methods used in the model are described as well as the formulation of the biomechanical model including the governing equations and their solution. The results of the simulations are then presented and discussed in subsequent sections.

Chapter 5: Modeling Droplets Breakup under Cough in Human Airway – The objective of the chapter is to extend the cough model developed in Chapter 4 to simulate and characterize the behavior of a typical liquid penetrant droplet during a cough event. The model allows for turbulent airflow-droplet interaction and droplet collision on the surface, and droplet breakup. Two cases, a strong cough, and a weak cough, representing a patient with disorders of laryngeal function were used in comparison to characterize droplet behavior. The results of the simulations are then presented and discussed.

Chapter 6: A Finite Element Model of Obstructive Sleep Apnea with Muscular Coupling – This chapter presents a finite element-based biomechanical model of the oropharynx to capture the effects of posture change and muscular stimulation on upper airway anatomy and flow characteristics under obstructive sleep apnea.

Chapter 7: Mathematical Modelling of Tongue Deformation in Oral Phase of Swallow in Patients with Head and Neck Cancer – This Chapter presents the biomechanical model of swallow. The formulation of the biomechanical model includes the reconstruction of the 3D tongue geometry from MRI images, governing equations, and finite element analysis. The results of the simulation are then presented and discussed.

Chapter 8: Conclusion and Future Work – This Chapter concludes the dissertation by summarizing the outcomes of the research. Additionally, it presents suggested future work in each biomechanical model including the design of experimental study for model validation.

CHAPTER 2: LITERATURE REVIEW

2.1 Overview

The purpose of this chapter is to provide an overview of upper airway physiology and anatomy which would be the primary focus of this dissertation. In addition, three physiological processes; cough, swallow and obstructive sleep apnea are also described.

2.2 Anatomy and Physiology of Upper Airway and Airway Tract

The respiratory system is comprised of several components including the central nervous system, the chest wall, the pulmonary circulation, and the respiratory tract. The respiratory tract can be divided into four separate sections: the nasopharynx and oropharynx, the conducting airways, the respiratory bronchioles, and the alveoli[1]. Figure 1 shows the different regions of the respiratory systems[2]. The sections outside the chest cavity are collectively called the upper airway, and those within the chest cavity make up the lower airway tract. The lungs are considered a part of lower airway structures as they can also be divided into the conducting airways and the units of respiration. The trachea, bronchi, and bronchioles conduct and transport air from the outside world and deliver it to the alveoli. Gas exchange with the blood vessels occurs at the level of the alveoli, providing the necessary oxygen for the body's daily functions.

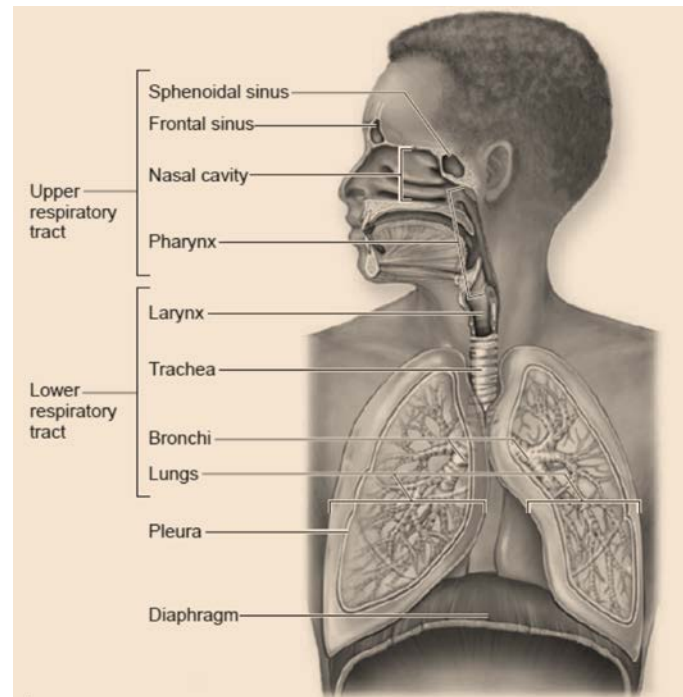


Figure 1: Regions of the respiratory system

Upper Airway Anatomy

The first section of the respiratory tract is the naso-oropharynx, which begins with the nostrils and lips, and includes the nasal passage, sinuses, and glottis until reaching the trachea. The nasal cavity and the paranasal sinuses are the primary structures that warm and humidify the air we inhale. It also filters out any large particles through contact with the respiratory epithelium and mucous covering[3]. Below the nasal cavity, the common space shared by both the respiratory system and digestive system is the pharynx. The pharynx can be divided into three compartments: (i) nasopharynx; (ii) oropharynx; and (iii) laryngopharynx[4]. The structural integrity of pharynx is important in Obstructive Sleep Apnea as airway narrowing occurs in the pharyngeal region[5].

Lower Airway Anatomy

The lower airway structures mainly contain the larynx and the conducting airways (trachea) which repeatedly branches to form approximately 14 generations of conduits for air reaching several distinct pulmonary segments. The larynx is also called the voice box which conducts air into the lower tract and produces sound [6]. The epiglottis and muscles of the larynx coordinate the passage of food and air and assure that food reaches the esophagus and air reach the trachea [2]. The trachea is a flexible, but somewhat rigid tube which bifurcates at the carina into two smaller tubes: right and left primary bronchi. It is approximately 2.5 cm in diameter and 12-14 cm in length [7]. Aspirated material is likely to go into the right main bronchus because it is wider and shorter than the left [1]. Each of the two primary bronchi leads to a bronchial tree which is a branched tree-like air-conducting passage diverging throughout the lungs.

2.2.1 Airflow Dynamics in Upper Airway and Airway Tract

The airway is the conduit that links the outside environment to the gas exchange site. This channel allows oxygen to be transported in and carbon dioxide to be transported out[8]. The process is by bulk flow [1] which allows the transfer of sufficient volumes to keep up with the needs of the body. For this flow to be maintained, the airway must be kept open. Airway patency is preserved by control of pharyngeal muscles, mucus production, mucociliary clearance, sneezing, and coughing. Flow in the airway is involuntarily controlled by the autonomic nervous system [2]. The process is complicated and loss of control can occur due to a variety of reasons including obstruction and inability to create the sub-atmospheric conditions [3].

The Flow Pattern of the Airway Tract

The airflow rate inside the airway can be simply defined using the Hagen Poiseuille's formula:

$$Q = \frac{\pi P r^2}{8 \eta l} \quad (2-1)$$

where Q is the airflow rate, P is the pressure, r is the radius of the conduit (tract), η is the air viscosity, and l is the length of the conduit. The total cross-sectional area of the airway increases from the trachea to the more distal parts which results in decrease of the linear flow velocity downstream as flow rate is constant. The linear flow velocity is the flow divided by the total cross-sectional area of a given generation of the airway. The linear flow velocity, being more sizeable in the trachea, causes the flow inside the trachea to be turbulent.

2.3 Cough

2.3.1 *Physiology of Cough*

Cough is an airway protective mechanism resulting from a coordinated series of respiratory, laryngeal, and pharyngeal muscle activity [9]. The cough aerodynamic sequence of inspiration, compression, and expulsion protects the lungs through the removal of secretions and foreign material from the upper and lower airways [10]. Weakening and slowing of the cough response, commonly observed in patients with respiratory compromise, reduces the shearing forces necessary to clear the airway, [11] potentially contributing to declines in respiratory health. In patient groups, cough impairment frequently contributes to increased risk of aspiration pneumonia, potentially hastening death [12]. Consequently, the study of cough as a process for maintaining respiratory health is of considerable importance to patient groups and is an area of increasing attention among clinicians and scientists.

The specific features of the voluntary cough airflow waveform recorded from a human subject are shown in Figure 2. During the initial (inspiratory) phase of cough, reduced alveolar pressure (relative to atmospheric pressure) results in the inhalation of air. The mean duration of the inspiratory phase varies from 0.4 to 1 sec [13-15]. The compressive phase immediately follows the initial inspiratory phase. Here, after inhaling a volume of air, the glottis closes, allowing air pressure to build up within the lower airways. During a normal compression phase, airflow ceases for approximately 0.2 s [16]. After this, the glottis opens, and the high intrathoracic pressures developed during the compressive phase of cough are released, resulting in high expiratory flow rates, and culminating in expiratory peak flow where air from the lower airways is rapidly released [16, 17]. Although a typical cough profile comprises all three phases described above, spontaneous cough events do not normally exhibit an inspiratory phase especially when laryngeal penetrants are present[18].

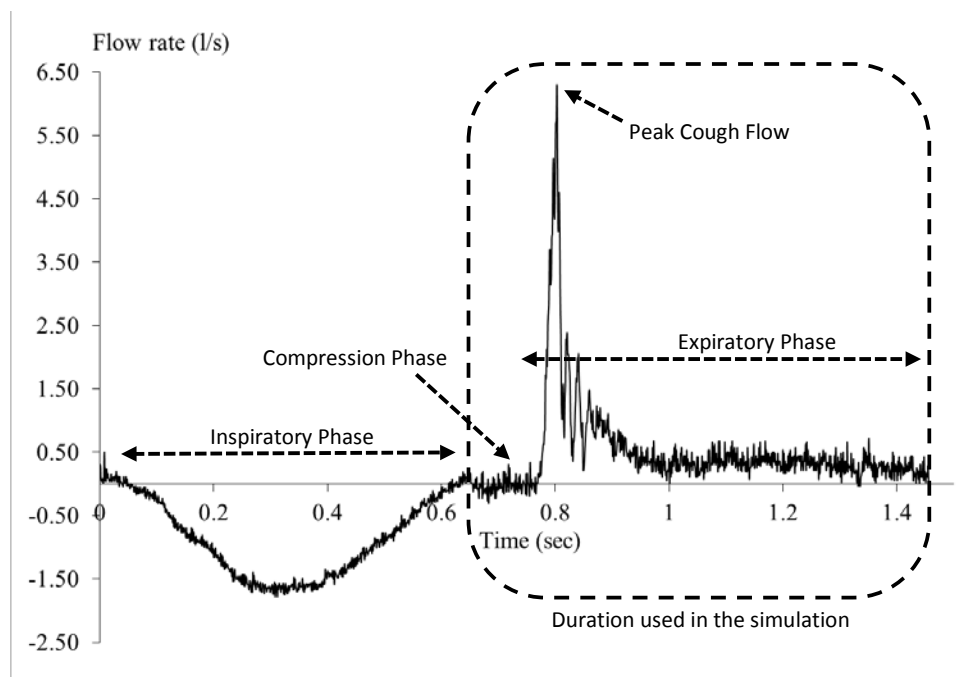


Figure 2: A typical cough profile of a human subject

An effective cough as a clearing mechanism is dependent upon the linear velocity of the airflow traveling down the airway lumen [19]. It appears that the cough mechanism is designed to significantly increase the velocity by both generating high expiratory flow rates and dynamically compressing the airways to reduce their cross-sectional area [20].

Impaired Cough and Aspiration

Impairment of the mechanisms of airway protection (including swallow and cough) is implicated in most forms of aspiration pneumonia. Patients with laryngeal/airway disorders often exhibit weakening and slowing of cough, which may result in aspiration [11, 12]. Weakening and slowing of the cough response are impacted by two parameters: the compression phase duration (CPD), which represents the period of full glottal closure immediately prior to a cough and the peak cough flow (PCF), an indirect measure of cough strength reflecting the velocity of expiratory airflow[21-23]. The weakening and slowing of cough response, commonly observed in patients with Stroke, Parkinson's disease, and cancer of the head and neck reduces the shearing forces necessary for airway clearance [24]. As a result, the foreign bodies such as food or liquid may not be expelled properly leading to aspiration pneumonia [25]. Common treatment targets for patients with reduced airway clearance focus on improving CPD and PCF. Some of these include: postural drainage, incentive spirometry, expiratory muscle strength training, percussion and vibration, manually assisted cough, huffing, and active breathing techniques. Many of these strategies include maneuvers resulting in forced expiration, creating greater "shearing" forces within the airway for the elimination of foreign material [24].

2.3.2 Biomechanical Modeling of Cough

Previous investigations have sought to characterize respiratory aerodynamics under a range of conditions such as airway obstruction or restriction. These efforts have led to the development of computational models in order to characterize the interaction between respiratory airflow and the surrounding soft tissue surfaces of the airway [20, 26], producing numerical simulations of these flows [9, 27]. Most of these studies assumed rigid walls and used approximated airway geometry despite the pliant nature of the human airways [28-30]. However, the mechanics of cough process typically results in an abrupt change in the tracheal cross-section, in some cases by up to 1/6 of its normal value in order to increase the flow velocity within the airway [15].

The transport equations governing airflow in human airways were typically solved in the context of either laminar or turbulent airflow depending on the flow condition of interest. Typically, the Reynolds number, Re , in the trachea varies from about 800 in light breathing and to about 10,000 in heavy breathing [31]. Therefore, turbulent flow modeling is widely used to characterize elevated flow conditions such heavy breathing and sniffing [32, 33]. In addition, the irregular shape and branching within the conducting zone of the airway may cause pressure drops, resulting in local turbulence spots [34]. Ma and Lutchen developed an anatomically based airway model in which flow patterns were predicted under turbulent conditions using zero-pressure outlet conditions and oscillating flow input conditions [35, 36]. The transient flows occurring during the cough process are usually considered turbulent [26, 37]. However, turbulent flow characteristics appear only during the expiratory phase of the cough where there is a rapid acceleration from the compression phase followed by a deceleration of the flow. The effect of turbulence and the transition from laminar to turbulent flow as well as relaminarization, on the airflow and particulates during cough are important phenomena that have not been fully explored.

Three major approaches are classically used for simulating such complex transitional-turbulent flows: direct numerical simulation (DNS), large-eddy simulation (LES), and Reynolds-averaged Navier–Stokes (RANS) turbulence models [38]. Although DNS is computationally expensive, it is the most accurate technique as it resolves turbulent eddies at all scales [35]. LES resolves large-scale energy containing turbulent eddies and parameterizes small-scale unresolved eddies. RANS does not resolve any turbulent eddy structures but uses turbulence models to predict the dynamics of these eddies. In certain cases, the interest is not mainly to simulate the instantaneous velocity fluctuations, but the average quantities while the effect of turbulence is modeled by RANS model selected. This results in a considerable reduction of computation time compared to DNS. The two most popular RANS turbulence models used in airway flow simulations are the k – ε , and k – ω models in which k represents turbulent kinetic energy, ε is the dissipation rate, and ω is the specific dissipation rate. Kleinstreuer C. et al demonstrated that k – ω model with Shear Stress Transport (SST) submodule can successfully simulate the turbulent effects for the flow regimes ranging from laminar to turbulent which are expected during a cough event [39]. In addition, various studies have demonstrated that k – ω SST model can accurately predict the mean velocity distributions, and the SST submodal is recommended for high accuracy boundary layer simulations[40].

Two fundamental approaches are widely used for analysis of particulate transport analysis namely, Euler-Lagrange method and Euler-Euler method [41]. In the Euler-Lagrange method, the particle trajectory is obtained by solving equations of motion for each particle. In the Euler-Euler method, the particle concentration distribution in the fluid is calculated based on the particle volume fraction [41]. The majority of previous studies on human airways have been based on the Euler-Lagrange approaches, such as the work of Zhang and Kleinstreuer [42, 43] who analyzed targeted aerosol drug deposition in a rigid triple bifurcation tracheobronchial

airway geometry. Most of these studies are based on micro and nanoparticles with a mean diameter in size range of $0.1\mu\text{m}$ - $1\mu\text{m}$ [44]. However, the size of a typical laryngeal penetrant that can be expelled during a cough event can be on the order of millimetres [45].

2.3.3 Cough Strength Evaluation

Several methods have been used to evaluate aspiration risk including aerodynamic and acoustic characteristics of cough [46-48], measuring the sound of swallow [49], pulse-oximetry [50], and ultrasonography [51, 52]. Although these techniques has been known to clinicians for a long time, they still mostly depend on the 8-point Penetration-Aspiration Score (PAS) scale evaluated from videofluoroscopy or video endoscopy, which provides a measure of the severity of aspiration [53-55]. The PAS scale is principally based on the assessment of the extent of the aspiration, and the depth of penetrant invasion. This method has been sufficiently robust to provide significant knowledge about the fate of foreign materials in the airway. The standard PAS assessment involves either videofluoroscopic swallowing study or the video endoscopy to observe aspiration in patients [55]. The examination studies are then used to classify aspiration severity by assigning a score. Such methods, however, require considerable experience on the part of the examiner and also intrude on the flow and the physiological function which may involve some risk for the patient [47]. In addition, the use of Barium as the radiological contrast material in videofluoroscopy is unnatural thus creates erroneous changes in food composition (especially viscosity). However, the invasive nature of the standard PAS score assessment leads to many limitations such as not being applicable to medically unstable patients, patients unable to be adequately positioned, patients allergic to Barium, size limitation of the patients (e.g., Infants) [56].

2.4 Obstructive Sleep Apnea

2.4.1 *Physiology of Obstructive Sleep Apnea*

Obstructive sleep apnea (OSA) results from a collapse of the upper airway during sleep. The consequences of OSA include resistant hypertension, heart failure, atrial fibrillation, diabetes, stroke and increased risk of death [57]. OSA occurs when the anatomical structures within or surrounding the airway produce a collapsing force that cannot be adequately compensated for by the pharyngeal dilator muscles [58-60]. The decline in pharyngeal neuromuscular activity during sleep in OSA patients combined with an inadequate reflex compensation results in the collapse of a vulnerable airway [61, 62]. One major site for OSA is the retro-lingual portion of the upper airway, a region that is usually described for its structural elements of the tongue and the anterior pharyngeal wall [63]. The underlying issues are the degree to which muscle activation vs. mechanical properties contributes to the disorder.

Previous studies have shown that upper airway dilator muscle activation, particularly the genioglossus, will maintain upper airway patency during sleep [64]. The genioglossus is an extrinsic muscle of the tongue located at the tongue base. This pathway has been exploited to treat OSA. Unilateral hypoglossal nerve stimulation producing a protrusion force on the tongue is a treatment technique for OSA [65]. This empirical demonstration underscores how little we know about the relative contribution of muscle activation to airway patency. The linkage of upper airway muscle activation state to airway patency may not be linear, and quantification of the relative effect of the airway surrounding tissue on the preservation of airway patency is lacking. In particular, it would be beneficial to know how to model the balance in terms of airway patency of activation pattern and mechanical set-points. This is a complex problem to address physiologically. A two-dimensional (2D) model approach has been advocated to isolate and therefore predict what anatomic and functional factors are important in causing

upper airway narrowing and collapse and how capable a neuromechanical element could be in preventing OSA from occurring [66].

2.4.2 Biomechanical Modeling of Obstructive Sleep Apnea

A number of biomechanical models have been introduced to study the motion state of the upper airway during OSA. These models can be classified into two broad categories: the lumped parameter models [32, 67] and distributed parameter models. The distributed parameter model, usually a finite element model (FEM), has recently become popular because the distribution of meaningful quantities such as velocity, pressure, deformation, and morphometry can be readily obtained. Finite element modeling has also been used in parallel to other methods such as acoustic rhinometry and endoscopy to assess the morphology of the nasal airway with and without OSA in human subjects [68]. FEM is non-invasive with more generic information compared to other morphometric techniques [68, 69], but distinct advantages in terms of prediction and virtual experiments.

Anatomical geometries can be reconstructed from imaging scans such as Computerized Tomography (CT) and Magnetic Resonance Imaging (MRI), and geometrical models with anatomic details have been adopted [70]. Estimation of regional elasticity values of complex anatomical structures is still a challenging task. In the case of the upper airway, the anatomy consists of integrated soft tissues and bone-cartilage structures with elastic properties can be difficult to quantify. In vivo experiments on cadavers have been used to estimate the elasticity of soft tissues, but cadaver tissue properties differ significantly from those of live tissues [71]. Magnetic resonance imaging has provided elastic properties non-invasively for the tongue [72] so that once developed a model with other upper airway structures like the hyoid, can be

adjusted for individual variation, rather than relying on measurements in animals or one reference value.

Some prior FEM models of upper airway often adopted rigid wall boundary conditions, which limit the models by not accounting for the coupled interaction between structural deformation of the tongue and surrounding musculature, and the channels for air flow, such as occurs with OSA and its therapy [73, 74]. More recent studies have integrated airway modeling from imaging to understand places of airway narrowing or occlusion during sleep apnea [71, 75], or have been able to demonstrate the effectiveness of OSA treatment, such as surgically implanted devices in the tongue base or mandibulomaxillary advancement, by providing quantitative descriptions of changes in structural and airway factors [76]. Although tissue kinematics and neurological information can be integrated into FEM models, such models are still at the developmental stage and consist of specific constraints and assumptions [77]. One such constraint results from the simplification of the geometry through truncation of the mandible and the interface between the thyroid cartilage and the adipose tissue [77]. In some models, the external environmental parameters such as body posture are not defined. These assumptions, constraints, and details of biomechanical models are to standardize the behavior of the system and permit comparisons among models.

2.5 Swallow

2.5.1 *Physiology of Swallow*

Normal swallowing involves rapid coordination of oral and pharyngeal structures and associated musculature in order to propel food and liquid from the oral cavity, through the pharynx, and into the esophagus [78]. The body and base of the tongue serve to both shape and propel the bolus. The presence of cancerous lesions within the tongue, as well as tissue changes

which occur as a side effect of radiation treatment, may interfere with bolus formation, transfer, and clearance [79, 80].

The swallowing process consists of four main stages as illustrated in Figure 3. The first stage is the oral preparatory phase in which the food is mixed with saliva and placed on the top surface of the tongue. The second stage is the oral phase (oral transit stage). In this stage, the food is pushed back through the mouth primarily by the tongue. The tongue moves upward and forward in this phase to create a front-to-back squeezing action. The third stage is the pharyngeal phase of swallow where the food enters the upper throat region. In this stage, the tongue moves backward and the pharyngeal wall moves forward to support food bolus as it moves down towards the esophagus. The esophageal phase is the last stage of swallow when food bolus finally enters into the esophagus.

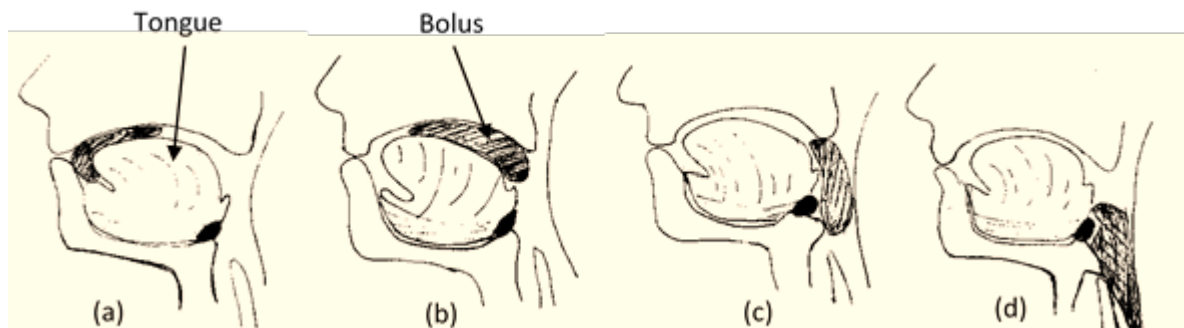


Figure 3: The four stages of swallow [4]: oral preparatory stage (a); oral stage (b); pharyngeal stage (c); and esophageal stage (d)

The tongue is a muscular organ, under voluntary control, and comprised almost entirely of skeletal muscle fibers. The tongue can be subdivided into oral and pharyngeal regions. The oral tongue includes the anterior region or tip and body or blade and terminates at the circumvallate papillae. The pharyngeal tongue is continuous with the oral division and is comprised of the

posterior region or base and extends into the pharyngeal cavity. Impaired tongue movement during the oral swallow phase can contribute to premature spillage of food or liquid into the pharyngeal cavity, potentially infiltrating the open airway prior to the onset of the swallow reflex [78, 79, 81]. Swallow changes are common in patients with tongue base cancers [82-84]. The presence of cancer itself causes fibrosis which may alter the elastic properties of the tongue base tissue, producing similar effects [85].

2.5.2 Biomechanical Modeling of Swallow

A number of studies have developed finite element numerical techniques to study the upper airway with attempts to utilize physiologically realistic boundary conditions and tongue musculature, with varying degrees of limitations. Buchaillard et al. [86] and Stavness et al. [87] describe a generic 3D biomechanical model of the tongue and the oral cavity, incorporating complex tongue muscular structure. However, the geometry was reconstructed from cadaver images, limiting the application of the results for patient-specific modeling. Some studies have introduced the motion capturing technique and physics-based modeling strategy to visualize the tongue deformation [88]. Although quite promising for representation of the physiological boundaries in speech production, such an approach has a number of limitations including the sparse placement of the mocap sensors throughout the tongue for data acquisition. Other studies provide a general mechanism for attaching rigid and deformable bodies to simulate jaw-tongue-hyoid dynamics [87]. In particular, the model provides dynamic simulations of interactions due to the motion of jaw-tongue-hyoid complex and contact phenomena. Such a model is quite useful and required for studying speech production. However, the desire to better understand the dynamics of upper airway structures has led many scientists to develop biomechanical model of individual structures in the oral, pharyngeal and laryngeal complex for analysis of observed organ dysfunction such as dysphagia (swallow dysfunction).

Any material mechanics, especially tissue material mechanics, can be quite complex and many assumptions must be made when deriving constitutive properties. It is impossible to derive a particular constitutive equation that would accurately model all aspects of tissue behavior under all types of loading conditions. This is because tissues may behave very differently under small loads as compared to large loads. In linear elastic models, the material deforms linearly due to prescribed loading. Past efforts at modeling the elastic properties of tongue tissue include the assumption of non-linear hyperelastic material [84] because the hyper-elastic model has been found to best approximate tongue elasticity [87]. Therefore the tongue tissues are considered to be hyper-elastic material. The biomechanical models also typically use finite element numerical analysis to simulate tongue deformation under specified loading conditions. The loading is typically applied in two ways. The first method assigns muscular force properties to the generation of tongue movements [89]. These muscle-activated models are defined by the respective contributions of both intrinsic and extrinsic tongue musculature, thus necessitating the use of muscle activation data obtained through electromyography (EMG). The second method of assigning loading parameters is to apply traction (pressure) to the surface of the tongue. This approach has the advantage of not requiring discreet identification of tongue muscle tissue.

2.6 Summary

The rapid development of computational power, advancement in medical imaging, and integration of multiple engineering principles such as fluid-structure interaction and particulate dynamics have opened new avenues to the field of biomechanical modeling which provides cost-effective, non-invasive techniques for simulating various biological processes. The visualization of biomechanical models allows us to precisely predict three distinct airway

diseases: weak cough leading to aspiration, upper airway patency in obstructive sleep apnea, and tongue cancer in swallow disorders, which are difficult to accomplish in a clinical setting. It is desirable to know more about how and how well, materials of varying properties are transported within the airway. Other important information include: what the necessary conditions are, and how and where they arise; what can impair the operation of the each mechanism; what are the consequences of impairment; and what can be done about the impairment under these physiological activities. Biomechanical modeling may provide a means of addressing these issues systematically.

Identified Gaps:

1. The effect of turbulence and the transition from laminar to turbulent flow as well as relaminarization, on the airflow and particulates during cough are important phenomena that have not been fully explored.
2. Quantification of the relative effect of the airway surrounding tissue on the preservation of airway patency is lacking.
3. The behavior of large particles and droplets in airways under cough event has not been addressed.
4. The effect of dilator muscle activation on sleep apnea in upper airway has not been addressed
5. The effect of head and neck cancer within tongue on swallow mechanics has not been addressed.

CHAPTER 3: MODELING COUGH IN TRACHEAL AIRWAY¹

3.1 Overview

A Computational Fluid Dynamics (CFD) technique was used to simulate fluid flow within a tracheal airway geometry reconstructed from patient CT images. The model utilized a finite-volume numerical scheme to simulate cough-induced airflow, allowing for turbulent particle interaction, collision, and break-up. Liquid penetrants injected at 8 anatomical locations were tracked during the simulated cough. Cough flow velocity was computed for a base case and four simulated cases. Air-way clearance was evaluated through assessment of the fate of particles in the airway following a simulated cough. Patients with laryngeal disorders often exhibit changes to cough function contributing to aspiration episodes. Two primary cough variables (peak cough flow: PCF and compression phase duration: CPD) were examined within a biomechanical model to determine their impact on characteristics that impact airway compromise.

3.2 Materials and Methods

3.2.1 *Biomechanical Model*

The representative 3D airway geometry was constructed from computed tomography (CT) scan images. The image was segmented in order to extract the 3D geometry of the upper airway associated with a cough event, by use of “MIMICS”, a widely applied medical image segmentation software[90]. After segmentation, the reconstructed geometry was divided into small finite volumes or cells called meshes by use of 3-MATIC[91] commercial software code.

¹ *The materials of this Chapter have been previously published in:* Hoffman Ruddy, Bari, et al. "Computational Modelling of Cough Function and Airway Penetrant Behavior in Patients with Disorders of Laryngeal Function." *Laryngoscope investigative otolaryngology* 2.1 (2017): 23-29.

Due to the irregular airway geometry, an unstructured mesh system was used to allow mapping of the exact shape. Figure 4 shows the reconstruction process of the airway geometry.

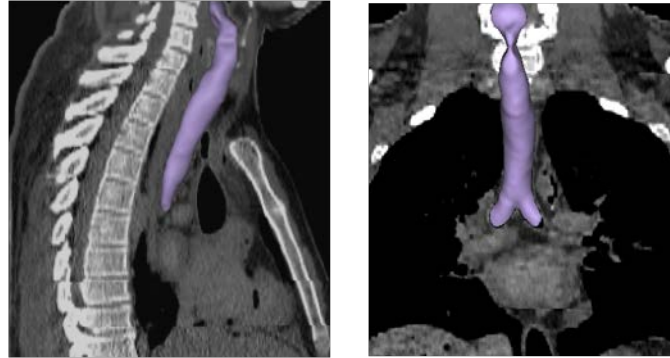


Figure 4: Reconstruction of airway geometry showing sagittal and coronal planes of CT image

A combination of triangular (surface mesh), and tetrahedral (volume mesh) elements were used to capture the geometrical features. The number of faces, vertices and mesh cells used in the study were 837223, 2425705, and 810665 respectively. A grid-independence test was first performed using three different grid sizes (~ 600000 , 800000 , and 1000000 cells) in order to ensure the accuracy of the results. The computed results were found to be essentially independent of the grid size beyond 800000 cells, and this grid structure was used for all results presented in the chapter. Figure 5 shows the mesh generated and used for this study.

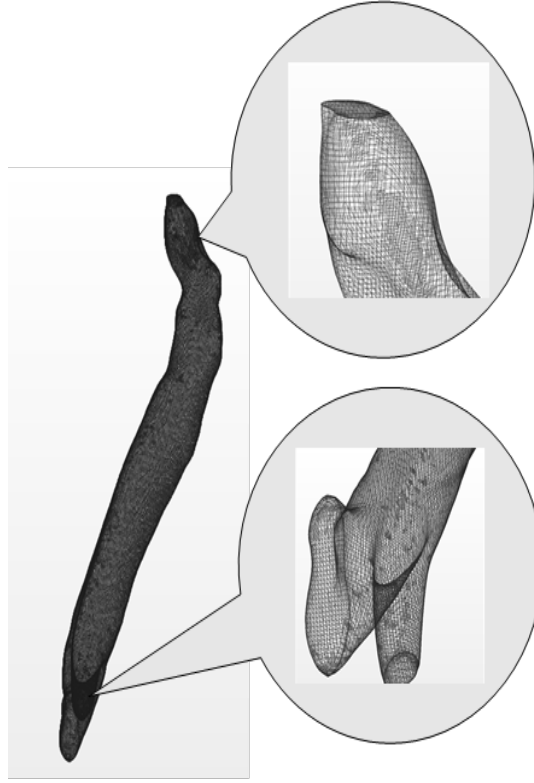


Figure 5: Mesh generated for the airway geometry and used for numerical computation

The equations governing fluid flow and particulate dynamics were integrated over the finite volumes generated by means of STARCCM+ commercial software[92]. The equations governing fluid flow and particulate dynamics are then integrated over the finite volumes generated by means of STARCCM+ commercial software.¹⁷ The equations are derived from physical laws expressing conservation of mass, and conservation of momentum for both the fluid and particulates.

Conservation of Mass

This is based on the principle that the mass of the fluid remains unchanged as it flows through the airway, and can be expressed thus:

$$\sum_{in} \dot{m} = \sum_{out} \dot{m} \quad (3-1)$$

where \dot{m} is the mass flow rate (in kg/s), the left hand side represents total mass inflow into a cell, and the right hand side is total mass outflow from the cell.

Conservation of Momentum

This is the Newton's second law of motion, which states that the sum of all external forces (body and surface forces) acting on a fluid element equals the rate of change of momentum (product of mass and acceleration of fluid). This equation is expressed thus:

$$\sum F_{body} + \sum F_{surface} = \rho \cdot \Delta v \cdot \frac{Du}{Dt} \quad (3-2)$$

where F is force, ρ is density of fluid, Δv is volume of fluid, and Du/Dt is acceleration.

Particle force balance: Dynamics of penetrant particle in the cough flow are governed by Newton's second law of motion expressed by the following force balance equation:

$$\rho_p \cdot V_p \cdot \frac{du_p}{dt} = \sum F_n \quad (3-3)$$

where ρ_p is particulate density, V_p is volume of particle, u_p is its velocity. The left hand side is the rate of change of momentum of the particle and the right hand side is the sum of all forces acting on the particle. More details of the formulation of the governing equations of fluid have been presented in previous studies thus the droplet transport equations, and the formulation for droplet breakup phenomena are presented in Chapter 4 and 5 (next two chapters).

Gas density and temperature are assumed to be constant. The laminar-turbulent transitional nature of cough flow is accounted for by use of appropriate turbulence model for calculation of the surface force in the momentum equation [19, 93, 94]. Three major approaches are typically used for simulating such transitional flows: direct numerical simulation (DNS), large-eddy simulation (LES), and Reynolds-averaged Navier–Stokes (RANS) models [95]. The k- ω

shear stress transport turbulence (SST) model in which k is the turbulent kinetic energy and ω is the specific dissipation rate has been adopted in this study because DNS or LES turbulence models are computationally intensive. Also, the k - ω SST model has been successfully used for transitional flows and represents an adequate compromise between computational intensity and accuracy [44].

The locations of individual particles are tracked while being transported through the fluid in the airway, a method known as Lagrangian approach [96]. The particle-dynamics equation is augmented by a sub-model allowing for possible droplet break-up, collision and coalescence. The underlying mechanism is that the surface tension and viscous forces inside the droplet resist its deformation [97, 98]. The governing equations are solved subject to appropriate boundary and initial conditions relevant to cough. Figure 6 shows the airway geometry indicating the inlet and outlet boundaries and the other upper airway landmarks used. The outlet is defined at the top surface of the airway geometry where zero gage pressure is imposed relative to atmospheric pressure. This approach expresses the fact that the mouth is typically open during cough. A voluntary cough waveform (see Figure 7) obtained from a human subject was applied at the inlet defined at the two (bifurcation) interfaces between the trachea and the lungs.

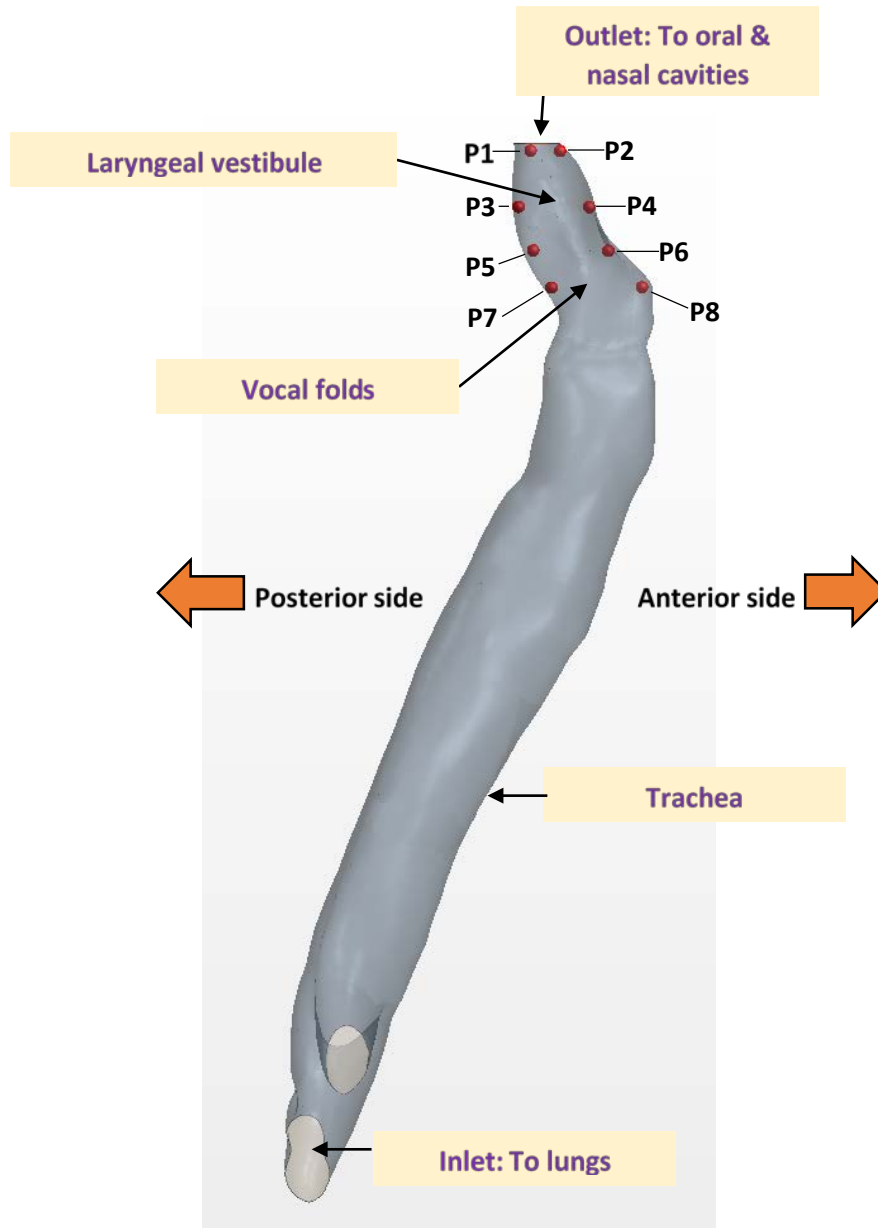


Figure 6: Airway geometry indicating inlet and outlet boundary surfaces and other landmarks

3.2.2 Parametric Study

A key objective of this study was to assess the effect of two cough parameters: compression phase duration (CPD) and peak cough flow (PCF), which determine the quality of cough strength. Although a typical voluntary cough has three phases: inspiratory, compression, and expiratory, most patients do not inspire prior to cough when a laryngeal penetrant is present

[99]. Therefore, for the purpose of this study, the simulation was started from the compression phase of cough as shown in Figure 7.

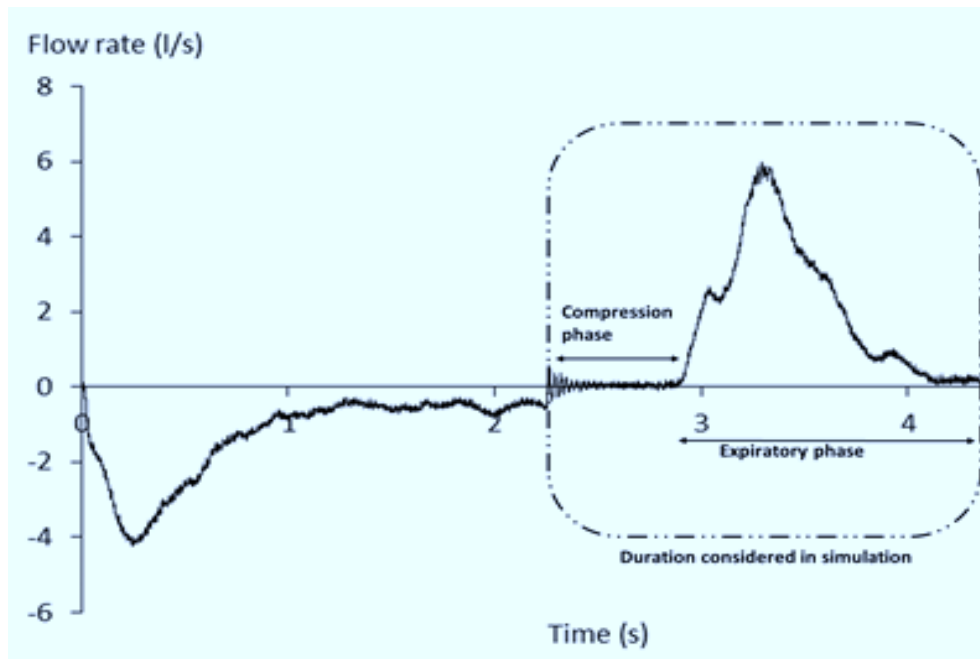


Figure 7: Cough waveform obtained from human subject and used as input data for the simulation

Liquid droplet penetrants were considered to have the properties of a ‘thin liquid’ e.g. water. The droplet penetrants were introduced at four different landmarks (levels) along the laryngeal section of the airway as shown in Figure 6. The laryngeal section of the airway possesses abundant sensory innervation, which can activate to produce cough [100]. These landmarks represented the levels of the laryngeal vestibule, above the laryngeal vestibule, vocal folds and above the vocal folds where cough receptors are located [101]. For the purpose of this simulation study, a single droplet penetrant with 4mm diameter was introduced at each level of both the anterior and posterior walls of the airway. The stickiness of the airway wall due to the presence of mucus was represented in the biomechanical model through a wall restitution

parameter, which typically ranges from zero (complete stickiness) to 1.0 (no stickiness). For this study we adopted a value of 0.1 in order to allow for a possible mucus-induced high degree of stickiness [102].

In order to establish the effects on the penetrants of the key parameters considered (airflow velocity distribution, penetrant trajectory and penetrant break-up pattern), a simulated dataset was first generated. A number of studies have shown the effect of PCF and CPD in different population groups. Specifically, Pitts et al. (2008) have shown that the penetration/aspiration groups with Parkinson's disease produce significantly longer CPD time [103]. Also, Kulnik et al. (2016) has found that higher PCF lowers the risk of pneumonia in acute stroke [104]. The percentage change associated with PCF and CPD in these studies vary significantly according to the population considered. Therefore, our study is designed to represent all possibilities associated with the key parameters considered. The base case represents an impaired voluntary cough from a human subject. Four cases (Cases 1 to 4), were then generated by changing both the compression phase duration (CPD) and peak cough flow (PCF) $\pm 40\%$ [105]. Case 1 demonstrates both CPD and PCF as decreased by 40% compared to the base case, Case 2 demonstrates the CPD reduced by 40% with an increase of PCF of 40%. Case 3 and Case 4 simulate a 40% increase to CPD with a corresponding PCF decrease of 40% in Case 3 and increase of 40% in Case 4. Figure 8 shows the simulated flow profiles for all four cases.

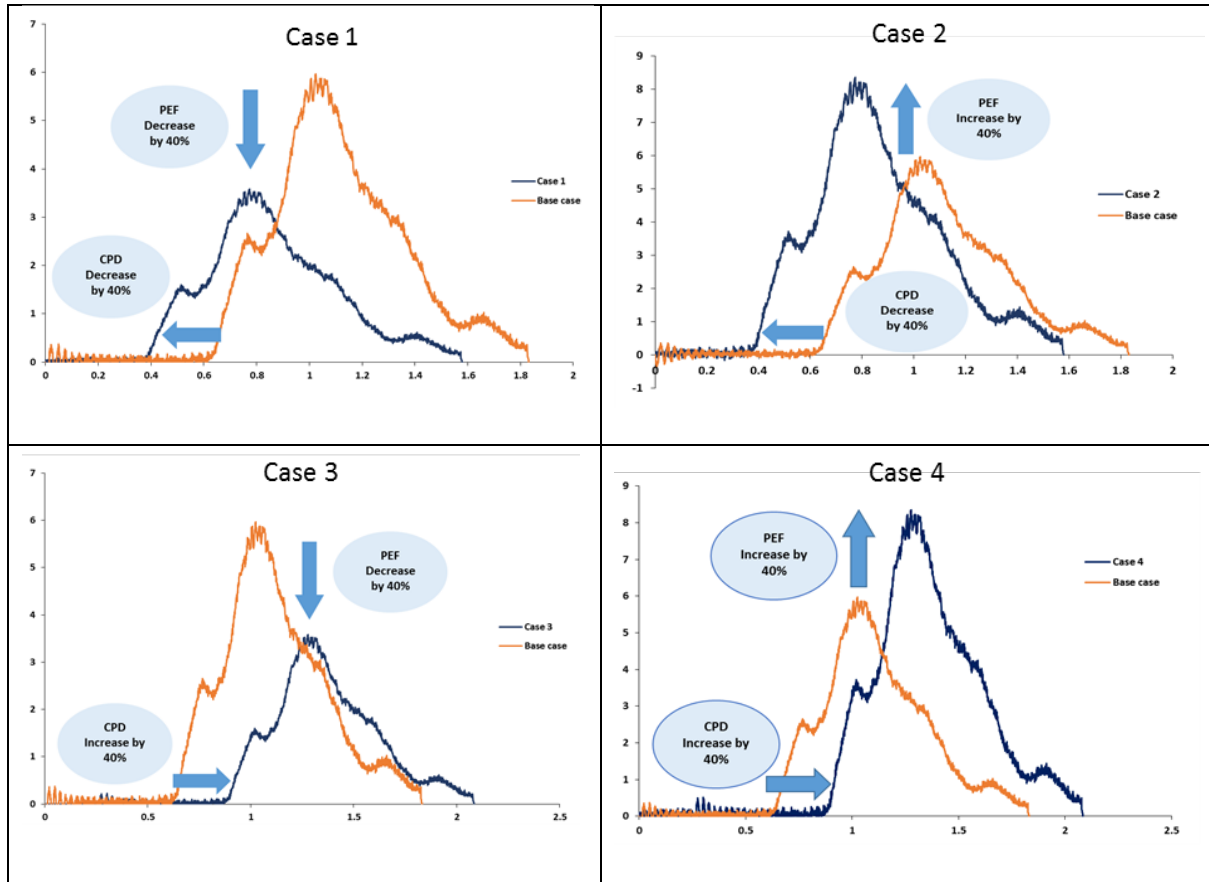


Figure 8: Four simulated cases used

3.3 Results

The results of this study can be evaluated based on three specific parameters; the velocity distribution, the penetrant trajectory and the pattern of break-up of the penetrant once exposed to the cough event.

3.3.1 Velocity Distribution

The predicted transient variation of velocity at the level of the vocal folds for the base case and four simulated cases (Case 1- 4) are presented in Figure 9. In all cases, the highest velocity was observed at the peak expiratory flow. The highest velocity predicted for these cases was 49.96m/s, 88m/s, and 117 m/s (Case 1 and 3, Base case, and Case 2 & 4) respectively. As

demonstrated in Figure 9, the predicted transient velocity pattern followed the same profile as the flow rate.

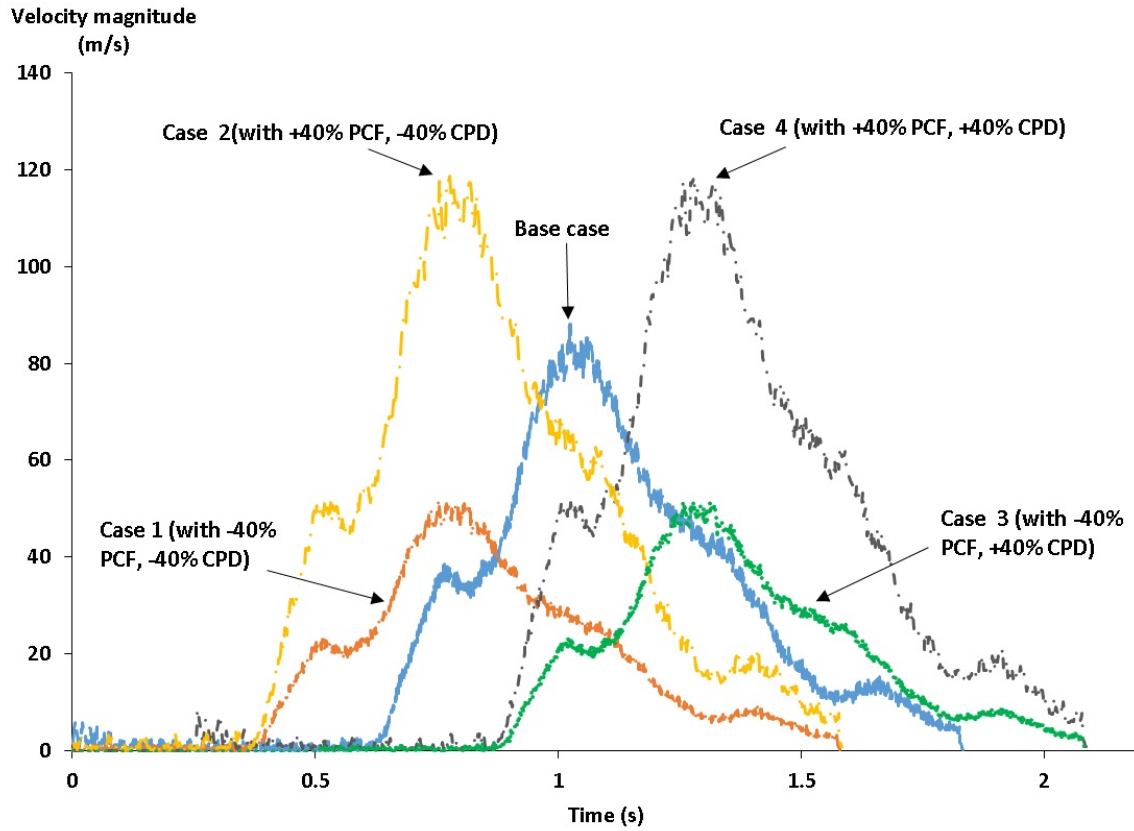


Figure 9: Predicted velocity magnitude at the level of the vocal folds

3.3.2 Penetrant Trajectory

Figure 10 shows the trajectories of penetrants released at location P1 for the base case and 4 simulated cases considered in the study. P1 is located on the posterior side of the airway above the laryngeal vestibule. The real-time duration of the simulation (T_s) in each case from the instant of release is also shown in Figure 21. The final location of the penetrant is indicated as F_P in each figure.

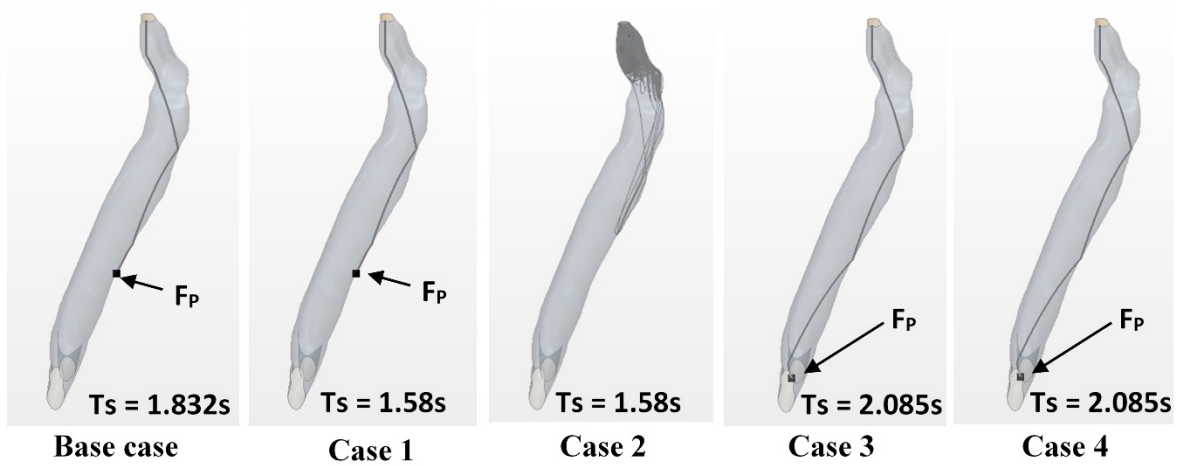


Figure 10: Predicted trajectories of liquid penetrants released at P1 above the larynx

The results indicate that the penetrant was retained in the airway in all cases except Case 2. For cases 3 and 4, the prolonged CPD resulted in the penetrant falling further down the airway before the expiratory phase. If the penetrant traveled to the lung-end of the airway, it was considered ‘aspirated.’ The trajectory of penetrants considered in all cases is summarized in Table 1. The three major outcomes predicted in the study are identified by the letters *E* (for particles that have escaped from the airway to the oral cavity), *R* for particles retained in the airway, and *A* for those aspirated to the lungs. We define three indices that may quantify aspiration, retention, and clearance of penetrants. For our model, we have assumed that cough is considered a success if penetrants are cleared from the laryngeal airway. Likewise, cough is considered as ‘in need of a sequential cough’ if penetrants are retained. The last parameter defines a cough ‘failure’ if penetrants are aspirated.

Table 1: Penetrant trajectory outcomes and evaluated indices (Key: R-Retained in airway, E-Escaped to oral cavity, and A-Aspirated to lungs)

Penetrant	Base case	Case 1	Case 2	Case 3	Case 4
P1	R	R	E	R	A
P2	R	E	R	R	E
P3	E	R	E	R	E
P4	R	A	R	A	A
P5	E	E	E	E	E
P6	R	A	R	A	A
P7	A	E	E	A	A
P8	A	A	R	A	A
<i>success index</i> $= \frac{\text{number of escaped penetrants}}{\text{total number of penetrants}}$	0.25	0.375	0.5	0.125	0.375
<i>need of sequential cough (NSC) index</i> $= \frac{\text{number of retained penetrants}}{\text{total number of penetrants}}$	0.5	0.25	0.5	0.375	0
<i>failure index</i> = 1 – (success + NSC)	0.25	0.375	0	0.5	0.625

In the base case, 25% of the penetrants escaped into the laryngeal airway. The highest percentage (50%) of penetrants escaping into the airway were observed in Case 2 (with -40% CPD, +40% PCF), while only 12.5% escaped in Case 3 (with +40% CPD, -40% PCF). The proportion that escaped in Cases 1 and 4 was 37.5%. The results of the penetrant trajectories provided in Table 1 reveal that penetrant P5 was successfully cleared from the airway in all simulated cases, while P4, P6 and P8 (introduced from the anterior airway) were not. Figure 11 shows the difference in penetrant trajectory for the same level when introduced anteriorly versus posteriorly.

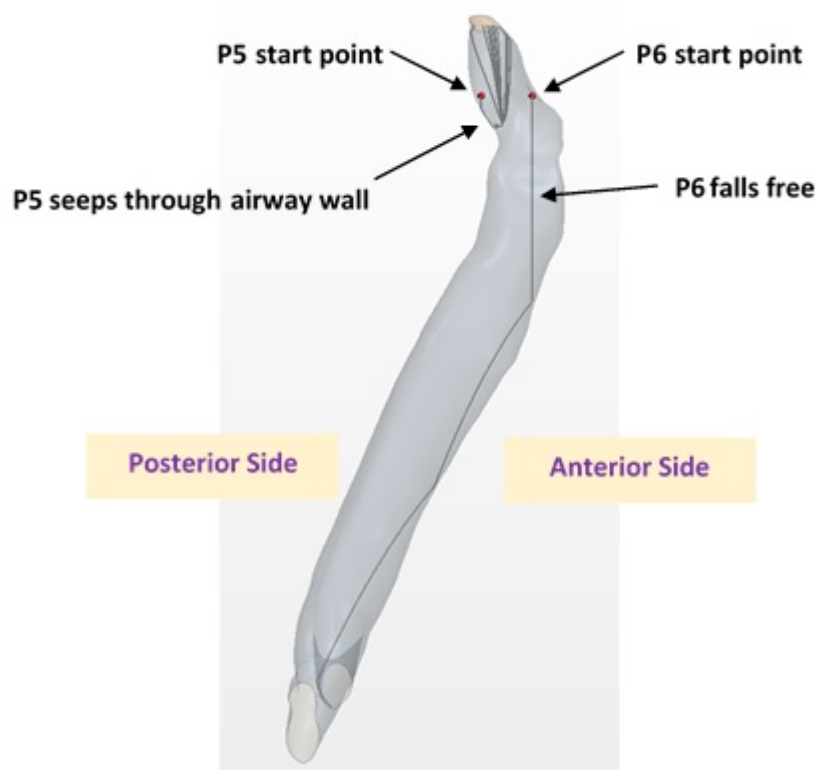


Figure 11: Penetrant trajectories for two penetrants (P6: anterior and P5: posterior)

3.3.3 Penetrant Break-up

An example of a penetrant break-up event within the airway is presented for location P5 in Case 3 (Figure 12). The penetrant released at location P5 was predicted to creep down the wall

of the airway due to gravity during the compression phase. Once the expiratory phase is initiated, the penetrant is disturbed by the exchange of momentum with the increasing airflow, resulting in disintegration of the droplet into small (child) droplets. The number of child droplets created during this ‘break-up’ event depends on several factors: 1) the droplet resident location, 2) the relative speed of the air flow, 3) the initial droplet size, and 4) the surface tension. The results presented in Figure 12 were obtained using the best estimates of these parameters and are considered to be only illustrative of droplet behaviour at this stage of the study.

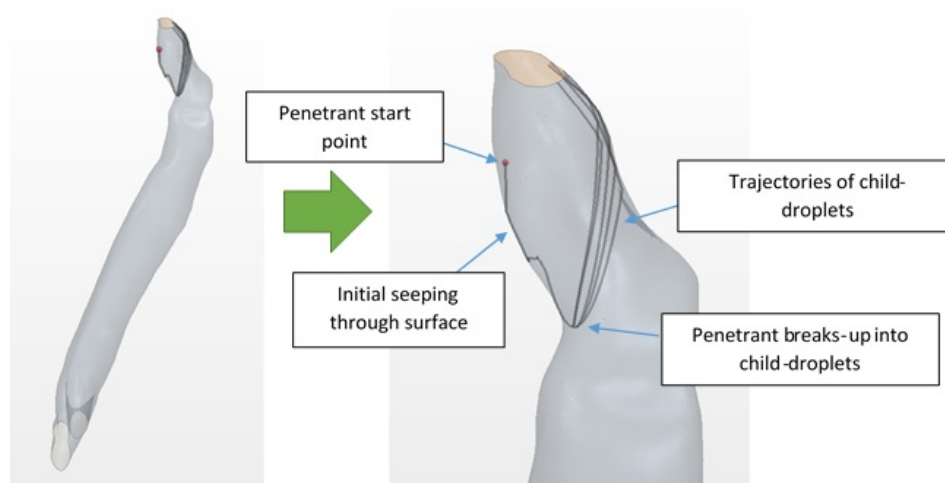


Figure 12: Predicted fate of liquid penetrant released from location P5 for Case showing cough-induced disintegration into small droplets

Figure 13 models six instances where the droplet break-up event is visualized using representative spherical particles for the penetrant P5 considered in Figure 13, based on the simulation. The real-time duration after cough initiation is shown in time steps of 0.001s from 1.180s to 1.185s. The penetrant is initially represented as one droplet, which upon subsequent interaction with the flow velocities of about 40 m/s, breaks up into small droplets. These child

droplets then travel up the airway towards the mouth-end. This process is illustrated in Figures 13(b) to 13(f). It should be noted that the child droplet trajectories and velocities are different from each other as they travel along the airway.

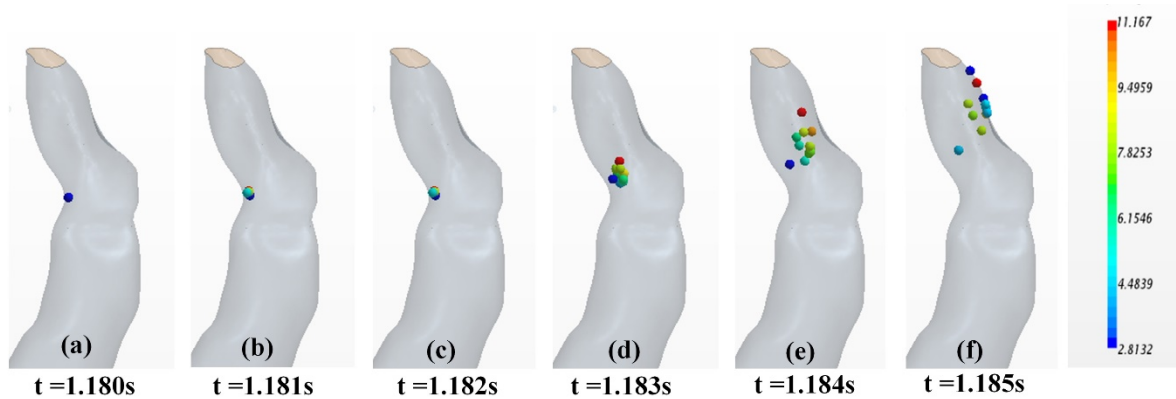


Figure 13: A droplet break-up event visualized at 6 instances

Figure 14 shows how the mean diameter of the penetrant changes during its residence within the airway for the time steps corresponding to those in Figure 13. At the first breakup event, the creation of child-droplets reduces the mean diameter of the liquid penetrant from initial 4 mm to 0.91mm. The mean diameter is subsequently reduced to 0.38mm as a result of the second break-up event at 1.183s. While travelling through the airway, some of these child-droplets may also collide and coalesce with each other due to change in the flow characteristics to form new droplets. Such coalescence may increase the mean diameter of the child droplet as predicted at 1.185s, and the new mean diameter is now 0.62mm.

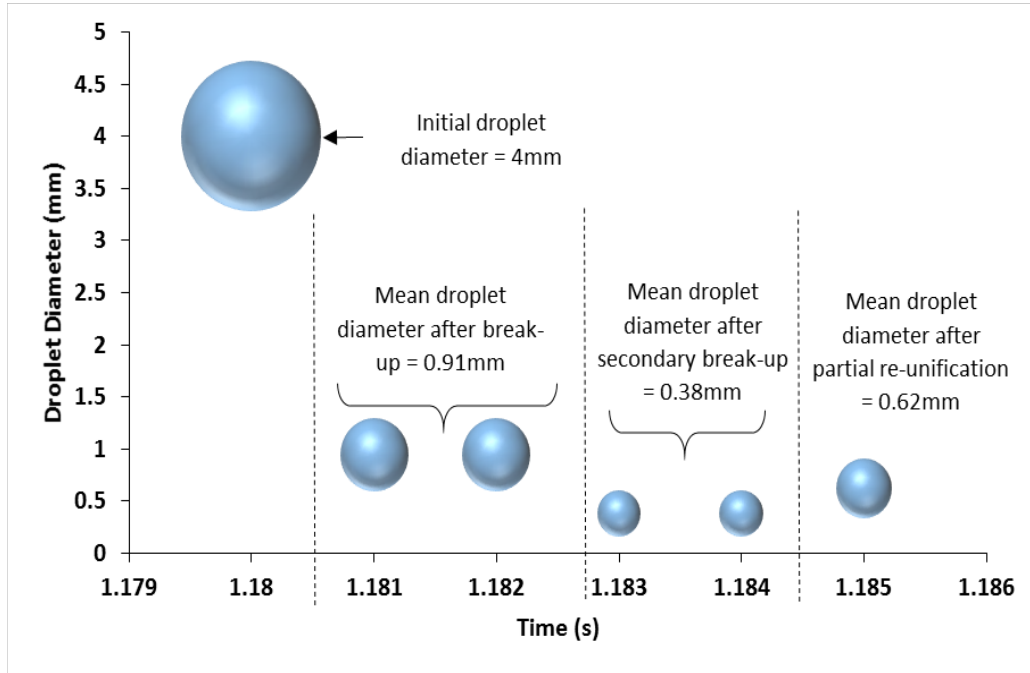


Figure 14: Droplet diameter variation

3.4 Discussion

This study investigated the effect of CPD and PCF variations in voluntary cough function using biomechanical modelling within the context of a trachea reconstructed from CT-scan images of human airways. The results of this study elucidate cough function and penetrant behaviour across three informative parameters, airflow velocity distribution, penetrant trajectory, and break-up pattern. The findings suggest that specific modifications to the expected cough dynamics may promote airway clearance.

3.4.1 Airflow Velocity

Specifically, the analysis of airflow velocity revealed that the modification in PCF resulted in substantial change in airway velocities for all cases modeled. This is consistent with previous studies and confirms the value of peak cough flow measures as a surrogate for velocity within an airway clearance event [11, 106]. The largest velocity magnitude is recorded in Case 2 (with

-40% CPD, +40% PCF) and Case 4 whereas the smallest is recorded in Case 1 (with -40% CPD, -40% PCF) and Case 3 (with +40% CPD, -40% PCF). The transient velocity variation in Case 1 and Case 2 is advanced in time compared to other cases due to short CPD. Therefore, the Case 2 demonstrates a strong fast cough response whereas Case 3 can be considered as a weak, slow cough. The outcome of velocity profiles shows that CPD primarily manipulates the pace of cough (fast / slow) while PCF contributes to the power of the cough (strong / weak).

3.4.2 Penetrant Trajectory

The trajectory study showed that Case 2 cleared more penetrants than any other cases. Recall that in Case 2, the CPD is decreased by 40% from the base case, and PCF is increased by 40%. The peculiarity of Case 2 appears due to the fact that the combined effects of these changes to CPD and PCF cause rapid flow acceleration after the short CPD duration, resulting in a favorable condition for the penetrant to break up before escaping from the mouth-end of the airway. In contrast, when the CPD was increased by 40% in Cases 3 and 4, the prolonged CPD resulted in the penetrant falling further down the airway before the expiratory phase. In addition, our data revealed that penetrants originating from the anterior side of the airway are likely to fall deeper into the airway presenting a greater challenge for airway clearance. A comparison of an anterior and a posterior penetrant at the same level in the airway showed the fact that the airway geometrical shape does not obstruct the path of the penetrants originating from anterior side. These data are novel and may provide direction to clinicians tracking events using dynamic video measurement. Consequently, the parameters defined by the simulated cases considered in this study may be utilized to direct therapeutic cough assist applications. The findings of the study also suggest that cough assist applications may need to effectively increase PCF and reduce CPD in order to maximize cough effectiveness as a defensive mechanism against aspiration.

3.4.3 Penetrant Break-up Pattern

Finally our study also comprehensively modeled penetrant break-up. During a break-up event, the penetrant diameter significantly drops when small child-droplets are created. In addition, the collision of liquid droplets together may enhance coalescence and increase the mean diameter of the droplets residing within the airway. By comparing the mean diameter, we may be able to predict the number of child droplets created in a specific break-up event. Previous studies measured aerosol droplet sizes leaving the mouth, but not within the airway [107]. Our findings shed light on a previously unrecognized issue within cough evaluation and management interventions. The role of droplet collision, coalescence and re-formation as a risk marker, and the impact of scattering for microaspiration events may need further consideration.

The data presented from our modeling efforts are both novel and informative to cough-assist evaluation and interventions. Modeling can assist in specifying different classes of features previously not recognized in contributing to event outcomes. Models like ours presented here can help us to better understand and possibly predict the behavior of cough function in conditions that cannot easily be experimentally reproduced. Despite this, the diversity of system conditions, the availability of system-specific information and availability of patient-specific data may limit outputs from any model and imply the need for validation and further adaptive models. One stiff assumption in our study is the use of static CT images to reconstruct the 3D airway geometry which thus has not considered the structural changes of the laryngeal wall. The use of optical flow-based motion estimation, which is derived from 4D CT image data set will enable to the representation of the dynamic nature of airway wall in subsequent studies. Like other modeling techniques, our efforts here must be further tailored not only to make the best use of the information available but also to answer additional questions such as; how does cough bolus/ material type interact with penetrant trajectory? How will anatomical

deviations (i.e. cervical spondylosis) impact the velocity and tracking of the penetrants? Likewise some of the parameters altered in our models were based on clinical knowledge of cough and patient cough experience. As a result, some bias and inaccuracy may be present in those decisions. Similarly, we have not considered the interactive events of cough and swallowing in airway clearance and penetrant trajectory. Although many questions remain, this study presents “proof of concept” in the development of a cough efficiency computational model.

This study also had some limitations which led to the improved model described in the next chapter. The biomechanical model did not consider the structural remodeling of the airway wall during the cough process. This remodeling may not be a major issue within the trachea on which this study is focused, but will be essential in the oropharyngeal and laryngeal regions containing softer tissues. The integration of fluid-structure interaction into the biomechanical model is therefore considered in the evolution of our work model presented in the next chapter. The model described in the next chapter would allow examination of the impact of airway remodeling on the flow-particulate behavior. The next limitation is that the reconstructed anatomy in this model does not span beyond the larynx which could result in inaccuracies in flow behavior. The flow outlet was set above the laryngeal vestibule and no downstream conditions were modeled. The realistic airway anatomy relevant to cough spans from the oral cavity to the trachea. This is taken as an enhanced modification to the biomechanical model in the next chapter in which the flow outlet would be set at the oral cavity and flow distribution within the pharynx, and oral cavity would also be simulated.

3.5 Summary

Airway modeling may be beneficial to the study of aspiration in patients with impaired cough function including those with upper airway and neurological diseases. It can be used to enhance the understanding of cough flow dynamics within the airway and to inform strategies for treatment with ‘cough assist devices’ or devices to improve cough strength. The proposed biomechanical model is the first of its kind to study cough-penetrant dynamics within the tracheal airway. As such it presents a “proof-of-concept” in the biomechanical modeling of human cough.

CHAPTER 4: MODELING COUGH AND AIRWAY CLEARANCE IN THE AIRWAY WITH WALL REMODELING

4.1 Overview

The objective of this chapter is to present the upgraded biomechanical model for calculation of the spatiotemporal flow-particulate behavior under a cough. The simulation includes improvement to the anatomy and physiology including oro-pharyngeal reconstruction beyond the laryngeal airway and deformable airway wall. There is a comprehensive description of the governing equations used to predict fluid flow, and particulate characteristics including particulate velocities and particulate location. Parametric study of particulate behavior is conducted to visualize solid penetrant transport in the airway during cough reflex which will be extended to droplets in a subsequent chapter. Six monitored locations are defined along the airway where velocity and pressure are monitored. The velocity and pressure are presented for using a cross-sectional plane that cuts across the airway vertically. In the next section of this chapter, we describe the materials and methods used in the study and formulation of the biomechanical model including the governing equations and their solution. The results of the simulations are then presented and discussed in subsequent sections.

4.2 Materials and Methods

4.2.1 Geometry Reconstruction and Mesh Generation

A representative geometry of the human airway was obtained from Computed Tomography (CT) scan images of a human subject in the standing posture, beginning at the oral cavity and extending to the trachea bifurcation at the entrance to the lungs. The scan resolution was 512x512 pixels with an inter-slice thickness of 3 mm. The CT-scan images (DICOM files) were first imported into the MIMICS image processing software [90]. Through color contrast

and complex surface rendering, images from the 2D cross sections (slices) were used to reconstruct the required 3D geometry as shown in Figure 15. The 3D geometry was then transferred in STL format to the StarCCM+ software for mesh generation and flow analysis [92].

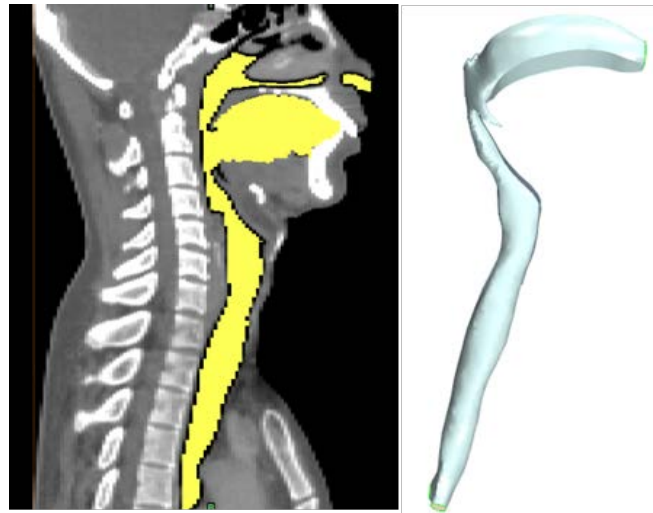


Figure 15: The reconstructed airway geometry in sagittal plane, and final geometry

The reconstructed geometry was discretized into meshes to be used for the finite volume numerical computation of airflow and penetrant tracking within the airway. Figure 16 shows the selected mesh used in the study. A combination of hexahedral cells in the core and prism layer cells near the wall were used to provide a high-quality robust and efficient mesh in order to capture both wall surface effects and geometrical features adequately. Specifically, the prism layers allow the model to resolve near-wall flow features such as flow separation, which in turn affects integral results such as drag or pressure drop. Accurate prediction of these flow features depends on the adequate resolution of the velocity gradient normal to the wall, which is steep in the viscous sublayer of a turbulent boundary layer. The base size of the mesh is selected as 0.2 mm with 8 prism layers of having 0.4 mm of the total thickness. By using multiple prism

layers near the wall of the mesh, low y^+ values close to 1 were obtained within the viscous sublayer during the simulation.

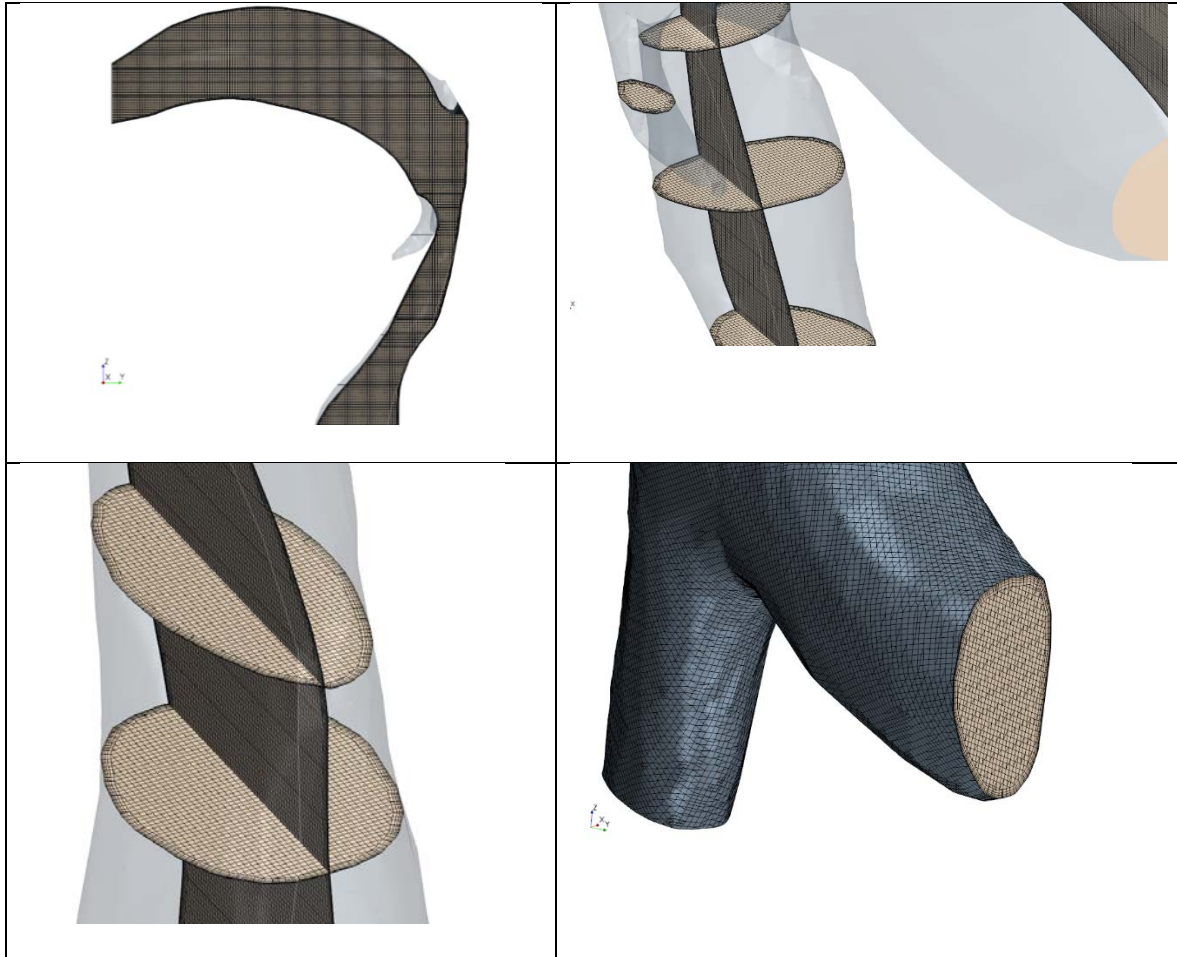


Figure 16: Mesh generated in the airway geometry

A mesh convergence study was performed with three different element sizes to establish a mesh-independent solution. The mesh for the results presented here had 5941425 elements with maximum skewness angle of 43° . Figure 17 shows the skewness histogram of the mesh used in this study.

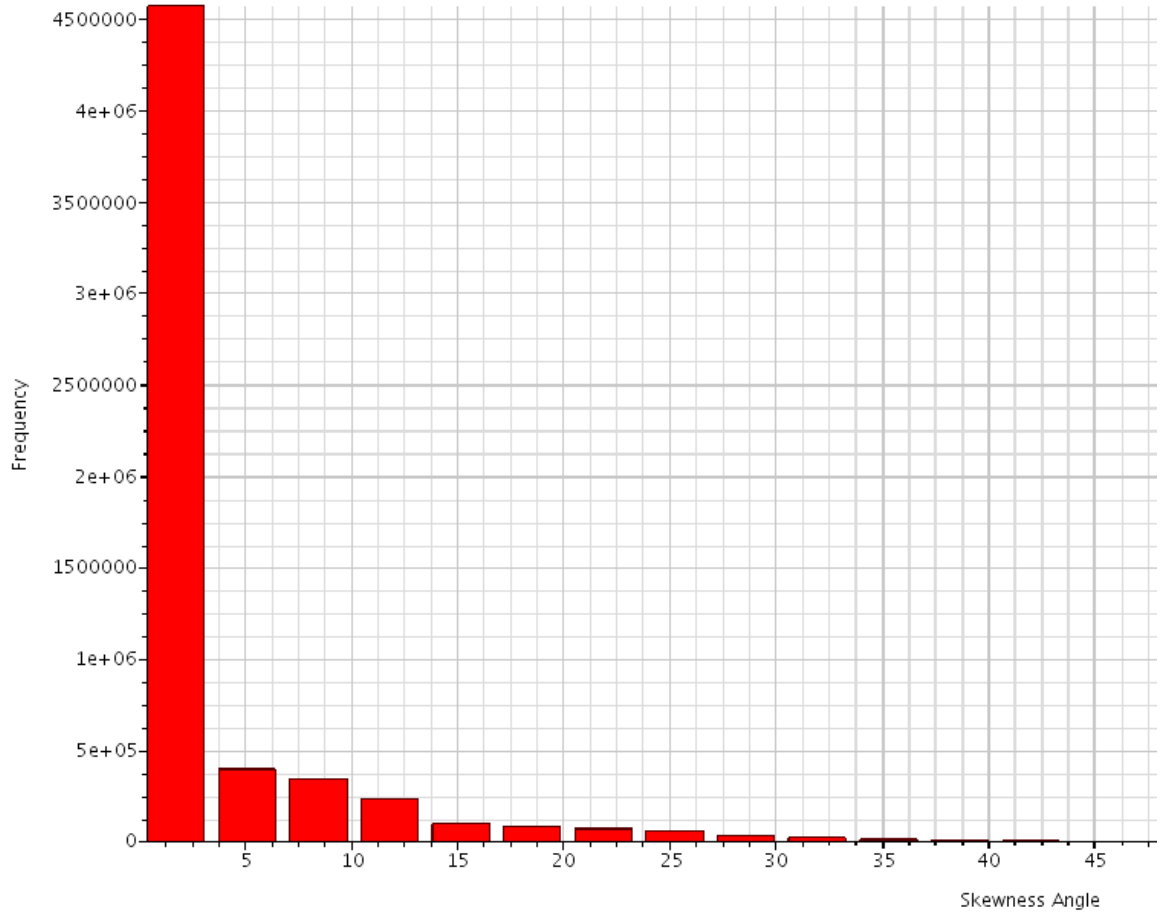


Figure 17: The mesh skewness histogram

4.2.2 Governing Equations for Fluid Flow

We assume that air is compressible and Newtonian with density ρ , and dynamic viscosity μ .

The equation of state for air is therefore expressed by ideal gas law in which the air density ρ is a function of temperature and pressure, thus:

$$\rho = \frac{P}{RT} \quad (4-1)$$

where P is pressure, R is the specific gas constant, and T is temperature. The flow in the airway during cough is typically considered transitional to turbulent [9, 26, 37]. The equations governing fluid flow are therefore taken to be the unsteady conservation of mass and

momentum for turbulent flow, with allowance for possible transition through turbulence modeling as described subsequently. The equations can be expressed in tensor notation thus:

Mass conservation:

$$\frac{\partial \rho}{\partial t} + \frac{\partial(\rho u_i)}{\partial x_j} = 0 \quad (4-2)$$

Momentum equation:

$$\frac{\partial(\rho u_i)}{\partial t} + \frac{\partial(\rho u_i u_j)}{\partial x_j} = -\frac{\partial(P\delta_{ij})}{\partial x_j} + \frac{\partial}{\partial x_j} \left[(\mu + \mu_t) \left(\frac{\partial u_i}{\partial x_j} + \frac{\partial u_j}{\partial x_i} \right) \right] + S_v \quad (4-3)$$

where, u_i , u_j represent time-averaged air flow velocities in x,y and z directions, μ is dynamic viscosity, and μ_t is turbulent (eddy) viscosity. The term S_v represents the momentum exchange between the dispersed phase (particulate) and carrier gas (air) and includes parts of the stress tensor not appearing directly in the diffusion and pressure gradient terms of the fluid flow equation.

The turbulent viscosity term in Equation (4-3) is evaluated for this transitional-to-turbulent flow system using the $k-\omega$ shear stress transport (SST) turbulence model [92] in which k is the turbulent kinetic energy, and ω is the specific dissipation rate. Specifically, μ_t will be evaluated from the general relation $\mu_t = k/\omega$. The $k-\omega$ SST turbulence model has been adopted in this study because Direct Numerical Solution (DNS) or Large Eddy Simulation (LES) turbulence models are computationally intensive [108]. In addition, the $k-\omega$ SST model has been successfully used for transitional flows [94] as may occur during cough, and represents an adequate compromise between computational intensity and accuracy.

The k - ω SST model is a two-equation eddy viscosity model requiring solution of the following two transport equations for k and ω :

k -equation:

$$\frac{\partial(\rho k)}{\partial t} + \frac{\partial(\rho u_j k)}{\partial x_j} = \tau_{ij} \frac{\partial u_i}{\partial x_j} - \beta^* \rho \omega k + \frac{\partial}{\partial x_j} [(\mu + \sigma_k \mu_t) \frac{\partial k}{\partial x_j}] \quad (4-4)$$

ω -equation:

$$\frac{\partial(\rho \omega)}{\partial t} + \frac{\partial(\rho u_j \omega)}{\partial x_j} = \frac{\gamma}{\nu_t} \tau_{ij} \frac{\partial u_i}{\partial x_j} - \beta \rho \omega^2 + \frac{\partial}{\partial x_j} [(\mu + \sigma_\omega \mu_t) \frac{\partial \omega}{\partial x_j}] + 2(1 - F_1) \frac{\rho \sigma_{\omega 2}}{\omega} \frac{\partial k}{\partial x_j} \frac{\partial \omega}{\partial x_j} \quad (4-5)$$

where τ_{ij} is turbulent shear stress. The value of parameter F_1 in Equation (4-5) is 1.0 near the surface and zero away from the surface [92]. The value of γ is obtained from the relation [30]:

$$\gamma = \frac{\beta}{\beta^*} - \frac{\sigma_\omega \kappa^2}{\sqrt{\beta^*}}. \quad (4-6)$$

The remaining parameters constitute the constants of the k - ω SST model. The values of model constants $\beta^*, \beta, \sigma_k, \kappa, \sigma_\omega$, and $\sigma_{\omega 2}$ have been established and validated in a previous study to be 0.09, 0.0750, 0.85, 0.41, 0.5, and 0.856 respectively [94].

4.2.3 Penetrant Dynamics

The motion of the penetrant within the airflow is determined by the momentum exchange between the carrier gas and the penetrant. In general, the particle velocity is different from that of the surrounding fluid. The relative velocity between the penetrant and the fluid is used to calculate the temporal penetrant location \mathbf{r}_p , thus:

$$\frac{dr_p}{dt} = u_p - u \quad (4-7)$$

where u_p is the particle velocity, and u is flow velocity.

We assume that the momentum balance for the penetrant is governed by Newton's second law of motion expressed by the following force-balance equation[92]:

$$m_p \frac{du_p}{dt} = F_D + F_L + F_{PG} + F_{AM} + F_B \quad (4-8)$$

where m_p is mass of the penetrant, F_D is Stokes drag force acting on the surface of the penetrant, F_L is lift force acting on the penetrant, F_{PG} is pressure gradient force developed by undisturbed flow, F_{AM} is added-mass force created by displaced fluid, and F_B is Buoyancy force. The left hand side of the equation represents the inertial force acting on the penetrant due to its acceleration.

The drag force per unit particle mass is given by [109]:

$$F_D = \frac{1}{8} \pi d_p^2 \rho_p C_{DP} (u - u_p) |u - u_p| \quad (4-9)$$

where ρ_p is penetrant density, d_p is penetrant diameter, and C_D is drag correlation. In this study, the penetrant is assumed to be a spherical particle with small diameter. Thus the Shiller-Neumann drag correlation is used to define the particle drag coefficients thus:

$$C_D = \begin{cases} \frac{24}{Re_p} (1 + 0.15 Re_p^{0.687}) & Re_p \leq 1000 \\ 0.44 & Re_p > 1000 \end{cases} \quad (4-10)$$

Here $Re_p = \frac{\rho_p u_p d_p}{\mu}$ is the particle Reynolds number. The lift force acting on particle is given by:

$$F_L = \frac{\rho \pi}{8} d_p^2 C_{LR} |u - u_p| \frac{\Omega \times (u - u_p)}{|\Omega|} + C_{LS} \frac{\rho \pi}{8} d_p^3 [\Omega \times (u - u_p)] \quad (4-11)$$

Here C_{LR} and C_{LS} are rotational and shear left coefficients respectively which are evaluated using Sommerfeld definition [110].

The rest of the terms in the Equation (4-8) can be expressed as follows:

$$F_{PG} = m_f \frac{du}{dt} \quad (4-12)$$

$$F_{AM} = \frac{1}{2} m_f \left(\frac{du}{dt} - \frac{du_p}{dt} \right) \quad (4-13)$$

$$F_B = (m_p - m_f)g \quad (4-14)$$

in which m_f is the mass of the fluid displaced by the penetrant and g is gravity.

Turbulence within the cough airflow causes the penetrant to collide with the walls of the airway. These collisions produce wall-particle forces that affect the momentum of the penetrant and are modeled according to the rebound-interaction model [39]. The airway wall is covered with a surface liquid layer which introduces possible mucus-induced high possibility of stickiness to the airway wall [111]. The presence of mucus is represented in the biomechanical model through a wall restitution coefficient. Specifically, the rebound velocity relative to the wall is determined by the impingement velocity and a restitution coefficient thus:

$$u_{p,rebound} = e_t u_{p,impinged} \quad (4-15)$$

$$u_{p,rebound} = e_n u_{p,impinged} \quad (4-16)$$

where e_t and e_n denote the restitution coefficients in the wall-normal and tangential directions respectively. In the present study, these restitution coefficients were set to 0.1 to allow for a small amount of stickiness at the surface of the airway. This exclusive assumption was

subjected to a sensitivity analysis in order to illustrate the effect of the chosen value of restitution coefficient, which was presented in the discussion section.

4.2.4 Design of Penetrant Study

A horizontal plane in the laryngopharynx was examined of which six different landmarks were selected to represent the launching positions for penetrants entering the larynx from the oropharynx. Due to the high sensitivity in penetrant launching positions, six particles are distributed parametrically to represent possible penetrant entering the domain in the anterior-posterior and lateral directions. All six penetrants are released under similar conditions and used for the aspiration risk assessment. Figure 18 shows the landmarks selected for examination within the airways.

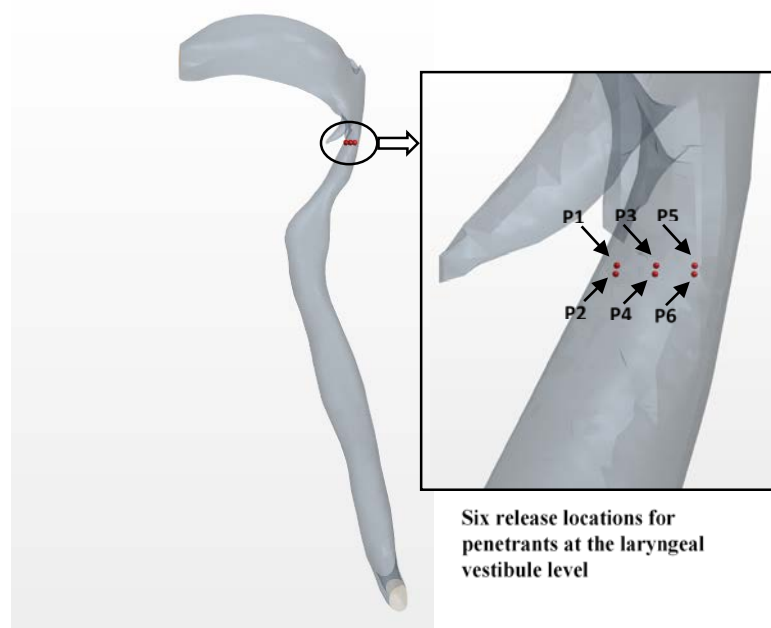


Figure 18: Locations of the penetrant ejection at the laryngeal vestibule level

Six solid particles assuming spherical shape were injected at as the penetrants, and the position, time, and velocity with which the penetrant crossed the control volume boundaries were monitored. A parametric study to investigate the effects of mass and size on penetrant trajectory was implemented by varying the initial diameter of the penetrant into two more values. The penetrants were injected and tracked through the airway segment until they either: (1) remained inside the airway or escaped through one of the bottom faces (penetrant aspiration), or (2) pushed into the oral cavity or escaped from the mouth-end of the airway (penetrant expulsion). A two-way coupling of momentum was assumed between the fluid and the penetrants as the six solid particles were in motion in the fluid during the simulation[112].

4.2.5 Initial and Boundary Conditions

The boundary conditions used in this study were the rate of mass flux (inlet) at the end of the two branches and zero gauge pressure (outlet) at the top end of the airway. The rate of mass flux was obtained from the cough profiles assuming that amount recorded in the cough profile was essentially passed through the airway. The mass flux at the inlet was therefore allowed to change with time accordingly while the rest of the boundary conditions remained unchanged.

Two different cough profiles obtained from human subjects were chosen in order to simulate two distinct cough events: a weak and strong cough. A weak cough in this study represents a cough commonly observed in patients with laryngeal disorders [113]. In general, reduced peak cough flow rate (PCF) and prolonged compression phase duration (CPD) marks weak cough events. In contrast, strong cough events have high PCF and short CPD to generate rapid, forceful ballistic airflow within the airway[113]. A typical voluntary cough has three phases: inspiratory; compression; and expiratory phase. However, inspiratory phase is not observed in most cases when a laryngeal penetrant is present[99]. Therefore, for the purpose of this study,

the simulation was started from the compression phase of cough. Figure 19 shows the two cough profiles used in this study.

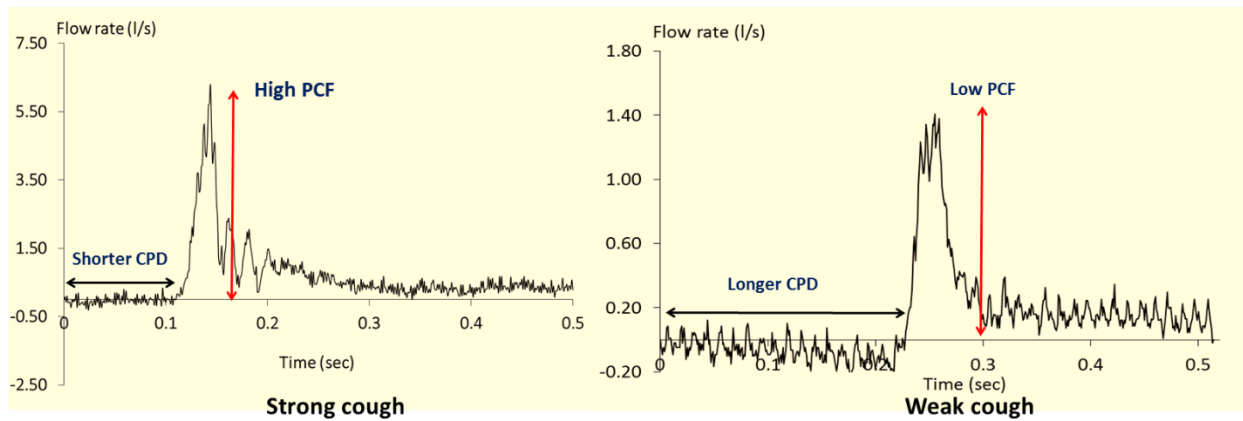


Figure 19: Cough profiles used in this study

Figure 20 shows the defined boundaries including details of the different regions of the airway.

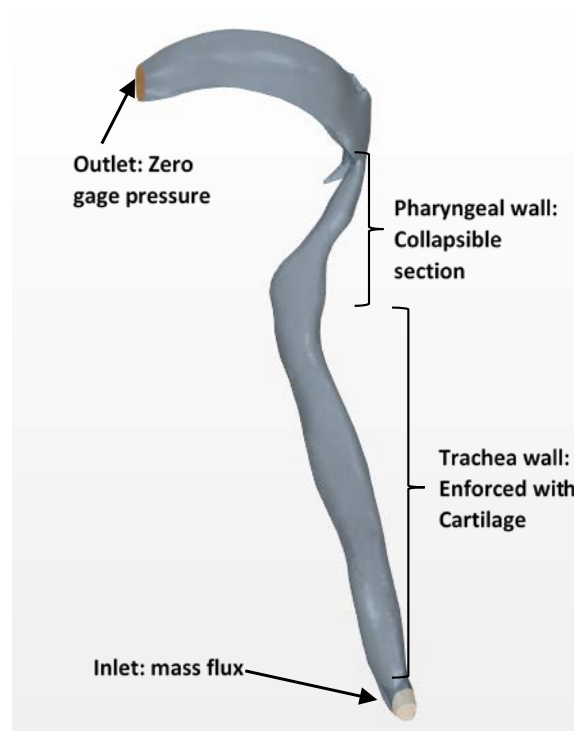


Figure 20: Airway geometry with inlet and outlet boundary surfaces

4.2.6 Airway Wall Remodeling

The cough mechanism is designed naturally to increase the flow downstream to a maximum in order to produce an effective airway clearance. This is achieved by generating high expiratory flow rates and dynamically collapsing the airway to reduce the cross-section area [19, 113, 114]. Therefore, in this model, we have assumed the wall of the upper airway to be flexible. Specifically, the airway wall is considered to be a collapsible tube during the forceful expiratory phase. The effect of this collapsible tube mechanics is integrated into the model by allowing the anterior and posterior walls of the airway to remodel transiently depending on the expiratory flow-time distribution.

In modeling perspective, this phenomenon changes the finite volume mesh of the initial airway, and thus requires redistribution of mesh vertices in response to the movement. The dynamic mesh morphing technique is used to generate the displacements [115]. As the air flow accelerates from a minimum at the end of the compression phase to the peak cough flow rate at the expiratory phase, the wall of the laryngeal airway is assumed to come closer such that the cross-section area is reduced as a function of flow distribution of the expiratory phase. After the peak expiratory flow, the airway is allowed to relax back to its original size. Figure 21 shows how the airway cross-section changes at the laryngeal level during the expiratory phase of the strong cough profile to illustrate the effect of airway wall dynamics on flow parameters. The real-time duration after cough initiation is shown in each instance. In the beginning, the airway is in its original shape with large internal volume. After the expiratory phase is reached, the airway wall in the laryngopharynx and trachea starts to deform mainly from the posterior wall. The deformation then reaches a maximum at the peak expiratory flow which is 0.15s for the strong cough considered in this study.

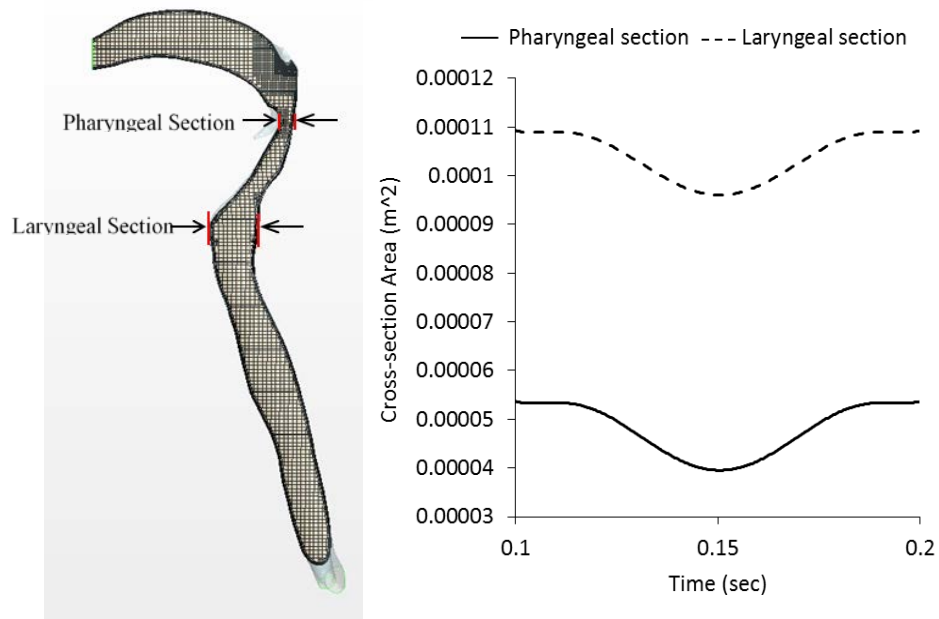


Figure 21: Airway wall deformation

4.2.7 Monitored Locations

The central sectional plane in the vertical direction across the geometry was selected for analysis of intra-airway flow velocities which are displayed in Figure 22(a). Six locations within the airway were selected and monitored in order to assess the transient velocity and pressure magnitudes. These six locations are illustrated in Figure 22(b).

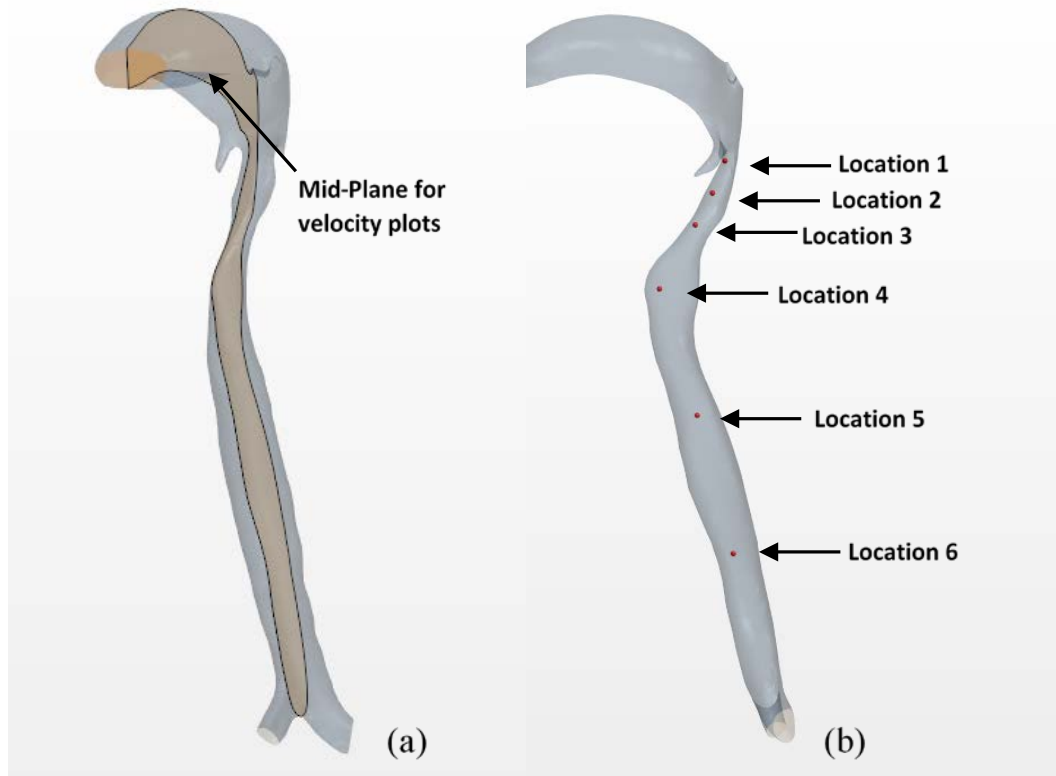


Figure 22: Vertical plane (a), seven monitored locations in the airway (b)

4.2.8 Assessment of Aspiration Risk

In order to assess aspiration risk, the predicted trajectories of the penetrants are analyzed and assigned numerical values between 1 and 8 based on the PAS scale. The penetration depth of the particles determines the decision-making criteria used to obtain the PAS scale in the airway and whether or not the particles are expelled from the airway. Figure 23(a) shows the regions of the airway with the possible particle behaviors. The term “penetration” is applied up to and above the vocal fold while “aspiration” is applied below the level of the vocal folds. Figure 23(b) shows the numerical values based on the outcome of the cough event. The ideal case with no penetration is assigned a value 1 while 8 is assigned to the poorest case of no cough

effectiveness. Numbers 2, 4, and 6 represent cases where penetrants are ejected, and numbers 3, 5, and 7 represent cases where penetrant remain within the airway.

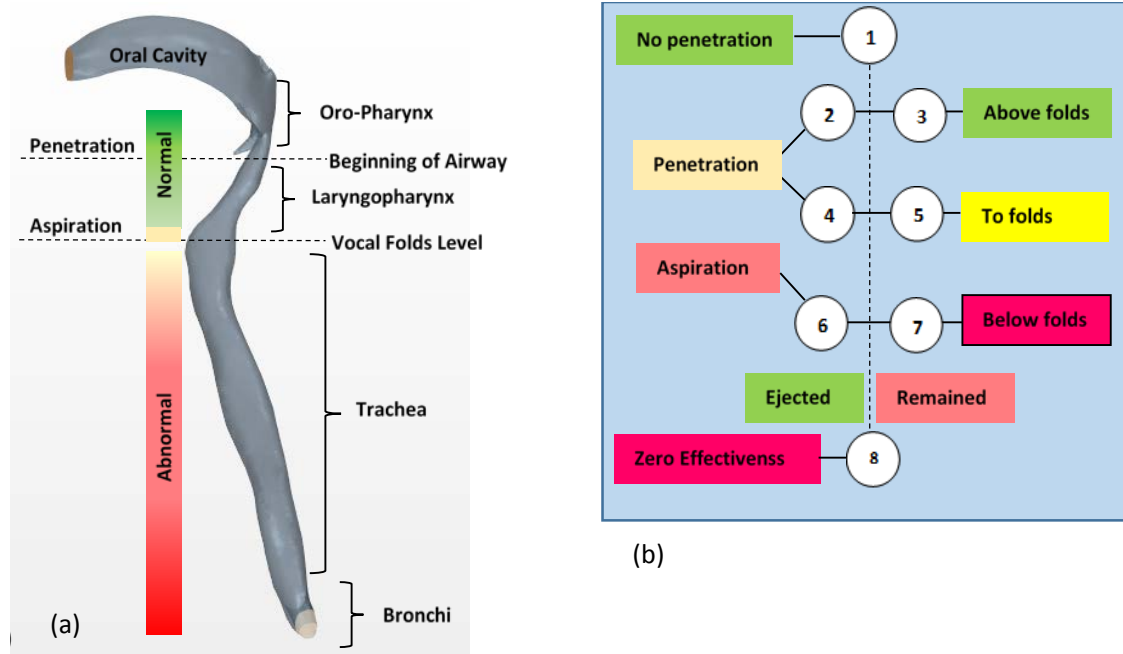


Figure 23: Decision-making criteria used in PAS score defined by (a) airway depth; and (b) schematic of numerical values

4.2.9 Computational Details

A finite volume based CFD software StarCCM+ was used for the simulation, utilizing an implicit unsteady solver with a minimum time step of 10^{-5} secs and second-order temporal discretization with second-order upwinding scheme. The time step was determined based on the Courant number which is expressed as:

$$Courant\ number = \frac{u \Delta t}{\Delta x} \quad (4-17)$$

where Δt is the time step and Δx is the mesh size. The Courant number is kept approximately 1 in order to have numerically stable and accurate solution. The computation was performed

on a workstation using Intel Core i7 processor with 32GB RAM. The average computational runtime for airflow was 20 to 40 hours depending on additional solving time for the droplet secondary break-up. A grid-independence test was first performed for three different grid sizes (~3000000, 4500000, and 6000000 cells) based on the velocity changes in their values at the monitored locations described in the next section. The computed results were found to be essentially independent of the grid size beyond 4500000 cells.

4.3 Results and Discussion

4.3.1 Velocity Distribution

Figure 24 shows the color-coded magnitude of velocity on the mid-plane as illustrated in previous Figure 22(a) at seven instances for the strong cough profiles considered in this study. It should be noted that red color indicates the largest velocity (100 m/s) and blue, the smallest.

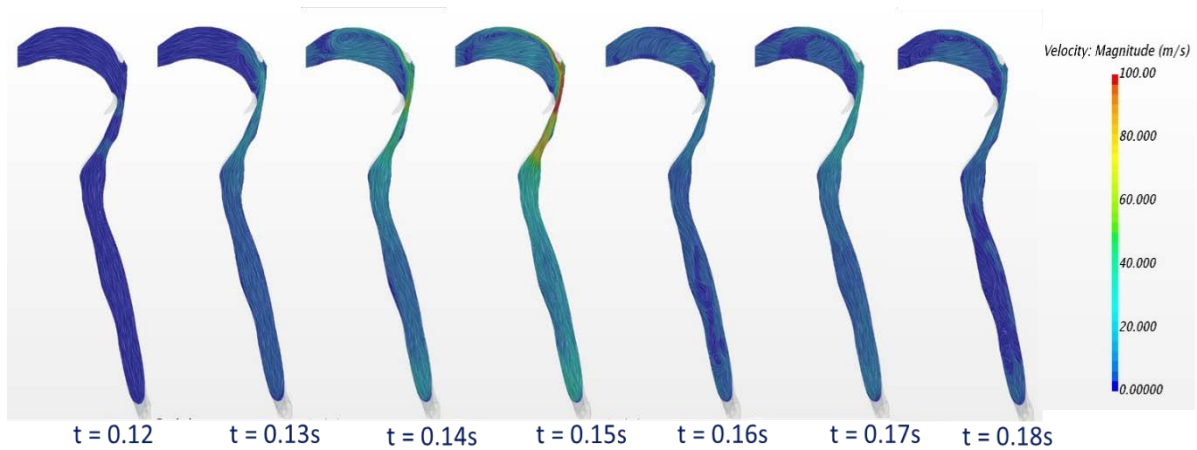


Figure 24: Predicted velocity magnitude for strong cough event

Figure 25 shows the color-coded magnitude of velocity on the mid-plane as illustrated in previous Figure 22(a) at seven instances for the weak cough profiles considered in this study.

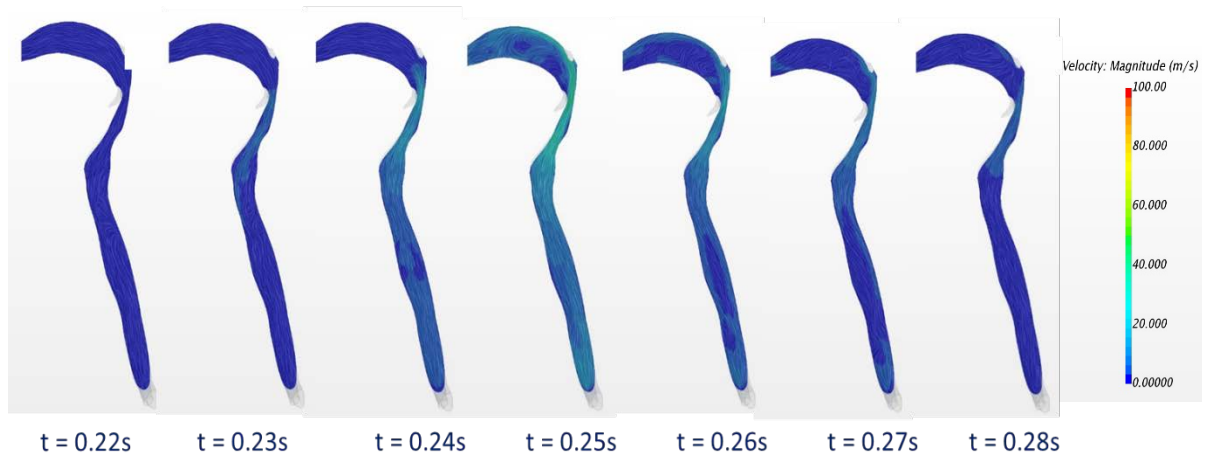


Figure 25: Predicted velocity magnitude for weak cough event

Figure 26 shows the transient variation of velocity for strong cough at the six monitored locations previously identified in Figure 22(b).

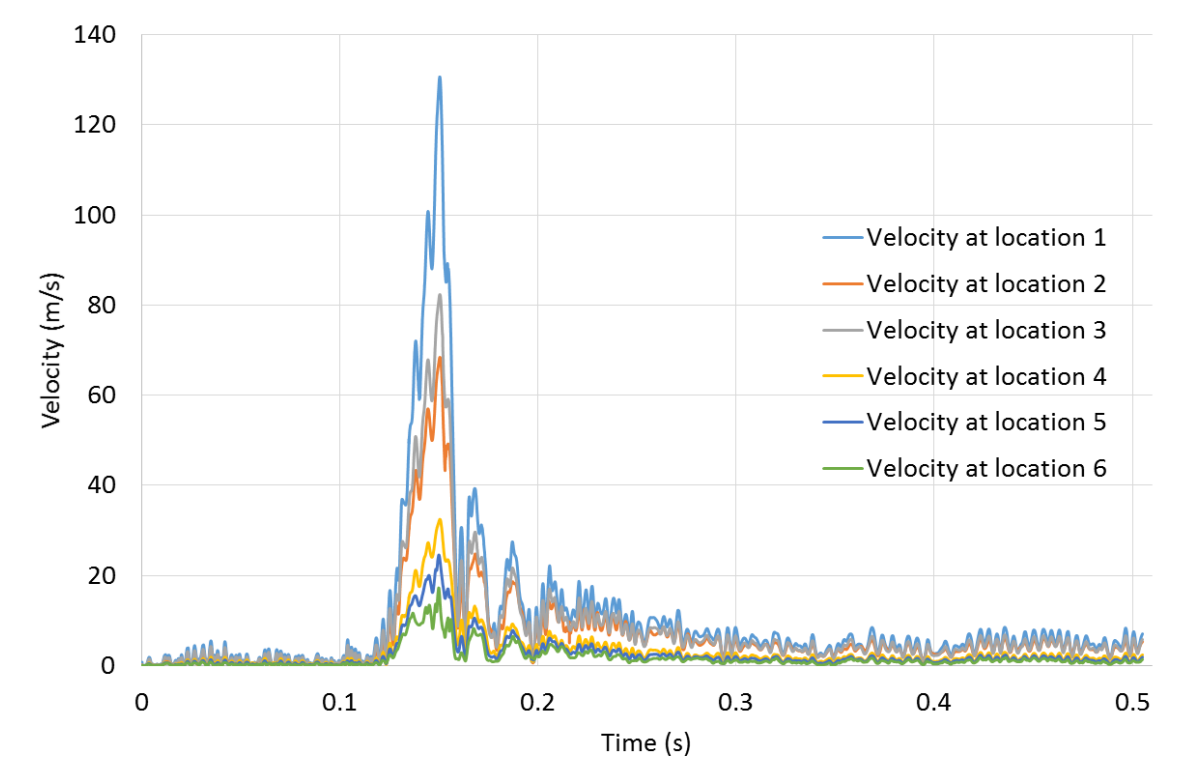


Figure 26: Predicted velocity magnitude with time at 6 monitored locations

In all cases, the highest flow rates are observed during the peak expiratory flow phase. The velocities at all the six locations follow the same general pattern with the largest values at location 1 where the airway is narrowest. The predicted velocity at location 1 is 130 m/s at (just after peak-expiratory flow). This value is close to 150% of the value predicted at any other location. The kinetic energy of moving gas relates to the square of velocity. Thus, the force exerting on the particles is significantly greater in Location 1 than that available in other regions.

The results (not shown) also indicate that the flows exhibit sudden acceleration during the expiratory phase, as high as 3971 m/s^2 at the narrowest section of the airway. The temporal variation of the velocity at other locations is not as high as at location 1. Location 6 at the straight part of the airway remote from all geometrical distortions exhibits the least velocity fluctuation, reaching a maximum of 16m/s. Figure 27 shows the transient variation of velocity for weak cough at the six monitored locations previously identified in Figure 22(b).

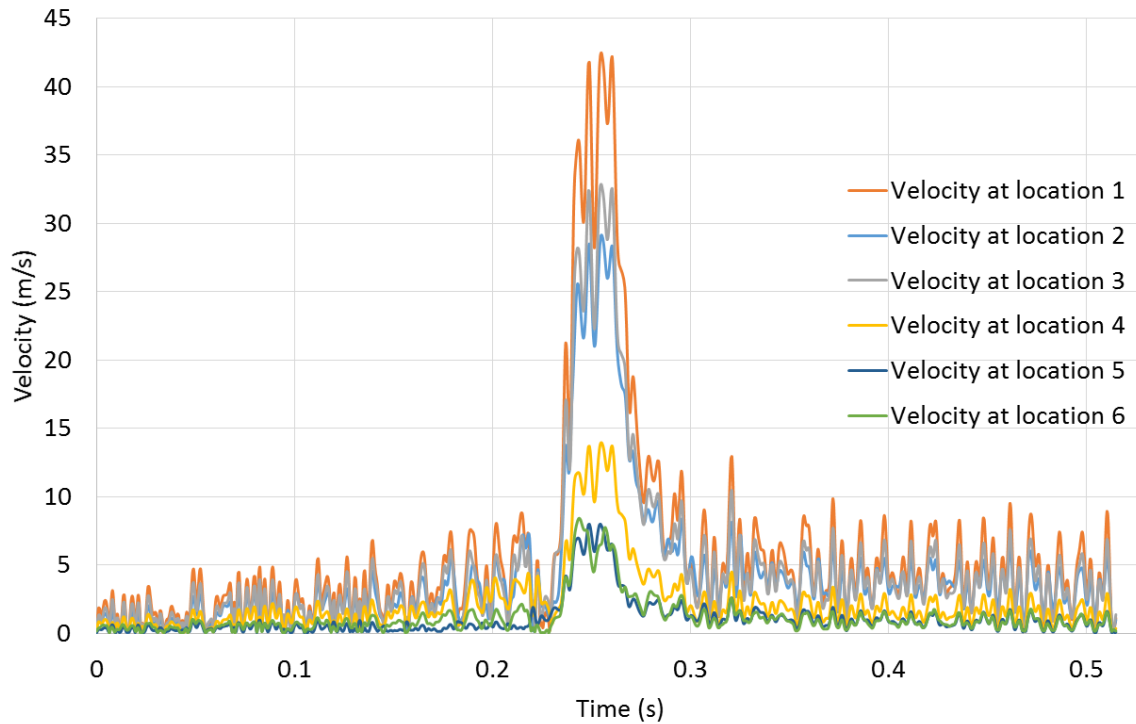


Figure 27: Predicted velocity magnitude with time at 6 monitored locations

4.3.2 Penetrant Trajectory

The purpose of the study was to assess penetrant behavior within the human airway during cough. Cough was induced as a result of penetrant released into the oropharynx and entering the larynx. The variables of interest included penetrant density and size, as summarized in Table 2.

Table 2: Input parameters used for the penetrant study

Penetrant size (Diameter in mm) d_p	1 mm, 1.5 mm, 2mm
Penetrant shape	Spherical
Penetrant density	500 kg/m ³ , 1000 kg/m ³ , 1500 kg/m ³

Typical behavior of the predicted trajectory of each penetrant released under strong and weak cough are shown in Figure 28 and 29 respectively. Penetrants were introduced at the same time to avoid differences in resident time.

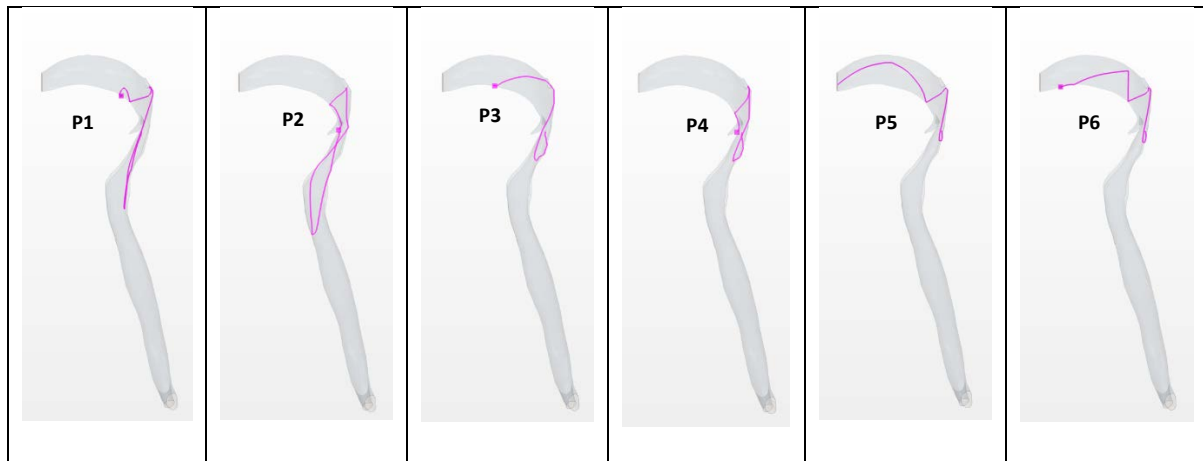


Figure 28: Predicted penetrant trajectory of six penetrants under strong cough (Penetrant diameter = 1mm, density = 500 kg/m³)

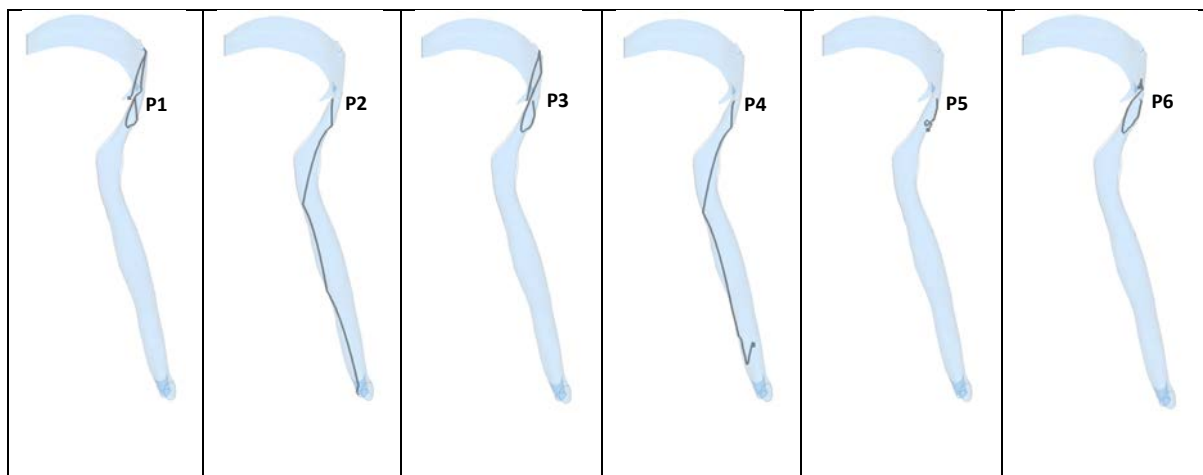


Figure 29: Predicted penetrant trajectory of six penetrants under weak cough (Penetrant diameter = 1mm, density = 500 kg/m³)

The first parametric study examined the predicted trajectory of different sizes of penetrants during cough. Three particle diameters were chosen based on the typical size of food penetrants

after mastication (Table 2)[116, 117]. Again, all the particles were assumed to be released at the beginning of the compression phase (after cough initiation). The purpose of the study was to assess the effect of the penetrant size on potential for expulsion under a particular cough. In order to quantify the effect of diameter on each penetrant trajectory, three additional parameters: (i) drag force exerted on the penetrants, (ii) penetrant velocity, and (iii) penetrant Reynolds number of each penetrant inside the tracheal airway, were monitored. Figure 30 shows how each of these parameters changed for penetrant released at the P5 location under strong cough.

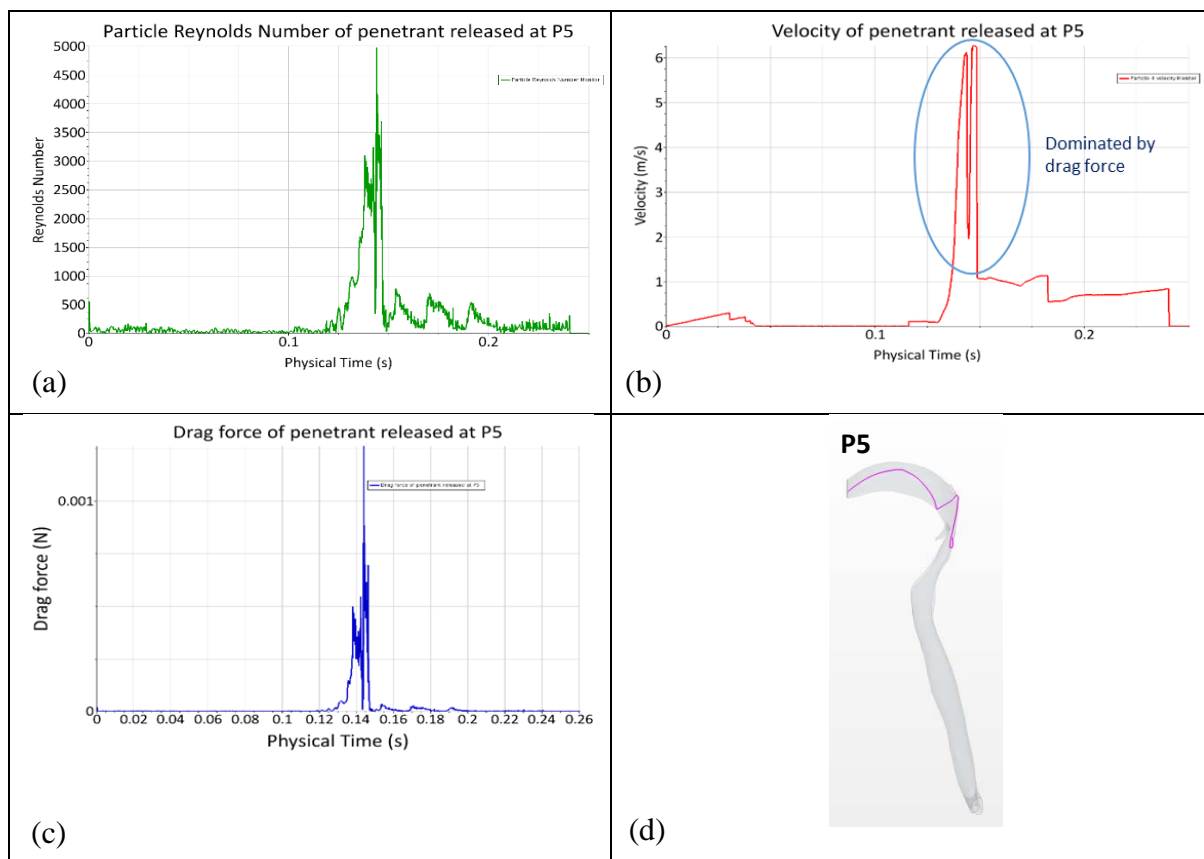


Figure 30: Monitored Parameters for Penetrant P5

The drag force exerted on the penetrant P5 is notably fluctuating between 0.12 and 0.15 sec. There is relatively no drag force exerted between 0.0 sec and 0.12 sec during the compression

phase of cough. After 0.12 sec, the penetrant is subjected to drag forces caused by the expiratory flow. A maximum drag force of 0.010056 N is predicted during the expiratory phase. The penetrant velocity profile is nearly analogous to the drag force pattern presented in Figure 30(b). The sudden drops and fluctuations in penetrant velocity are due to momentum loss from penetrant collisions with the walls of the airway. The predicted highest penetrant velocity is 6.3 m/s, when maximum drag force is being exerted on the penetrant. Thus, the drag force is determined to be the primary contributor to changes in penetrant momentum. The drag force could either make the penetrant move with the flow or collide with the walls of the airway. During the compression phase, the penetrant velocity exhibits a magnitude although the drag force is nearly zero. A possible explanation for this trend is that gravity acts to increase the penetrant velocity even in the absence of airflow. Tables 3 and 4 show the maximum drag force for each penetrant under strong and weak cough respectively while the diameter is changed parametrically.

Table 3: Parametric study of penetrant size (diameter variation) under strong cough event

	Maximum drag force ($\times 10^{-4}$ N)		
Penetrant	1mm	1.5mm	2mm
P1	0.501	3.87	4.10
P2	0.66	3.00	4.31
P3	23.21	28.39	61.24
P4	0.838	37.5	57.13
P5	14.80	54.9	100.56
P6	46.8	16.78	81.15

Table 4: Parametric study of penetrant size (diameter variation) under weak cough event

Penetrant	Maximum drag force ($\times 10^{-4}$ N)		
	1mm	1.5mm	2mm
P1	0.386	0.071	6.5
P2	0.147	0.256	7.7
P3	0.11	0.209	0.263
P4	0.162	0.235	0.389
P5	1.435	0.675	0.261
P6	0.146	0.274	0.418

The next parametric study considered the effect of the penetrant density on the trajectory and the outcome of the cough event. Three values of the penetrant density were selected to match the effective density of food particles typically swallowed and entering the esophagus. Penetrant trajectory studies were conducted by assigning the two additional density values to the penetrants under strong and weak cough events. Similar to the second parametric study, the results of this study were analyzed using the same three individual variables. The maximum drag force values are presented in Table 5 and 6 for strong cough and weak cough respectively while the density is changed parametrically.

Table 5: Drag force on penetrant under strong cough event

	Maximum drag force ($\times 10^{-4}$ N)		
Penetrant	500 (kg/m ³)	1000 (kg/m ³)	1500 (kg/m ³)
P1	1.32	0.501	0.965
P2	4.216	0.66	0.797
P3	40.18	23.21	87.96
P4	1.708	0.838	1.853
P5	10.15	14.80	9.97
P6	82.17	46.8	25.42

Table 6: Drag force on penetrant under weak cough event

	Maximum drag force ($\times 10^{-4}$ N)		
Penetrant	500 (kg/m ³)	1000 (kg/m ³)	1500 (kg/m ³)
P1	48.55	0.386	0.1538
P2	0.054	0.147	23.94
P3	1.607	0.11	0.108
P4	0.141	0.162	0.139
P5	0.123	1.435	0.323
P6	1.063	0.146	0.343

4.3.3 Penetrant Behaviour Outcome

Tables 7 – 10 summarize the penetrant trajectory outcome evaluated for two parametric studies under both strong and weak cough. It was found that all penetrants of having 2mm and 1.5 mm diameter escaped the airway under strong cough. Penetrant size significantly influenced the drag force. This finding was not surprising given that larger particles travel faster than small diameter particles due to increase of surface area. By comparing the drag force and the velocity

plots, we concluded that drag force was the main contributor to changes in the momentum of the penetrant.

Table 7: Penetrant trajectory outcome for penetrant diameter variation under strong cough event

Penetrant Size (diameter in mm)	No. of penetrants retained	No. of penetrants aspirated	No. of penetrants escaped
1	0	1	5
1.5	0	0	6
2	0	0	6

Table 8: Penetrant trajectory outcome for penetrant diameter variation under weak cough event

Penetrant Size (diameter in mm)	No. of penetrants retained	No. of penetrants aspirated	No. of penetrants escaped
1	5	1	0
1.5	4	2	0
2	4	2	0

Table 9: Penetrant trajectory outcome for penetrant density variation under strong cough event

Penetrant Density (kg/m ³)	No. of penetrants retained	No. of penetrants aspirated	No. of penetrants escaped
500	0	0	6
1000	0	1	5
1500	0	1	5

Table 10: Penetrant trajectory outcome for penetrant density variation under weak cough event

Penetrant Density (kg/m ³)	No. of penetrants retained	No. of penetrants aspirated	No. of penetrants escaped
500	5	1	0
1000	5	1	0
1500	3	3	0

4.3.4 Assessment of Modeling improvements

Figure 31 shows the velocity distribution at 0.15s into the simulation of strong cough event for two airway models. We applied a strong cough profile to differentiate the effect of airway geometry on velocity distribution with or without oropharyngeal anatomy attached to the laryngeal airway. In the model described in the previous chapter (Chapter 3), the flow outlet was set above the laryngeal vestibule, and no downstream conditions were considered. In the process, the flow outlet was set at the oral cavity and flow distribution within the pharynx and oral cavity was simulated.

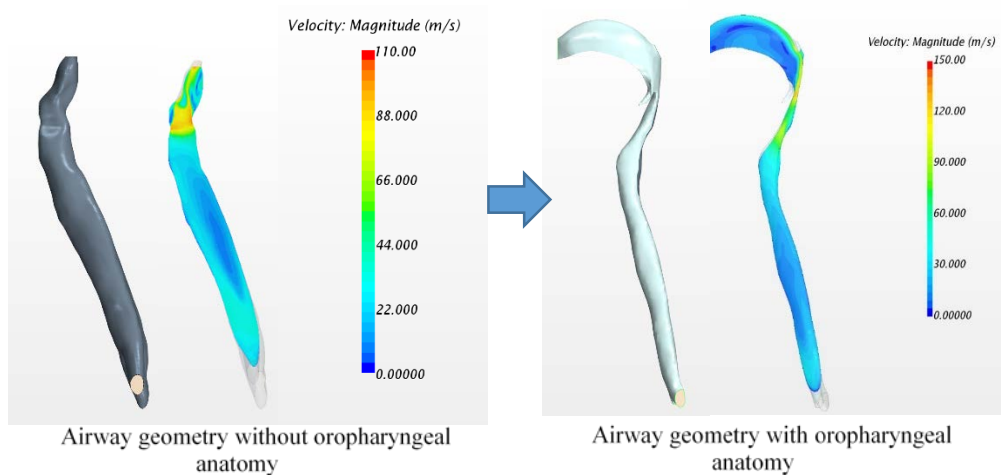


Figure 31: Comparison of velocity distribution in two airway geometries

Figure 32 shows how the airway wall dynamics modifies the velocity distribution. Three landmarks: (laryngopharynx of the airway, entrance of trachea, and the lower trachea), were monitored for velocity magnitude with and without allowance for airway collapse under the same cough profile. By integrating the airway wall deformation into the model, we observed a significant increase in the magnitude of the velocity within the laryngopharynx region. The percentage increase near the epiglottis was 52% which certainly influences the drag force acting on the penetrants. There was no increase observed for velocity magnitude within the lower end of the trachea (Location 3) because wall remodeling had a minimal effect within the lower end of the trachea.

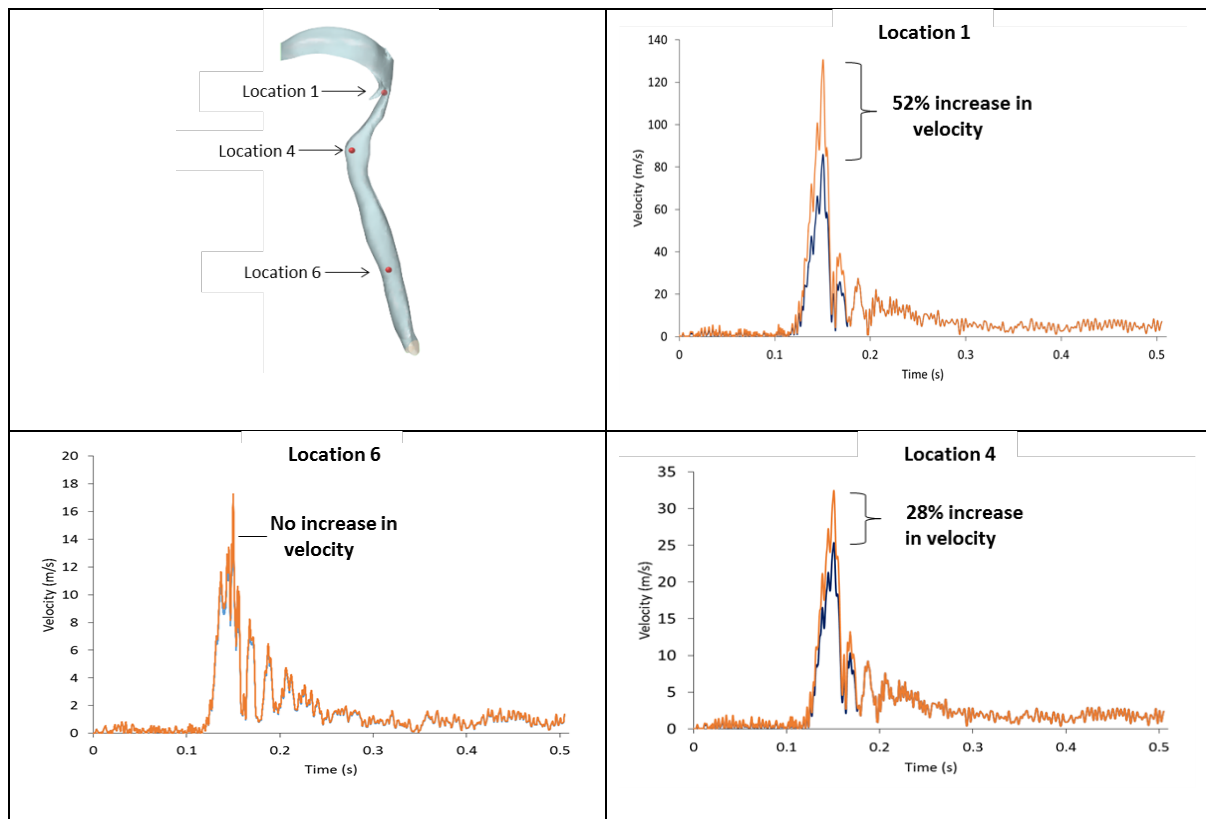


Figure 32: Variation of velocity magnitude at three locations within the airway for rigid and deforming walls

4.4 Summary

The airflow behavior and penetrant transport under cough were investigated within the context of a 3D airway geometry reconstructed from CT-scan images of the human airways and imported into CFD simulation software. The flow governing equations and the particle transport equations were solved with the finite volume method in order to calculate the transient cough flow distribution, and penetrant dynamics. Cough waveforms are comprised of several distinct stages: inspiratory phase, compression phase, and expiratory phase. The expiratory phase is the strongest phase of cough and results in very high observed airway velocities and pressures. At peak-expiratory flow instance, the velocity was predicted to be 130 m/s for the specific cases and conditions considered. The narrowest part of the airway had the highest velocities throughout the cough event.

CHAPTER 5: MODELING DROPLETS BREAKUP UNDER COUGH IN HUMAN AIRWAY²

5.1 Overview

The objective of the chapter is to extend the cough model developed in Chapter 4 to simulate and characterize the behavior of a typical liquid penetrant droplet during a cough event. We hypothesized that the fate of liquid droplets within the laryngeal airway under cough depends on droplet breakup pattern and sizes of subsequent child droplets generated. Two factors (number of droplet breakups and diameter of child droplets) were evaluated using an improved biomechanical model of the airway under two specific cough conditions. The model allows for turbulent airflow-droplet interaction and droplet collision on the surface, and droplet breakup. Liquid droplets with the density of water were released at same locations inside the airway defined in chapter 4 and tracked in the course of simulated cough. Two cases, a strong cough, and a weak cough, representing a patient with disorders of laryngeal function were used in comparison to characterize droplet behavior. The results of the simulations are then presented and discussed in subsequent sections.

5.2 Materials and Methods

5.2.1 Formulation of Droplets Behavior in Cough Flow

The droplets frequently disintegrate under the action of aerodynamic forces, a phenomenon that is known as a secondary break-up. The response of droplets to non-uniform surface forces is invariable to deform, with the deformation resisted by surface tension and viscous forces

² The materials of this Chapter have been submitted to *Laryngoscope Journal* and been in review process. Kuruppumullage, D. N., Hoffman Ruddy, B. & Ilegbusi, O. J. (2017). Computational Modeling of Cough and Airway Clearance in Patients with Disorders of Laryngeal Function.

inside the droplet. Characteristic measures of this behavior are the Weber (We) and Ohnesorge numbers (Oh) [118, 119].

$$We = \frac{\rho v^2 D_P}{\sigma} \quad (5-1)$$

where ρ is air density, v is cough flow velocity, D_P is droplet diameter, σ is the surface tension.

$$Oh = \frac{\mu_p}{\sqrt{\rho_P \sigma D_P}} \quad (5-2)$$

where μ_p is the liquid viscosity of the droplet. We allowed for droplet breakup under the action of aerodynamic forces by employing the Reitz-Diwakar breakup model [120, 121]. The model is based on the length scale and the time scale of a droplet breakup. The Reitz-Diwakar model assumes two possible breakup modes: (i) ‘bag’ breakup, in which the pressure field becomes non-uniform around the droplet causing it to disintegrate as the surface tension forces are overcome; (ii) ‘stripping’ breakup in which liquid is stripped from the parent droplet surface[92].

5.2.2 Design of Droplet Study

The objective of this study is to assess the effect of droplet break-up phenomena on cough effectiveness. The cough effectiveness in the presence of laryngeal liquid penetrants is defined by the ability to expel a droplet without retaining any of subsequent child droplets within the airway under a cough. The fate of liquid droplets in the event of a cough depends on the droplet size, location, break-up pattern, and cough strength in order to travel along the airway, and loose mass and finally disintegrate into small droplets. Hence, the droplet study is designed to record the break-up pattern, creation of child droplets, and size of child droplets under two cough profiles. A location in the laryngopharynx is chosen to define as the launching locations

for the droplet in this study. The droplet is released at the beginning of the CPD to allow free-fall within the airway in order to mimic penetration up to some degree before the expiratory phase begins. The position, time, and velocity with which the droplet crossed the airway are monitored. We choose a droplet diameter of 1mm for investigation. Droplets are then tracked through the airway segment until they might disintegrate into small droplets, remain within the airway, aspirate to the lung (penetrant aspiration), or escape from the mouth-end of the airway (penetrant expulsion).

5.3 Results

5.3.1 *Droplet Breakup Characteristics*

Figure 33 shows a typical break-up event for a droplet initially released under a strong cough. The droplet first creeps down the wall by its own weight and subsequently disintegrates into child-droplets on encountering an increased flow velocity. It is observed that the number of child droplets and the number of subsequent break-ups in a strong cough are high. The trajectories of the initial droplet and the child droplets suggest that no child droplets are retained in the airway. Correspondingly, none of the droplets reached the trachea.



Figure 33: Droplet breakup under a strong cough

Figure 34 shows a typical break-up event for a droplet released under a weak cough. As mentioned in the previous section (methodology), the location, diameter, and other droplet properties are set to be the same as in the case of a strong cough. Although the droplet subsequently disintegrated into child-droplets, the number of child droplets and the number of subsequent breakups were not as high as in the case of a strong cough. The trajectories of the child droplets show that there was no reverse course in any of the droplets. All child droplets were finally retained in this case regardless of subsequent breakups.

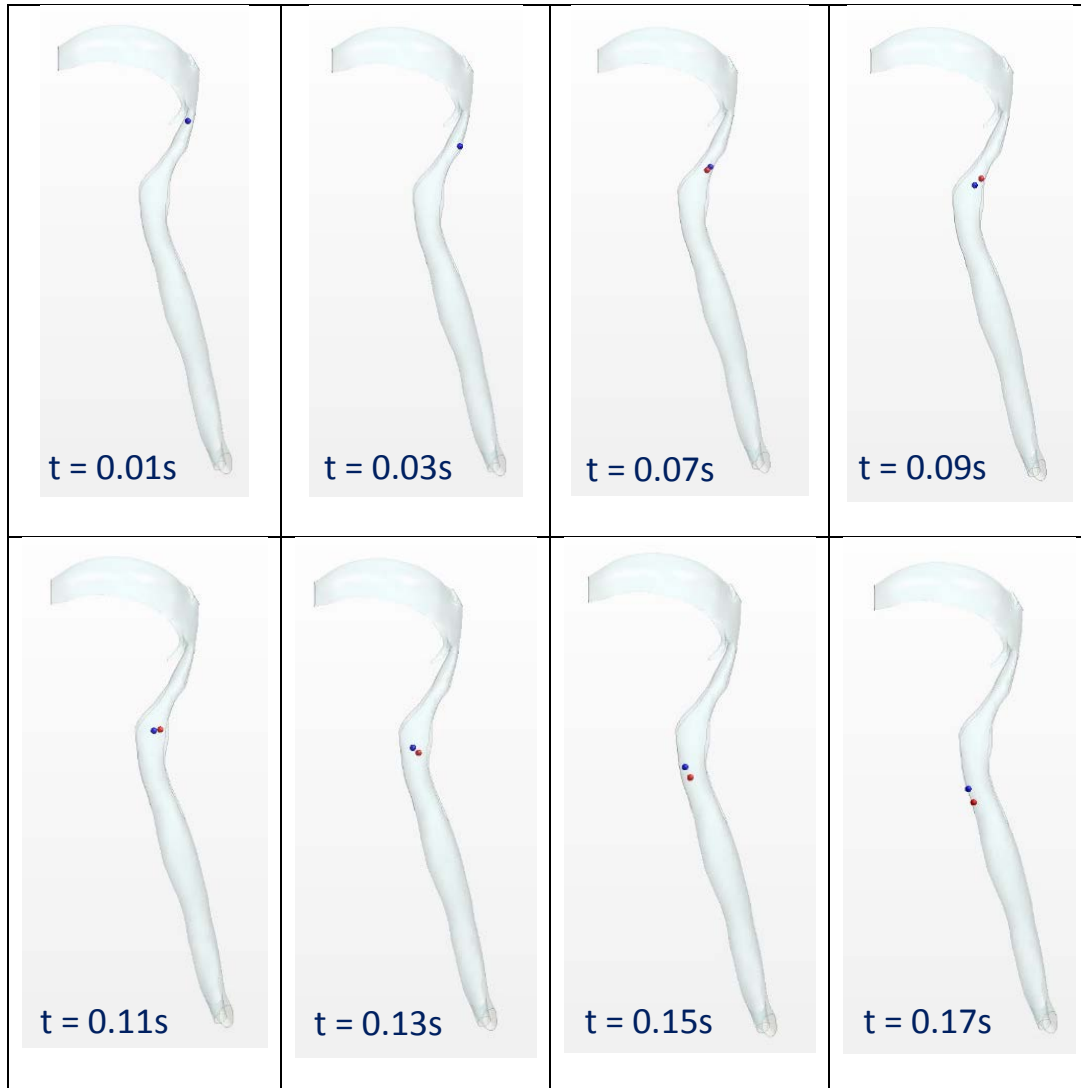


Figure 34: Droplet breakup under a weak cough

Figure 35 and 36 illustrate how the mean diameter of the droplet changes over its residence time within the airway for both strong and weak cough events considered in this study. At first, the creation of child-droplets reduced the mean diameter in multiple droplet events. Some of these child droplets then collided and coalesced with each other due to change in flow characteristics to form new droplets.

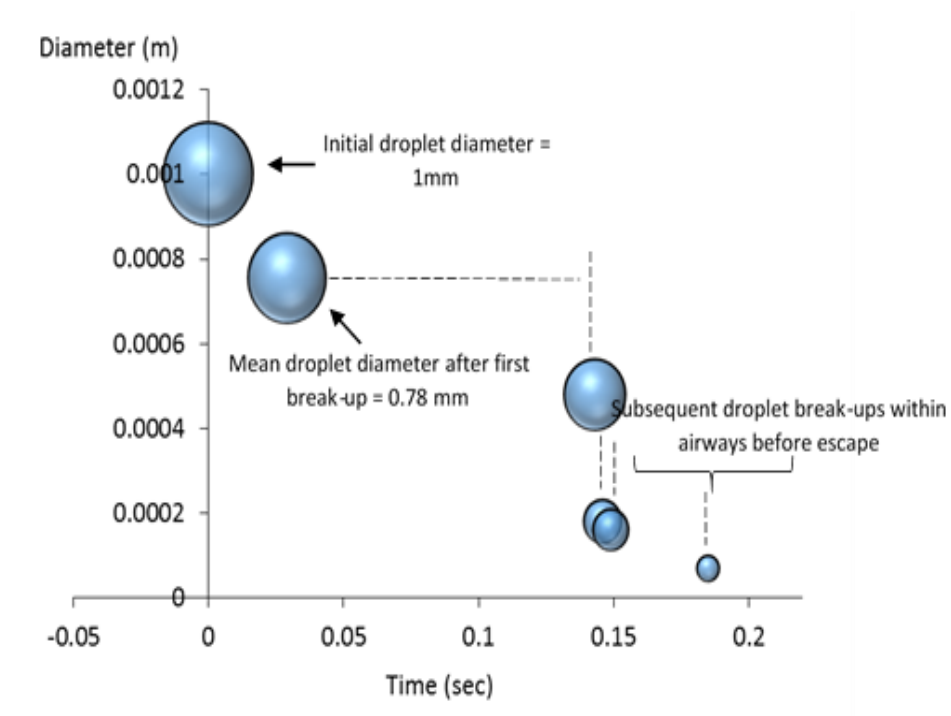


Figure 35: Droplet diameter variation under a strong cough event

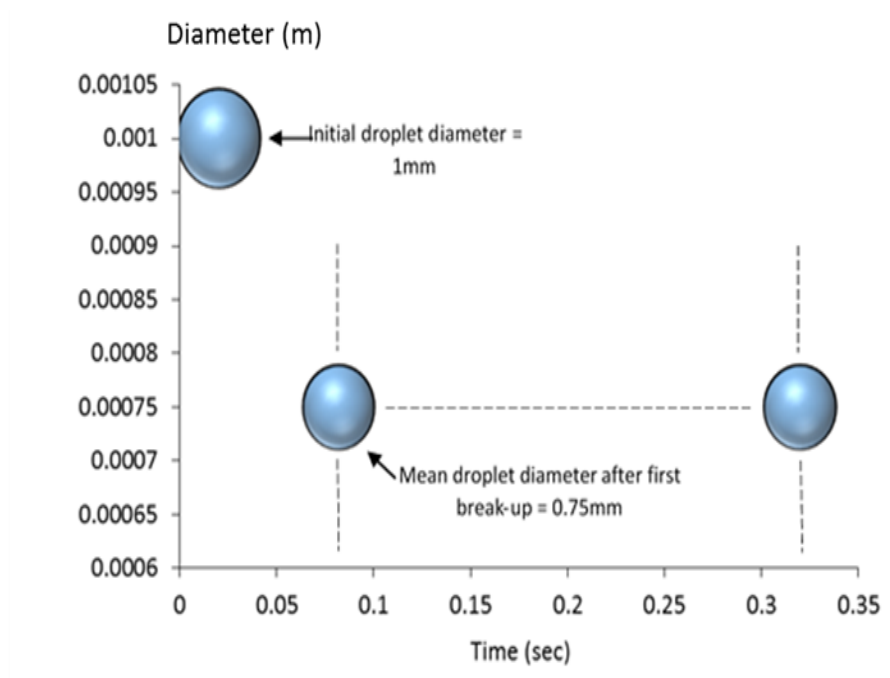


Figure 36: Droplet diameter variation under a weak cough event

Table 11 summarizes the behavior of the droplet over the duration of its residence time under both strong and weak cough events considered in this study.

Table 11: Summary of the Droplet Study

	Initial droplet size	No. of breakups	No. of child droplets created	Mean diameter of the final child droplet	Outcome of cough (Escaped or Retained)
Strong cough	1mm	5	9	0.06mm	Escaped
Weak cough	1mm	2	2	0.75mm	Retained

5.4 Discussion

5.4.1 Droplet Characteristics

The analysis of the droplet trajectory indicated that a strong cough caused more droplet breakup events. As discussed in the previous section, the aerodynamic forces exerted on the droplets cause secondary breakups. In a strong cough event, the relative velocity between the droplet and airflow was quite high, which thus increased the aerodynamic forces acting on the droplet. Multiple breakup events may lead to more small-sized child droplets compared to droplet behavior in a weak cough. In a weak cough event, the droplet was subjected to low aerodynamic forces, and it finally crept along the wall. The number of breakup events under a weak cough was not as high as in a strong cough, and the few droplet breakups led to child droplets of relatively larger size. The droplets with larger diameters have more mass, and the gravitational force was able to overcome the aerodynamic forces. The findings imply that more breakup events and smaller child droplet size aid the removal of penetrants from the airway. Our findings shed light on an unrecognized issue within cough evaluation and management. The

role of droplet collision, coalescence and re-formation as a risk marker, and the impact of scattering for microaspiration events may need to be further explored.

5.5 Summary

The present study was designed to assess the effect of variation of liquid droplet characteristics in the upper airway in patients with laryngeal disorders using imaging-based CFD technique. The results of the study spanned the behavior of the droplets within the airway in the event of a cough. The results suggest that the cough biomechanical model is better able to represent droplet behavior and promote the airway clearance in the presence of droplets towards realistic cough mechanism. The study still has a limitation. The location at which the droplet was released was fixed in the present model. It did not consider the random nature of the droplet origin within the airway. In the future, the study should be extended to include multiple release locations of more physiological relevance. Computational Fluid Dynamics can simulate the detailed cough flow and droplet behavior including a breakup, collision, and coalescence. Thus, CFD could be a powerful tool to assess penetrant behavior and aspiration pneumonia in patients with cough dysfunction such as patients with laryngeal function disorders including head and neck cancer, and neurological disease.

CHAPTER 6: FINITE ELEMENT MODEL OF OBSTRUCTIVE SLEEP APNEA WITH MUSCULAR COUPLING

6.1 Overview

A two dimensional (2D) finite element model of upper airway function was developed emphasizing the effects of dilator muscular activation on the human retro-lingual airway. The model utilized an upright mid-sagittal computed tomography (CT) of the human head and neck to construct relevant structures of the tongue, mandible, and the hyoid-related soft tissues, along with the retro-lingual airway. Reconstructions were discretized fluid and solid domains into finite element meshes used for the finite element (FE) model. Three cases were investigated: standing position; supine position; and supine position coupled with dilator muscle activation. Computations were performed for the inspiration stage of the breathing cycle, utilizing a fluid-structure interaction (FSI) method to couple structural deformation with airflow dynamics.

The spatio-temporal deformation of the structures surrounding the airway wall were predicted in general agreement with known changes from upright to supine posture on luminal opening and the distribution of airflow. The model effectively captured the effects of muscular stimulation on upper airway anatomical changes as well as flow characteristics relevant to airway narrowing with the supine position and enlargement with muscle activation. The smallest opening in this model in retro-lingual portion was predicted to occur at the epiglottic region in all the three cases considered, an unexpected vulnerable location of airway obstruction. The model also predicted that hyoid displacement would be associated with recovery from airway collapse. This information may be useful for building more complex models relevant to mechanisms and clinical interventions for obstructive sleep apnea.

6.2 Materials and Methods

6.2.1 *Reconstruction of Relevant Upper Airway Anatomy*

The biomechanical modeling procedure involves three major steps – geometry reconstruction, mesh generation and solution of governing equations. First, the two-dimensional (2D) geometry of the nasal and oral cavities and extending to the pharynx was reconstructed from the mid-sagittal plane obtained from a CT scan of a “normal” middle-aged male from the Radiology Unit at the Florida Hospital in Orlando. The boundaries of the different anatomical regions on the sagittal plane such as the airway, soft and hard palates, tongue, and epiglottis were identified based on grayscale threshold. Once the airway tissue structure was reconstructed, airway luminal volume was extracted using the void space between the pharyngeal walls and the oral cavity. The airway luminal volume was assumed to be occupied by air, representing the fluid domain in this study. Figure 37 shows the selected mid-sagittal plane of the CT image and the reconstruction process for airway structure and airway luminal volume.

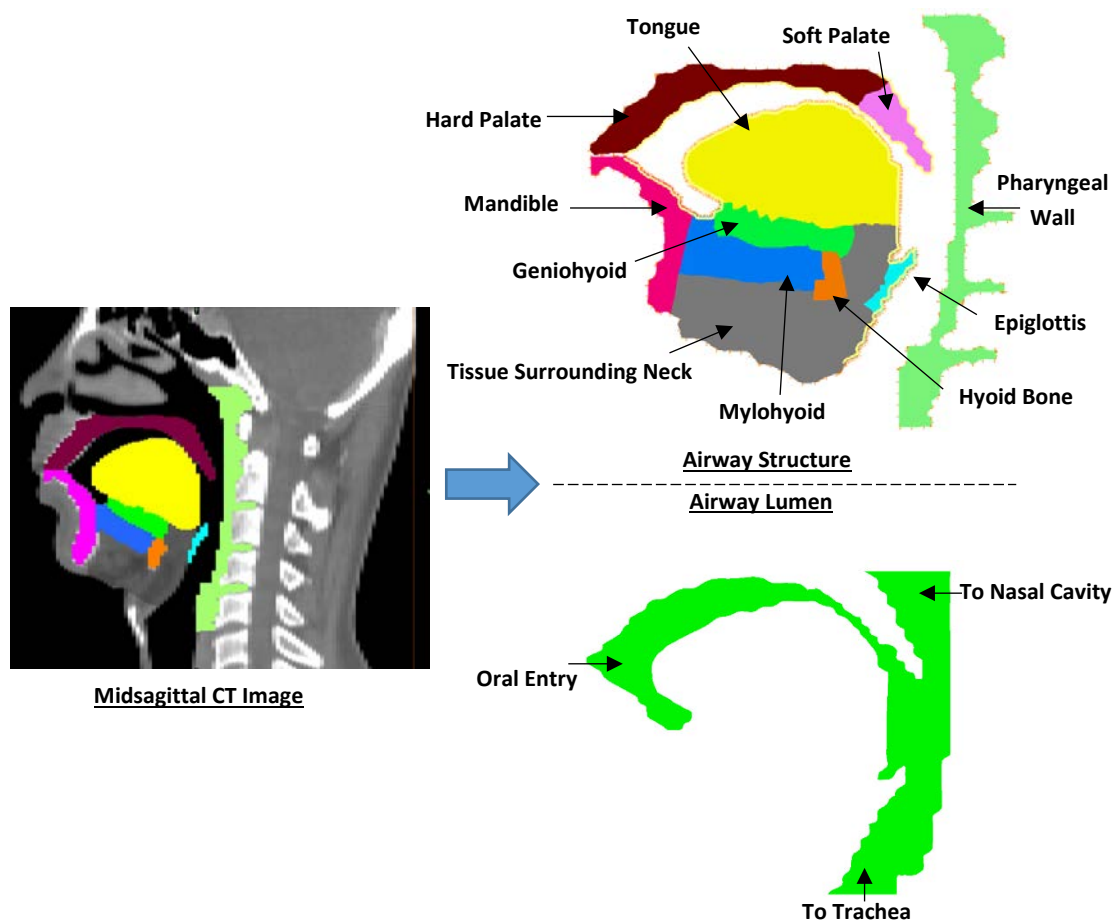


Figure 37: CT scan of the midsagittal plane representing airway structure and the reconstructed upper airway anatomy

Next, the fluid and solid domains were transformed (discretized) into finite elements using an unstructured mesh system to represent the complex geometry. In particular, we used non-uniform mesh sizes within the solid domain especially near the interface between the airway structure and fluid domain where property variations are expected to be largest. A uniform mesh size was adopted within the fluid domain. A mesh sensitivity study was then performed with three different element sizes in both the fluid and solid domains to establish a grid-

independent numerically-accurate solution. Figure 38 shows the two meshes utilized in the study.

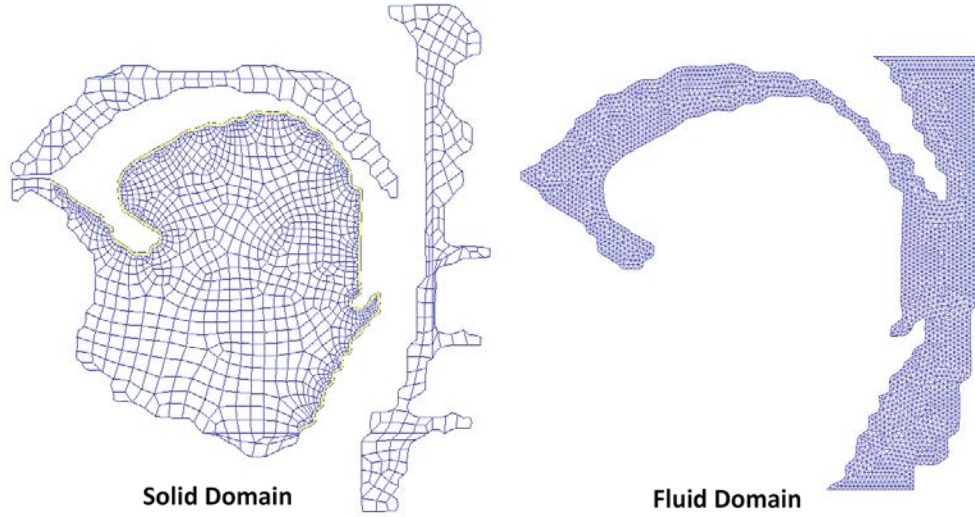


Figure 38: Finite Element meshes used for the FE model

6.2.2 Mathematical Formulation

The mathematical model of OSA consists of the physical equations governing structural stress and strain coupled with the airflow, in a Fluid-Structure Interaction (FSI) scheme. The basic principle behind this method is that, given any set of conditions, the unknown solution of the system which we wish to determine its lowest-energy configuration. The formulation of the governing equations is presented below.

The following stress-strain relationship expresses the governing equation for total stress in the structural domain:

$$\rho_s \frac{D^2(u_s)}{Dt^2} = \nabla \cdot (F \cdot S^s) + \rho_s f_g \quad (6-1)$$

where u_s represents the displacement vector, and ρ_s and f_g represent the density of the tissue and gravity force, respectively, F is the deformation gradient tensor, and S^s represents the

second Piola-Kirchoff stress tensor. Equation (6-1) in effect expresses a balance between the body acceleration force (on the left hand side) and externally applied loads (first term on the right) and the weight by gravity (second term on the right).

The governing equations for the fluid domain comprise the conservation of mass and momentum. The conservation of mass principle states that fluid in motion moves through a region with its mass conserved, and can be expressed in tensor notation by:

$$\frac{\partial \bar{u}_i}{\partial x_i} = 0 \quad (6-2)$$

where \bar{u}_i represents the time-averaged air flow velocities in the x and y directions.

Momentum conservation expresses Newton's second law of motion, which states that the sum of the external forces acting on the fluid equals the rate of a change of momentum of the fluid, thus:

$$\frac{\partial \bar{u}_i}{\partial t} + \bar{u}_j \frac{\partial \bar{u}_i}{\partial x_j} = -\frac{1}{\rho} \frac{\partial P}{\partial x_i} + \frac{\bar{u}}{\rho} \frac{\partial}{\partial x_j} \left[\mu \left(\frac{\partial \bar{u}_i}{\partial x_j} + \frac{\partial \bar{u}_j}{\partial x_i} \right) \right] \quad (6-3)$$

in which μ is dynamic viscosity, P is pressure, and ρ is air density. Air density and temperature are assumed to be constant. The pressure drop across the upper airway is typically small and the flow velocity is generally much smaller than the speed of sound, ensuring that airflow in the pharyngeal airway is essentially incompressible [122, 123].

The transport equations governing airflow in human airways were typically solved in the context of either laminar or turbulent airflow depending on the flow condition of interest. Although previous studies have suggested that airflow during breathing is laminar, there is evidence that flow transition or turbulence could occur locally with partial airway obstruction [124, 125]. Two most popular turbulence models used for airway flow simulations are the $k-\epsilon$

[126, 127], and $k-\omega$ [40, 128] models in which k represents turbulent kinetic energy, ε is the dissipation rate, and ω is the specific dissipation rate. However, previous work has shown that $k-\omega$ model is more appropriate to account for potential transitional and turbulent characteristics of the flow while satisfying acceptable accuracy in the laminar flow regime within the bulk of the upper airway[40]. Accordingly, we have adopted the low Reynold's number $k-\omega$ model in the present study. In order to allow for FSI analyses, fluid forces are applied to the solid, and the solid deformation in turn affects the fluid domain. The two domains are directly coupled through the interface conditions as described below.

The kinematic and dynamic conditions applied at the interface are the displacement compatibility and traction equilibrium, which can be expressed by:

$$d_f = d_s \quad (6-4)$$

$$n \cdot \tau_f = n \cdot \tau_s \quad (6-5)$$

where d_f and d_s are, respectively, the fluid and solid displacements, and τ_f and τ_s are, respectively, the fluid and solid stresses.

By coupling fundamental fluid dynamics governing equations (conservation of momentum and conservation of mass), with the above structural dynamics (stress-strain) equations, we can account for the FSI at the walls of the pharyngeal region to determine the effect of the obstruction and wall deformation on the airflow distribution under any condition.

6.2.3 Material Properties

The constitutive model utilized for soft tissue assumed materials that exhibit different elastic behavior. Soft tissues (tongue, geniohyoid, mylohyoid, tissue mass, and pharyngeal wall) was assumed to be hyperelastic materials following the Mooney-Rivlin constitutive model as the

tongue and other pharyngeal tissues are typically subjected to large displacement during upper airway collapse [127, 129, 130].

The hyperelastic materials exhibit stress-strain relation based on strain energy density function (W). The strain energy density function for the Mooney-Rivlin model can be expressed as a function of principal invariants (I_1, I_2) and material constants (C_1, C_2, D_1 , and D_2), thus:

$$W = C_1(I_1 - 3) + C_2(I_1 - 3)^2 + D_1(\exp(D_2(I_2 - 3)) - 1) \quad (6-6)$$

In the hyperelastic model, the stress tensor of previous Equation (6-1) is calculated from the relation:

$$S = \frac{\partial W}{\partial E} \quad (6-7)$$

The material constants of Equation (6-6) were adopted from the values presented in previous studies[131, 132]. The material constants are for soft tissues are listed in Table 12.

Table 12: Material constants used in the computation for hyperelastic model of soft tissues

Region	$C_1 \times 10^3$ (Pa)	$C_2 \times 10^3$ (Pa)	$D_1 \times 10^{-5}$ (Pa ⁻¹)	$D_2 \times 10^{-5}$ (Pa ⁻¹)
Tongue	1.628	0.77	1.24	2.61
Geniohyoid, Mylohyoid, Soft Palate, and Tissue mass	1.532	0.725	6.75	14.30

The bone and cartilaginous structures (epiglottis, hyoid bone, mandible, and hard palate) were assumed to have incompressible linear elastic properties to avoid unrealistically deformed

shapes from the forces and moments generated during airway wall deformations and dilator muscle activation. These structures were assumed to have Young's modulus of elasticity of 190 Mpa [133].

6.2.4 Boundary and Loading Conditions

For the genioglossus (the major upper airway dilator muscle), we assumed that muscle contraction occurred for 3s along an anterior-posterior direction. The strength of the contraction was induced through a time-force function in the FE model. In reality, the contraction of muscle tissues is activated through impulses delivered through the motor nerve network, for instance, the hypoglossal nerve for genioglossus in the tongue [134, 135]. Figure 39 shows the activation profile used in this study. The activation profile was used as a distributed load within the region of genioglossus muscle. We assumed the airway structure was initially at rest. Therefore, there was no activation for the first 3 s of the simulation in order to allow the airway structure to reach stable condition under gravity in the lateral-posterior direction.

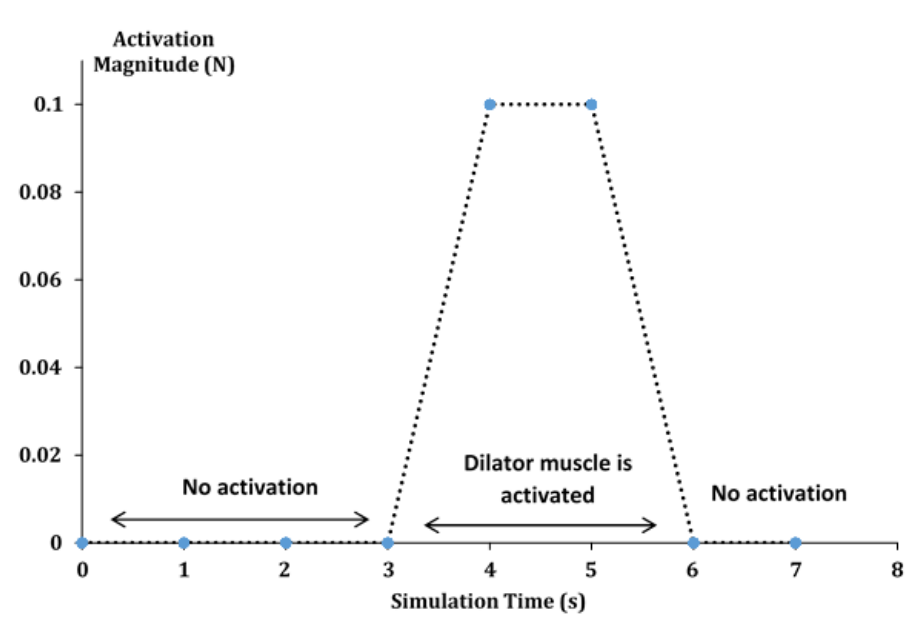


Figure 39: Time-Force activation of the genioglossus in the simulation

A no-displacement condition was imposed for the solid domain at three regions: the pharyngeal wall, the bottom surface of the neck tissue, and the upper palate. This condition implies the regions were assumed to be fixed during the simulated OSA process. A subatmospheric pressure was set at the nasopharynx to allow for the pressure drop caused by the flow resistance inside the nasal cavity. Therefore, the entrance to the nasal passage was assumed to be at -1 cmH₂O [32, 136]. A constant negative pharyngeal pressure (-5 cmH₂O) was imposed at the tracheal end of the oral cavity to simulate the inspiratory phase of the breathing cycle [33]. This pressure was chosen as the minimum pressure usually present at the initiation of an obstructed breath. Although the primary inhalation of airflow in this study was defined through the nasal cavity, the oral cavity was not entirely shut but opened slightly to allow air to pass through the mouth. The posterior tongue was still subjected to the pharyngeal pressure, but the oral cavity experienced atmospheric gage pressure. Due to the uncertainty of these parameters, the boundary and loading conditions used in the model were later analyzed for their sensitivity, and the outcomes of the study are presented in the Results section.

6.2.5 Computational Details

The above governing equations were solved subject to the boundary conditions using ADINA computer code [137]. The structural analysis utilized the dynamic implicit scheme with direct integration [138]. A total of 1,851 and 5,194 finite elements were utilized within the structural and fluid domains respectively. Each computation required about 150 minutes of CPU time on Intel Core i7 computer with 32 GB of memory.

6.3 Results

The model examined the effect of dilator muscle activation on three variables: the width of the airway lumen, hyoid bone elevation, and airflow distribution within the region at the level of the retro-lingual airway. In addition, in order to assess the effects of gravity, three cases were investigated; (a) standing (upright) position, (b) supine position, and (c) muscle activation in the supine position.

Figure 40 shows the predicted width of airway lumen at four reference levels; (i) soft palate, (ii) tongue, (iii) epiglottis, and (iv) larynx. First, the dimensions were recorded when the upper airway structure was in the standing position with gravitational effect in the vertical downward direction (Figure 40(a)). Figure 40(b) shows the result when the upper airway structure is in the supine position to mimic the sleeping posture. Figure 40(c) shows the corresponding result in the supine position when the dilator muscles are activated. All four reference levels in Figure 4 show a slight decrease in airway lumen size due to the weight of the tissue. This partial collapse is particularly noticeable at the soft palate, epiglottis and the laryngeal levels, as the epiglottis level defines the minimum gap. Figure 40(c) shows the recovery of the airway with the activation of the dilator muscles. Specifically, the dilator muscle activation causes the anterior wall of the airway lumen at all three levels to move forward and the cross-sectional dimensions of the airway to increase.

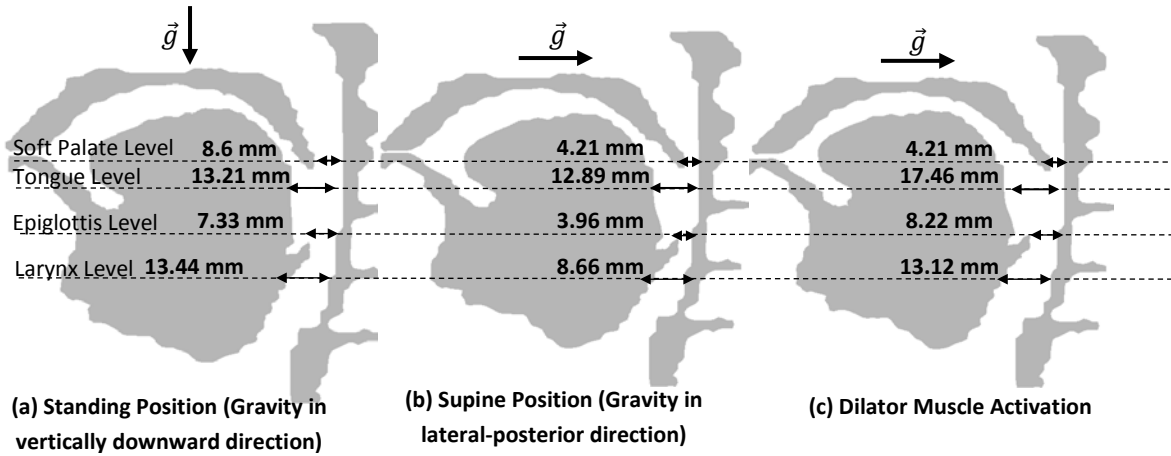


Figure 40: Predicted dimensional changes in the width of airway lumen at four reference levels. The width was measured in a lateral plane between the posterior wall of the oropharynx and the relevant anterior structure of the airway

Figure 41 shows the color-coded plot of the displacement magnitude within the airway structure for the three cases considered. We presumed that the upper airway structure in the standing position was under vertical downward gravity, thus indicating slight deformation in tongue and epiglottis region. When the upper airway structure is subjected to gravity in the supine position, the highest displacement leading to the collapse of the airway structure is observed at the tongue base and the region surrounding the hyoid bone. Figure 41(c) for the activation of the dilator muscles shows anterior and upward movements of the tongue, with the highest displacement occurring within the anterior region of the tongue. Figure 41(c) also indicates the recovery of the airway opening as the displacement reaches minimum again at the region surrounding the hyoid bone and the epiglottis.

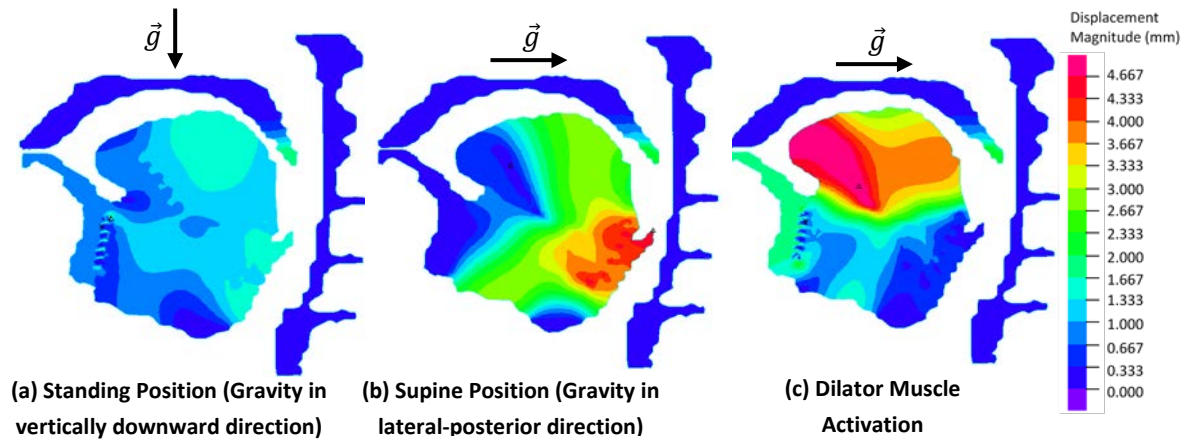


Figure 41: Predicted displacement magnitude in millimeters for three cases: (a) standing position; (b) deformed structure due to gravity in the supine position; (c) recovery with dilator muscle activation.

The location of the hyoid bone was also analyzed as part of this study due to its significance in structural integrity and function of the anterior pharyngeal wall [139]. With the movement of the tongue and the surrounding tissue during muscle activation, the hyoid bone elevated. Figure 42 shows the predicted hyoid bone elevation before and after activation of the dilator muscles. The hyoid bone is elevated by 1.853 mm with the activation of the dilator muscles for the specific input conditions utilized.

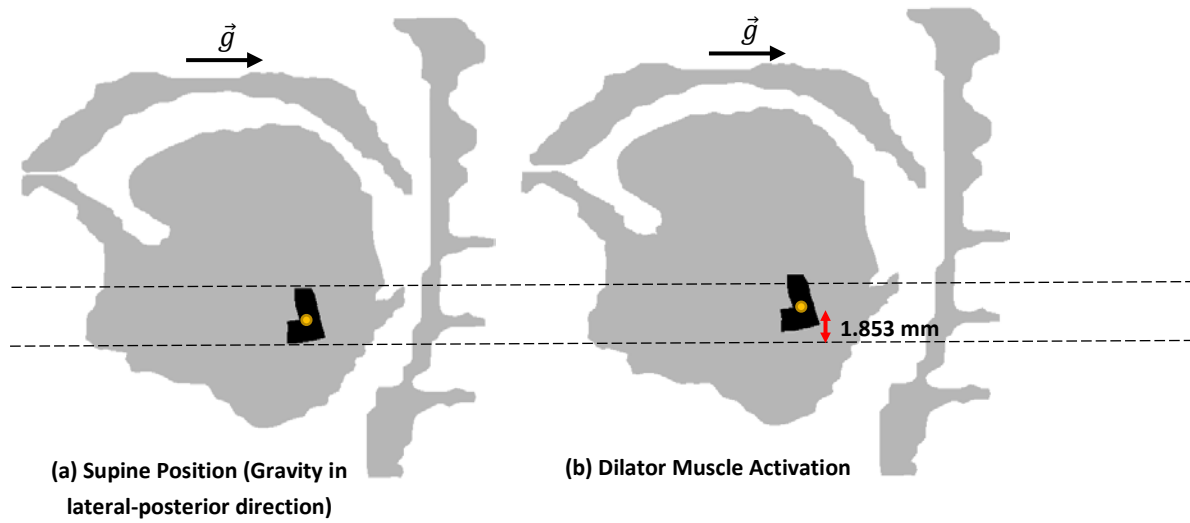


Figure 42: Hyoid bone highlighted in black before activation (a), Hyoid bone elevated during activation (b). Two horizontal reference lines are drawn to show the relative movement of the hyoid bone without and with activation.

The following section presents the changes in the airflow pattern through the airway lumen imposed by the structural deformation. We conducted an FSI analysis to study the effects of structural deformation on the airflow velocity and pressure distribution in the airway.

Figure 43 shows the predicted velocity distribution within the airway lumen for the three cases considered. Figure 43(a) presents the velocity distribution within the airway in the standing position. Air enters the airway from the nasal cavity and flows down through the airway lumen to the larynx. As expected, the highest velocity magnitude occurs near the axis of the airway lumen and the smallest velocities occur near the walls of the airway due to frictional effects are highest. There is no significant airflow into the oral cavity in both the standing posture (Figure 43(a)) and the case when dilator muscle is activated (Figure 43(c)). The result is consistent with the fact that a typical human being inhales air through the nose during breathing if no obstruction occurs. Some localized swirls are observed mostly near the irregular

morphological regions of the airway. The airflow, however, is found to be significantly disturbed in the supine position due to the partial airway collapse. Specifically, the velocity within the lumen increases significantly in the epiglottic region to compensate for the narrowing walls. Figure 43(c) shows a notable recovery of the air flow velocity in the airway lumen with activation of the dilator muscle. Dilator muscle activation causes the airway to expand and allows air to flow with minimal obstruction. In our model, we allowed the oral cavity to have a small opening which in turn allows air to flow freely through the oral cavity.

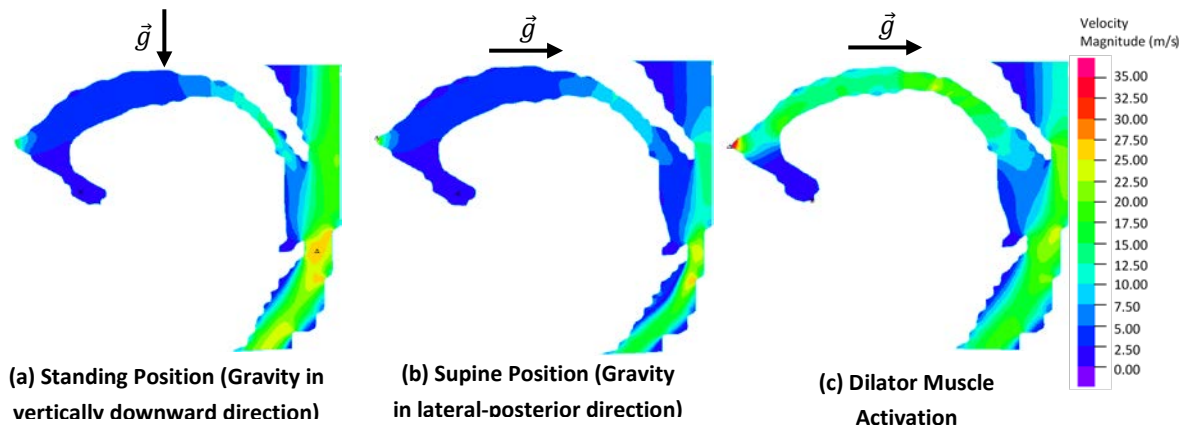


Figure 43: Predicted velocity magnitude in meters per second for three cases: (a) standing position; (b) deformed airway due to gravity in the supine position; (c) recovery with dilator muscle activation. The highest velocity magnitude is represented by the red

Table 13 shows the airflow rate based on the velocity magnitude, evaluated at the laryngeal level for the three cases considered. The airflow rate is calculated per unit depth as the model in this study represents only 2D plane. A nominal lateral width at the laryngeal level is 13.44mm. It is found that the airflow rate per unit depth is reduced by half in the supine position compared to the standing position, which is a significant impact on the inhaling process.

However, the dilator muscle activation restores partial recovery to the airflow rate as shown in Table 13.

Table 13: Airflow rate evaluated for three cases with the 2D model

Case	Average velocity (m/s)	Airflow rate (m ² /s)	Comment
(a) Standing Position (At rest)	15.87	0.213	Base case flow rate
(b) Supine Position (Gravity in lateral-posterior direction)	7.939	0.107	Airflow is reduced by 50% of case (a)
(c) Dilator Muscle Activation	12.101	0.162	Airflow is recovered to 75% of case (a)

Figure 44 shows the pressure distribution within the airway lumen for the three cases considered in the study. In the standing position (Fig. 44(a)), the lowest pressure is observed near the epiglottis (hypopharynx) within the airway lumen. When the airway structure is in the supine position (Fig. 44(b)), the partial airway collapse causes the pressure below the epiglottis to decrease significantly. This result is due to the increased resistance to airflow through the passage. This result can, in turn, cause a domino effect of further narrowing the lumen as the local low-pressure is inadequate to support the weight of the airway structure. Figure 44(c) shows the recovery stage under activation of dilator muscles. Specifically, with the muscle activation, the pressure distribution within the airway lumen recovers to the level observed in the standing position (in Fig. 44(c)). Slightly low pressure is observed within the oral cavity due to the mandibular advancement under dilator muscle activation.

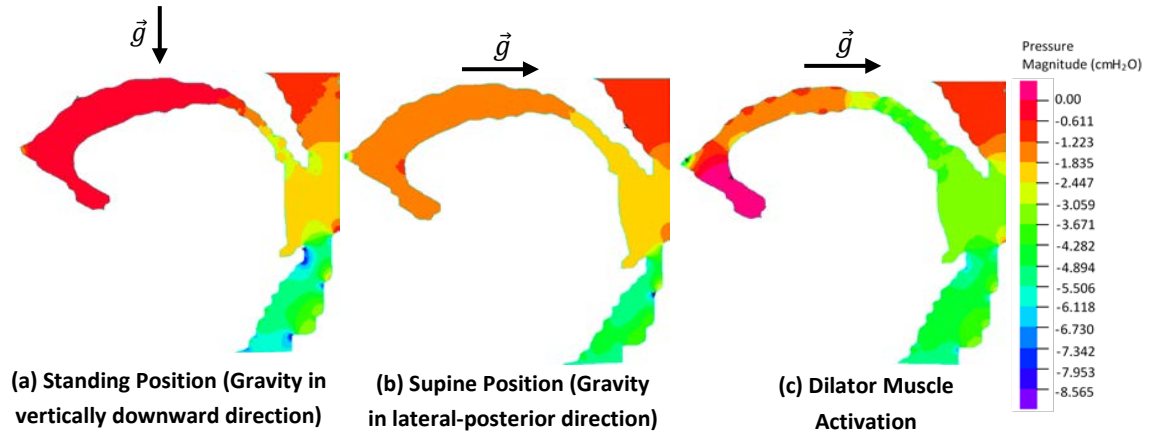


Figure 44: Predicted pressure magnitude in cmH₂O for three cases: (a) standing position; (b) deformed structure due to gravity in the supine position; (c) recovery with dilator muscle activation.

6.4 Sensitivity Analysis

Analyses were designed to assess the sensitivity of the FEM simulation to changes in some of the primary input parameters. Errors in simulation often arise from the assumptions made to characterize the physical behavior of the upper airway in OSA due to the simplification of the anatomy, assignment of tissue properties, modeling boundary conditions and external loads. In order to assess the sensitivity of our results to such constraints in our model, three parameters were selected based on the material elasticity, the time-force function used in muscle activation, and the inspiratory laryngeal pressure, all of which were either based on literature or experimental data. To assess the sensitivity of each of these parameters, we assigned separately $\pm 20\%$ and $\pm 10\%$ compensation intervals to each value used in the original model and simulated the response of the model for deformation and air flow rate at two distinct landmarks. Table 14 and Table 15 show the results of the sensitivity analysis in percentages for deformation and air flow rate, respectively, during the dilator muscle activation in the model.

6.4.1 Structural Deformation

The deformation was assessed based on the change in the width of the airway at the tongue level similar to a previous Figure 39 of the original (baseline) model.

Table 14: Sensitivity analysis for deformation assessed as change in airway width at tongue level

	+20% increase	+10% increase	-10% decrease	-20% decrease
Variable	(values presented as \pm percentage change from baseline result)			
Muscle Force	4.39	2.17	-2.22	-4.35
Laryngeal Pressure	0.05	0.018	-0.035	-0.05
Tissue Elasticity	0.086	0.04	-0.04	-0.11

6.4.2 Airflow

The air flowrate was assessed by using the nominal lateral width of the airway at the laryngeal level which is 13.44 mm. The average velocity was used to calculate the air flow rate at the same level where the nominal lateral width was evaluated.

Table 15: Sensitivity analysis for air flow rate assessed at a location close to the center of the airway lumen at epiglottis level

	+20% increase	+10% increase	-10% decrease	-20% decrease
Variable	(values presented as \pm percentage change from baseline result)			
Muscle Force	-0.58	-0.303	0.487	7.46
Laryngeal Pressure	15.56	12.85	-12.98	-16.01
Tissue Elasticity	-0.143	-0.01	0.031	0.21

The results in Table 14 suggest that the muscle force is most sensitive among the three model parameters considered in driving uncertainty of the tongue deformation. Table 15, on the other hand, shows that the laryngeal pressure is most sensitive in driving the uncertainty in the air flow rate within the lumen. Of interest, neither study exhibits any significant influence of varying the tissue elasticity on the deformation or velocity.

6.5 Discussion

This model captures a number of basic physiologic features relevant to upper airway structure as based on a CT image. It indicates an ability to couple fundamental fluid dynamics governing equations (conservation of momentum and conservation of mass), with structural dynamics (stress-strain). Second, this work presents simulations of interest using computational methods (i.e. Finite Element Analysis) regarding positional effects that reproduce observations in humans [140, 141]. Finally, the study begins to distinguish the effects of the state of muscle activation from those of elastic properties to assess outcomes on structure and airway functions using FSI analysis.

The model predicts a decrease in the pharyngeal luminal opening from the standing position to the supine position, which results in a reduction in the pressure in the laryngopharynx. This results in an increase in the resistance to the airflow which correlates with the relevant anatomical changes and outcomes relevant to patients with obstructive sleep apnea. We have also assessed the dimensional variations in the upper airway in three different longitudinal sections along the airway namely the tongue level, the epiglottis level, and the larynx level. Out of these three, in this formulation, the epiglottis section exhibits the smallest opening in all three cases considered. This result suggests a possible new location for airway obstruction, which may be examined for its impact on clinical treatment. In the supine position, the narrowing of the airway results in the higher pressure differential between the internal pressure and the external pressure imposed by the weight of the surrounding tissues, which makes the upper airway behave like a collapsible vessel.

The role of the hyoid bone in upper airway patency is to act as a pivot for transferring loads from one region of the pharyngeal tissue to the other [142]. Our model predicted the hyoid bone displacement associated with the recovery of airway collapse. We observed an elevation of the hyoid bone when the dilator muscles were activated. The model prediction suggests that the upward movement of the hyoid bone may prompt the movement of the tissue surrounding the anterior wall of the airway to recover from collapse [139]. This particular result is in agreement with the observations made in previous FEM modeling studies where the limited hyoid bone movement caused reduction of transferring forces to the tissues below the hyoid bone, resulting in little to no tissue displacement in the region [142].

Flow resistance and the risk of collapse of the upper airway are evident in the supine position, constituting one causal pathway to pharyngeal closure. Adverse changes in the upper airway

can be recovered through dilator muscle activation so that a failure to adjust neuromuscular activation is crucial to the initiation of the obstructive event. The FEM model presented in this study has elucidated the flow-structural factors determining airway collapse in the supine position, and the potential for its mitigation by dilator muscle activation. This observation is consistent with the change in pharyngeal patency observed in humans moving from the upright to supine posture; in this study the change in acoustic size of the pharynx was not the result of a change in lung volume or a reduction in sub-mental EMG activity; in fact EMG activity increased while pharyngeal cross-sectional area was reduced in the supine posture [140].

The findings of the sensitivity analysis begin to address a gap in understanding physiological mechanisms relating to this complex system, which can be modified for effects on airflow dynamics [63]. The analysis was for the purpose of testing initial assumptions and was not exhaustive for all the degrees of freedom regarding driving pressures and directional actions of muscle elements. Nevertheless, it suggests that model parameters for muscle activation could be more carefully described to reduce uncertainty and that the elastic properties of the system for its dynamic functions may not contribute as much as one might assume. It provides a roadmap for data collection to detail features (muscle orientation, driving pressures, and anatomic set-points along the airway) that regulate airflow in health and disorders like obstructive sleep apnea.

One limitation of this study is that the current model assumes the upper airway structure to be two-dimensional (2D), i.e., planar, while in reality, the upper airway geometry is three-dimensional, and that the activation of the muscle could have asymmetric effects. As well, we ignore changes in the structure and airflow along the lateral dimensions of the airway which are known to affect airway function and are modified by surgical revisions for treatment of

OSA [63, 143]. A second limitation is a focus on the tongue and its immediate effects on the retroglossal airway size; there is emerging evidence that OSA can be a multi-site event involving the retropalatal as well as the retro-lingual airway [144, 145]. It is suggested that the present model be expanded to a 3D fluid-structure interaction simulation of the upper airway in a future study. In the long term, a FEM model could be used to mimic various conditions associated with OSA and patient treatment by changing geometrical, physical, and material parameters in response to therapy such as Continuous Positive Airway Pressure (CPAP), oral appliance, or unilateral hypoglossal muscle activation.

In summary, this model can reproduce physiologic findings in humans concerning the effects of position on pharyngeal patency and neuromuscular activation. The value of such a model in going forward is to encourage the development of more sophisticated models that include more degrees of freedom, the possibility of multi-site collapse and effects of specific muscles alone or in combination on upper airway size and shape, compliance, and stability to the point where predictions can be made. General, as well as more individual models, could be used to assess the impact of anatomic and non-anatomic therapy for OSA.

CHAPTER 7: MATHEMATICAL MODELLING OF TONGUE DEFORMATION IN ORAL PHASE OF SWALLOW IN PATIENTS WITH HEAD AND NECK CANCER³

7.1 Overview

A computer-based, biomechanical model of swallow may provide a means of quantifying cancer-related changes to tongue tissue, as well as the resultant changes to tongue movement during the swallow. Cancer localized to the tongue is often characterized by increased stiffness in the affected region. This stiffness affects swallow in a manner that is difficult to quantify in patients. The objective of this study is to develop a biomechanical model to simulate the spatiotemporal deformation of the tongue during oral phase of swallow in patients with cancer of the tongue base. The model involves finite element analysis of the three dimensional model of the tongue reconstructed from magnetic resonance images (MRI). The tongue tissue is assumed to be hyper-elastic. In order to examine the effects of tissue change (increased stiffness) due to the presence of cancer localized to the tongue base, various sections of the 3D geometry are modified to exhibit different elastic properties. Three cases are considered, representing the normal tongue, a tongue with early-stage cancer, and tongue with late-stage cancer. Early and late stage cancers are differentiated by the degree of stiffness within the base of tongue tissue. Analysis of the model suggests that healthy tongue has a maximum deformation of 9.38mm whereas tongues having mild cancer and severe cancer have a maximum deformation of 8.65mm and 6.17 mm respectively for the specific conditions

³ *The materials of this Chapter have been previously published in:* Ilegbusi, O. J., Kuruppumullage, N., Silverman, E., Lewis, V., Lehman, J., & Ruddy, B. H. (2016). Mathematical modelling of tongue deformation during swallow in patients with head and neck cancer. *Mathematical and Computer Modelling of Dynamical Systems*, 22(6), 569-583.

investigated. Biomechanical modeling is a useful tool to explain and estimate swallowing abnormalities associated with tongue cancer and post-treatment characteristics.

7.2 Materials and Methods

7.2.1 *Reconstruction of Three-Dimensional Tongue Geometry*

The first step in the development of the biomechanical model is to define the complex structure of the tongue by analysis of de-identified MRI images obtained from patients at the Florida Hospital in Orlando, FL. The images were acquired using the Philips Medical Systems scanner. The image dataset constitutes a sequence of MRI scans representing the head and neck anatomy. The image resolution was 400 x 400pxl with a slice thickness of 5mm. All images were stored in DICOM file format and later input into the Mimics image processing software [90] for analysis and reconstruction of the 3D geometry of the tongue.

The steps involved in the reconstruction process are illustrated in Figure 45. The process begins with the sequential delineation of tongue boundaries in each image slice. Once completed, the boundary identifiers are transferred to a mask, followed by the calculation and outlining of the 3D tongue morphology. The geometry is then further refined to improve quality.

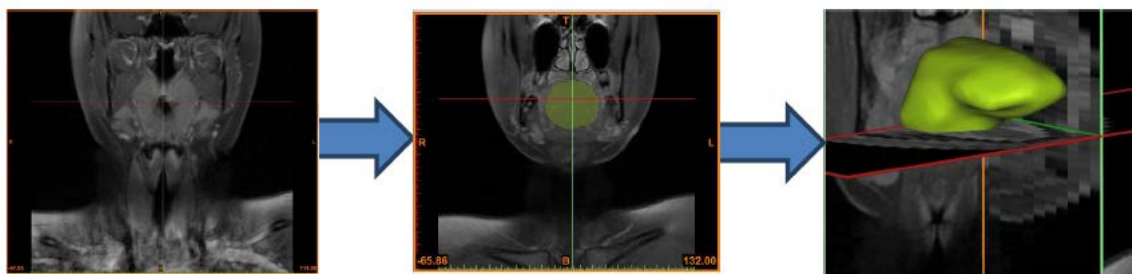


Figure 45: Steps involved in reconstruction of 3D tongue geometry

The next step is to generate computational meshes from the reconstructed geometry. This is achieved with the 3-Matic software [91], which is also used for subsequent mesh refinement to improve quality. Tetrahedral elements are then used to fill the volume meshes. Tetrahedral elements were chosen in order to reduce meshing problems associated with a complex geometry like the tongue. Uniform mesh sizes were also used to prevent unnecessary distortion of the elements. Figure 46 illustrates the type of mesh generated (a), and a cut-out view of the mesh (b).

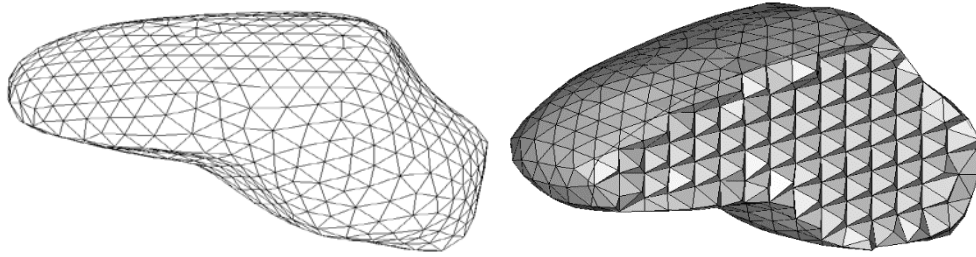


Figure 46: volumetric mesh generated (a), and cut-out view (b)

7.2.2 Mathematical Formulation

In developing the mathematical model to solve for the tissue deformation during swallow, it is assumed that the tongue can experience large deformation and nonlinear constitutive response. Lagrangian formulation expresses the equilibrium of the tongue at time $t + \Delta t$, using the principle of virtual displacement in tensor notation thus;

$$\int_{t+\Delta t_v} {}^{t+\Delta t}\tau_{ij} \delta_{t+\Delta t} e_{ij} d^{t+\Delta t}v = {}^{t+\Delta t}R \quad (7-1)$$

where, $\tau_{ij} \equiv$ Cauchy Stress Tensor, $\delta_{t+\Delta t} e_{ij} \equiv$ Strain Tensor corresponding to virtual displacement, ${}^{t+\Delta t}v \equiv$ Volume at time $t + \Delta t$, ${}^{t+\Delta t}R \equiv$ External forces, and $d^{t+\Delta t}v \equiv$ Differential volume element at time $t + \Delta t$.

Using the definitions of Second Piola Kirchoff stress tensor and Green Lagrangian strain tensor, the relationship in Equation (7-1) can be transformed to:

$$\int_{t+\Delta t_v} {}^{t+\Delta t}\tau_{ij} \delta_{t+\Delta t} e_{ij} d^{t+\Delta t}v = \int_{v^0} {}^{t+\Delta t}{}_0S_{ij} \delta_0^{t+\Delta t} \epsilon_{ij} d^0v \quad (7-2)$$

where, ${}^{t+\Delta t}{}_0S_{ij} \equiv$ Second Piola Kirchoff Stress Tensor, $\epsilon_{ij} \equiv$ Green Lagrangian Strain Tensor, and $d^0v \equiv$ Differential volume element at time $t = 0$.

Then, the equation of motion in total Lagrangian formulation can be rewritten thus;

$$\int_{v^0} {}^{t+\Delta t}{}_0S_{ij} \delta_0^{t+\Delta t} \epsilon_{ij} d^0v = {}^{t+\Delta t}R \quad (7-3)$$

By linearizing the equation of motion using approximations for Second Piola Kirchhoff stress and Green Lagrangian strain tensor also considering the incremental decomposition of stress and strain tensors, the following equation is obtained[146].

$$\int_{0_v} {}_0C_{ijrs} {}_0e_{rs} \delta_0 e_{ij} d^0v + \int_{0_v} {}^t_0S_{ij} \delta_0 \eta_{ij} d^0v = {}^{t+\Delta t}R - \int_{v^0} {}^t_0S_{ij} \delta_0 e_{ij} d^0v \quad (7-4)$$

where, ${}_0C_{ijrs} \equiv$ Constitutive Tensor incorporates material properties of configuration at time 0, ${}_0e_{rs} \equiv$ Linear incremental strain, $\delta_0 e_{ij} \equiv$ Virtual linear incremental strain, $\delta_0 \eta_{ij} \equiv$ Virtual Non-linear incremental strain, and $d^0v \equiv$ Differential volume element at time $t = 0$.

Equation (7-4) can be used to calculate incremental displacement over Δt , which is then used to calculate approximations to the displacements, strains and stress to time $t + \Delta t$. The total Lagrangian formulation essentially expresses the equations in incremental continuum mechanics, including all nonlinear effects such as large displacement, large strain and material non-linearity.

The above formulation enables the use of numerical methods such as finite element analysis (FEA) to calculate the displacement in the tongue under applied loading. The inputs to the FEA are the material properties, loading and boundary conditions. In dynamic analysis, the applied external forces include inertia forces as part of the body forces. Assuming that the mass of the body is preserved, the mass matrix can be evaluated using the initial configuration. Therefore the finite element formulation of the Equation (7-4) for dynamic analysis with implicit time integration is expressed as:

$$M^{t+\Delta t}\ddot{U} + ({}^tK_L + {}^tK_{NL})U = {}^{t+\Delta t}R - {}^tF \quad (7-5)$$

where, $U \equiv$ Nodal displacement, $\ddot{U} \equiv$ Nodal point acceleration, $M \equiv$ Mass Matrix, ${}^tK_L \equiv$ Linear stiffness matrix, ${}^tK_{NL} \equiv$ Non-linear stiffness matrix, and ${}^tF \equiv$ Nodal point force vectors

In the above finite element formulation, ${}^tK_L U$, ${}^tK_{NL} U$, and tF are obtained from finite element evaluations of the first, second and fourth terms of Equation (7-4) respectively. For materials undergoing large deformation, the formulation is further modified to include the displacement/pressure relationship to allow for the approximate incompressibility of tongue thus;

$$\begin{bmatrix} M_{uu} & 0 \\ 0 & 0 \end{bmatrix} \begin{Bmatrix} \ddot{U} \\ \ddot{P} \end{Bmatrix} + \begin{bmatrix} (K_L + K_{NL})_{UU} & (K_L + K_{NL})_{UP} \\ (K_L + K_{NL})_{PU} & (K_L + K_{NL})_{PP} \end{bmatrix} \begin{Bmatrix} U \\ P \end{Bmatrix} = \begin{Bmatrix} {}^{t+\Delta t}R \\ 0 \end{Bmatrix} - \begin{Bmatrix} F_U \\ 0 \end{Bmatrix} \quad (7-6)$$

in which $(K_L + K_{NL})_{UU}$, $(K_L + K_{NL})_{UP}$, $(K_L + K_{NL})_{PU}$ and $(K_L + K_{NL})_{PP}$ represent the coefficients within the stiffness matrices. In the mixed pressure/displacement relation, \hat{u} is the nodal displacement, \hat{p} is the element internal pressure, ${}^{t+\Delta t}R$ is the applied force at the next time step, and F_U represents the nodal point force vectors being evaluated. Finally, Equation (7-6) is solved to obtain the approximations to the displacement and acceleration. The linearization of Equation (7-3) may introduce errors and instability to the solution. Therefore,

equilibrium iterations are performed in each load step until, the assumptions for the variation of material constants and numerical time integration are satisfied.

7.2.3 Material Properties

The tongue is assumed to be a hyper-elastic material based on previous studies [87]. The hyper-elastic material exhibits stress-strain relationship derived from Strain energy density function (W). The strain energy density function has high order terms of invariants and material constants. These material constants are chosen in this study to fit the experimental data. The strain energy density of the Mooney-Rivlin hyper elastic model adopted can be expressed as a function of two principal invariants I_1 , I_2 and five constants C_1 to C_5 , thus,

$$W = C_1(I_1 - 3) + C_2(I_1 - 3)^2 + C_3(I_2 - 3) + C_4(I_2 - 3)^2 + C_5(I_1 - 3)(I_2 - 3) \quad (7-7)$$

The invariants are given in terms of the components of the Cauchy-Green deformation tensor C_{ij} .

$$I_1 = C_{kk}, I_2 = \frac{1}{2}[(I_1)^2 - C_{ij}C_{ij}] \quad (7-8)$$

In the hyper-elastic model, the Second Piola Kirchhoff stress of previous Equation (7-4) is calculated from the relation:

$${}^t_0S_{ij} = \frac{\partial W}{\partial {}^t_0\epsilon_{ij}} \quad (7-9)$$

Three parametric test cases were considered in this study: a normal tongue (Case 1), a tongue with early stage, localized tongue-base cancer (Case 2), and a tongue with later stage, localized tongue base cancer (Case 3). The choice and size of the affected region, though arbitrary, were guided by associated medical literature [147].

The stress-strain curve which represents the elastic behavior for the healthy tongue was obtained from the indentation experiment on fresh human cadaver tongue [148]. However, the tissue elastic properties do not exist and have not been established for tongue with cancer. We hypothesized that cancer of the tongue base will also stiffen adjacent tissue in the affected region, therefore two additional stress-strain curves shown in Figure 47 were used to represent the parametric test cases.

The stress-strain curves used for the cancer-affected region of the tongue were selected to increase the stiffness of the material in that region over that of Case 1. Case 3 was assigned the highest stiffness to mimic late-stage cancer while Case 2 was assigned constant values between those assigned to Case 1 and Case 3 in order to simulate early-stage cancer. The pathological changes are generally correlated with changes in tissue stiffness of soft tissues in human body such as cancers of the breast which appear extremely stiff [149-151]. Therefore, the stress-strain curves for the cases of severe and mild cancer were compared to the findings for breast cancer to verify that they follow similar behavior [152].

The next step is to estimate the hyper-elastic material constants for the Mooney Rivlin model adopted for the study. The material constants are listed in Table 16 for the three cases considered. These constants were estimated from curve-fitting of the data in Figure 47. Although a sensitivity analysis using experimental data would have been desirable in assigning values to Case 2 and Case 3, the material constants assigned for cancer tissue here are merely used for qualitative assessment of the effect of tumor on tongue deformation. Thus the values used are considered adequate to meet the immediate objective of the study.

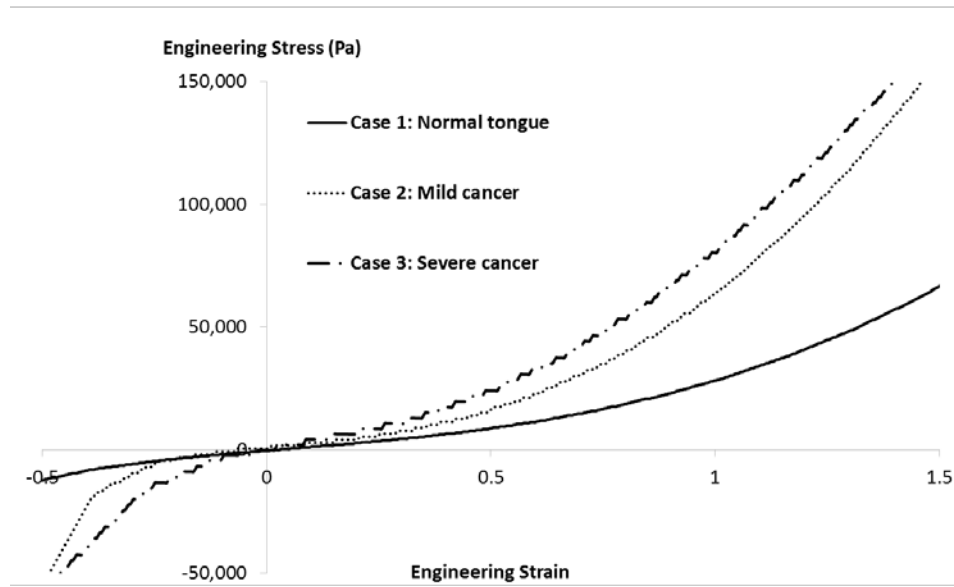


Figure 47: Stress-strain curves used for the three parametric cases considered in the study

Table 16: Material constants used in the computation (values in kPa)

	C_1	C_2	C_3	C_4	C_5	Bulk Modulus
Case 1 (Normal tongue)	4.367	-1.908	2.077	-1.851	0.530	2459
Case 2, (Tongue with mild cancer)	5	-2.5	4.5	-2.0	0.63	4000
Case 3 (Tongue with severe cancer)	6.5	-0.5	7.0	-1.0	0.1	6000

7.2.4 Loading and Boundary Conditions

The tongue is attached to the base of the mouth near the hyoid bone. Therefore this base is fixed in the computational model. The swallowing process proceeds by the activation of the tongue muscles. It is a major challenge to identify the specific muscles involved and in order to define the appropriate force applied during the swallowing process. Therefore the tongue

movement is induced in this study by applying normal stress to the elements on the top surface of the tongue. The normal stress applied to the tongue during swallow can be obtained from tongue pressure measurement [152]. In the oral stage, the tongue basically elevates to meet the hard palate that pushes bolus onto the upper part of the tongue posterior. The force and time duration in the analysis considered here only cover the propulsion stage lasting for 200ms. We assume that the tongue is initially at rest. The pressure load is then gradually increased at various sections on the surface of the tongue. The profiles of the pressure utilized in the study are shown in Figure 48. The various profiles a,b,c indicate stresses applied on different surfaces of the tongue as illustrated in Figure 49. These profiles in sequence simulate the bolus feeding movement of the tongue.

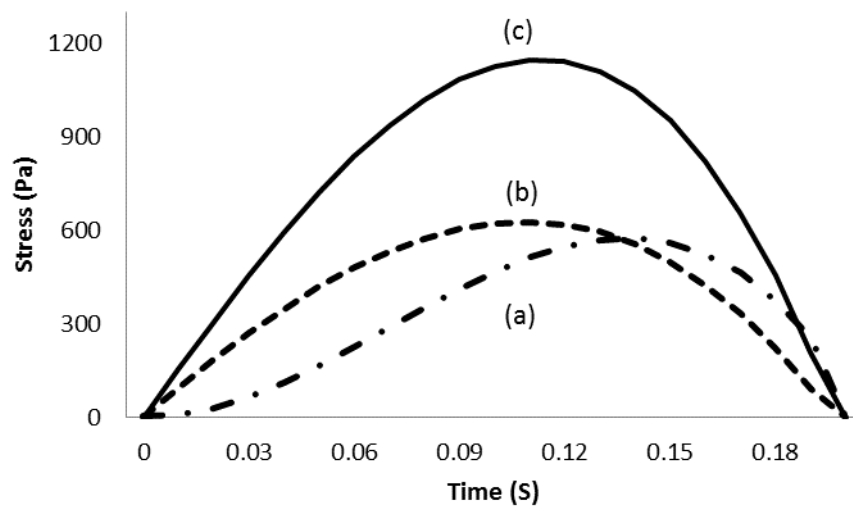


Figure 48: Applied stress at different sections of tongue surface during propulsion stage of swallowing

Specifically the locations on the tongue surface on which the pressure profiles (stresses) applied are obtained from a previous study [153] and are shown in Figure 49. In effect, Profile 1 is imposed on Surface 1, Profile 2 is imposed on Surface 2 and Profile 3 is imposed on Surface

3. Surface 4 represents the location where the tongue is connected to the oral cavity near the hyoid bone. Thus, the meshes within surface 4 are fixed in the biomechanical model.

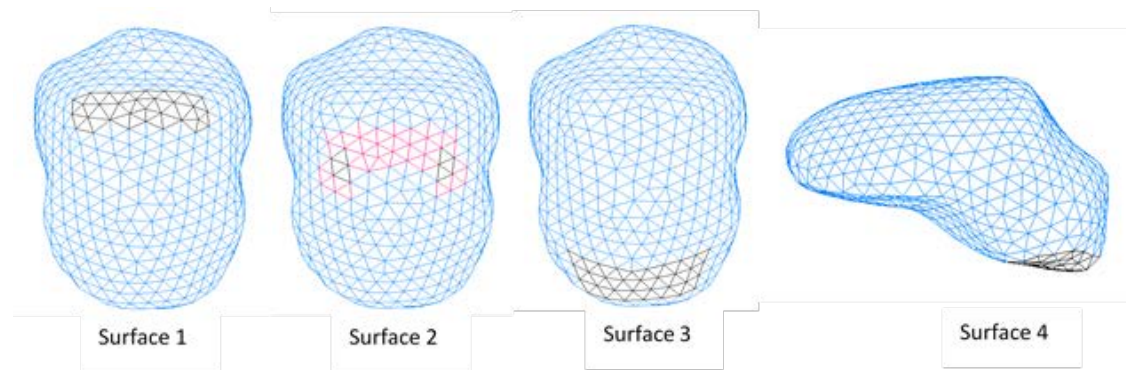


Figure 49: schematic sketch indicating sections of tongue surface on which pressure or fixity is applied

7.2.5 Representation of Localized Cancer

Figure 50 shows the location of the cancerous lesion on an external (a) and sagittal (b) view. The affected part of the tongue is highlighted on the surface of the tongue and, within the sagittal views, is assumed to have spread into the tongue in all dimensions as illustrated in (b). Although tissues affected by cancer can demonstrate varying tissue abnormalities and properties, for the purposes of this investigation, we assumed uniformly abnormal tissue properties within the affected region.

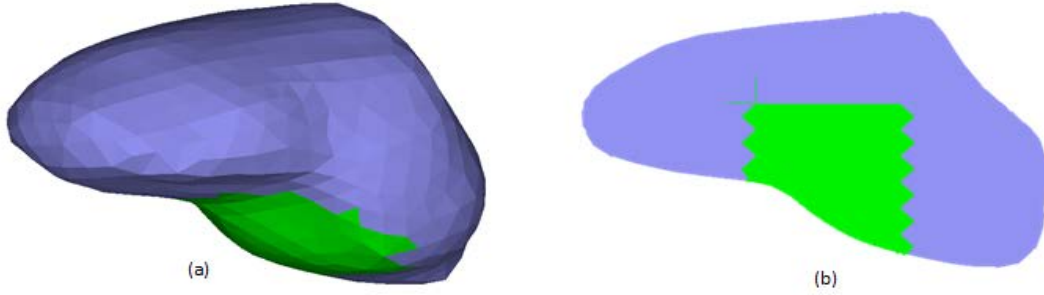


Figure 50: Schematic sketch indicating location of localized cancer in (a) external view, and
(b) sagittal view

7.2.6 Computational Details

The finite element model was constructed using ADINA [137] computer code. The dynamic-implicit analysis using direct integration for structural problems is chosen in this analysis. In nonlinear analysis, the equilibrium iterations are performed to the incremental finite element equilibrium equation given in Equation 6. The study utilized Bathe Method to divide sub steps in time increments which is based on conserving energy and momentum [154]. In the first sub step, the displacement and acceleration are solved using trapezoidal rule which are then solved using a backward 3-point Euler method in the second sub step.

The implicit method is unconditionally stable for larger time steps and creates no issues as the time step size exceeds critical time step. The swallow motion of the tongue is a low-speed dynamic problem that has a longer solution time than the time it takes the wave to propagate through an element. Therefore, implicit method is the best option. However, the implicit method requires more time steps and each time step requires more iterations to converge. There were no convergence errors or convergence difficulties in all simulations. There were four iterations in some time steps to reach the equilibrium. This is mainly due to the non-linear

behavior of hyper-elastic material. The computer used in the simulation is equipped with Intel Core i7 processor with 8 GB of RAM memory.

7.2.7 Mesh Sensitivity Analysis

In order to evaluate mesh quality and assure numerical accuracy of predicted results, the finite element mesh was initially refined until a critical result, such as the maximum displacement in a specific location converges. Table 17 shows the details of the five different meshes used for the sensitivity study. The predicted displacement at the tongue tip was monitored for each mesh under similar loading and boundary conditions, and plotted against the number of elements as shown in Figure 45.

Table 17: Details of meshes used for sensitivity analysis


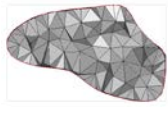

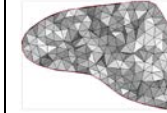
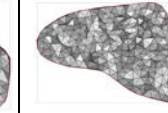
					
No. of elements	1927	2530	3534	8134	15582
No. of nodes	687	768	916	1792	2809

Figure 51 shows that as the mesh density increases, the monitored displacement monotonically increases initially. Subsequently, the result becomes essentially invariant with mesh size beyond the mesh with 8674 elements. This mesh is considered numerically accurate and used for all computations reported in this study.

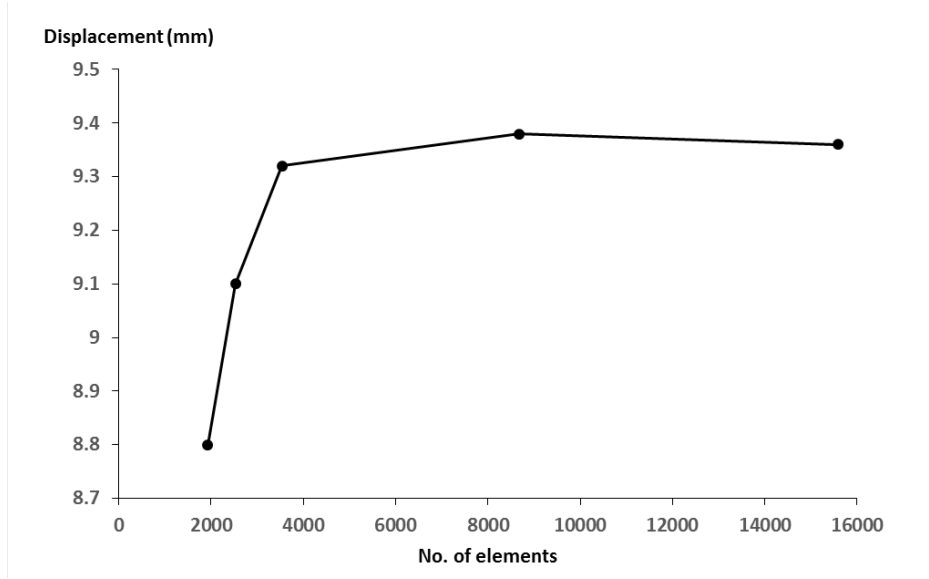


Figure 51: Displacement of tongue tip for different mesh sizes

7.3 Results

Three parametric test cases are considered representing normal tongue without cancer (Case 1), tongue with mild cancer of the base (Case 2) and tongue with severe cancer of the base (Case 3) as discussed in a previous section 3.3 and. Figure 52 shows the predicted color-coded deformation at the mid-plane of the tongue for Case 1 at various instances when a varying force is applied to the tongue to simulate the propulsion stage of the swallowing process. The results at 8 instances are presented at 20ms intervals. The dark blue color represents minimum deformation while red color is the maximum. The distribution in general starts with the lowest deformation at the base where the tongue is fixed, to the largest at the tip. This pattern is maintained at subsequent instances, with the magnitude of the deformation at the tip progressively increasing (region of red color enlarges from the tip region towards the base). The maximum deformation is reached at an intermediate stage ($t = 110$ ms) which corresponds approximately to the peak applied force profile shown in a previous Figure 48.

This observed pattern is consistent with the fact that the tongue typically elevates during the propulsion stage to push bolus into the pharynx and the process begins with the upward motion (large deformation) of the oral tongue. Thus the oral tongue region exhibits the largest deformation in all cases relative to the base throughout the duration of the propulsion stage. It is remarkable that progressive stratification of the deformation occurs in the tongue, reaching a maximum intensity when the applied force is largest, then begins to attenuate as the tongue is relieved of pressure. The degree of stratification is indicative of the extent of flexibility of the tongue i.e. the ability of different parts of the tongue to sustain different degrees of deformation and motion.

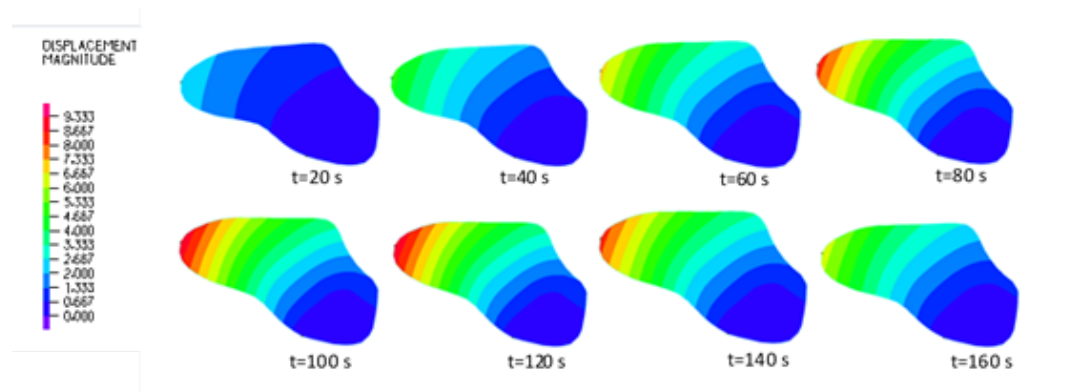


Figure 52: Predicted evolution of tongue deformation during propulsion stage of swallowing for normal tongue (Case 1)

Figures 53 and 54 show the distribution of deformations as predicted for Case 2 (early-stage cancer) and Case 3 (late-stage cancer), respectively. Cases 2 and 3 deformations are similar to those observed for normal tongue in (Figure 52). One exception to this involves observations that, starting at the tongue base, regions undergoing low magnitudes of deformation extend over a larger area than those observed within Case 1 (no cancer). The lowest deformations were observed within Case 3 (late-stage cancer). In addition, the magnitude with which these

deformations were stratified progressively decreases, relative to the normal tongue, between early and later stage representation. This observation illustrates progressive reductions in tongue flexibility and capacity for deformation in model with late-stage disease, relative to models with early-stage disease or no cancer at all.

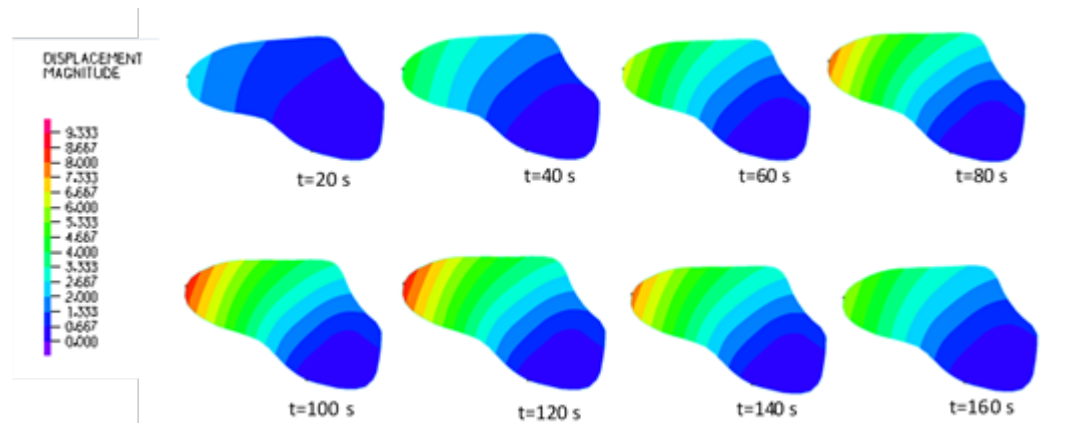


Figure 53: Predicted evolution of tongue deformation during propulsion stage of swallowing for tongue with mild cancer (Case 2)

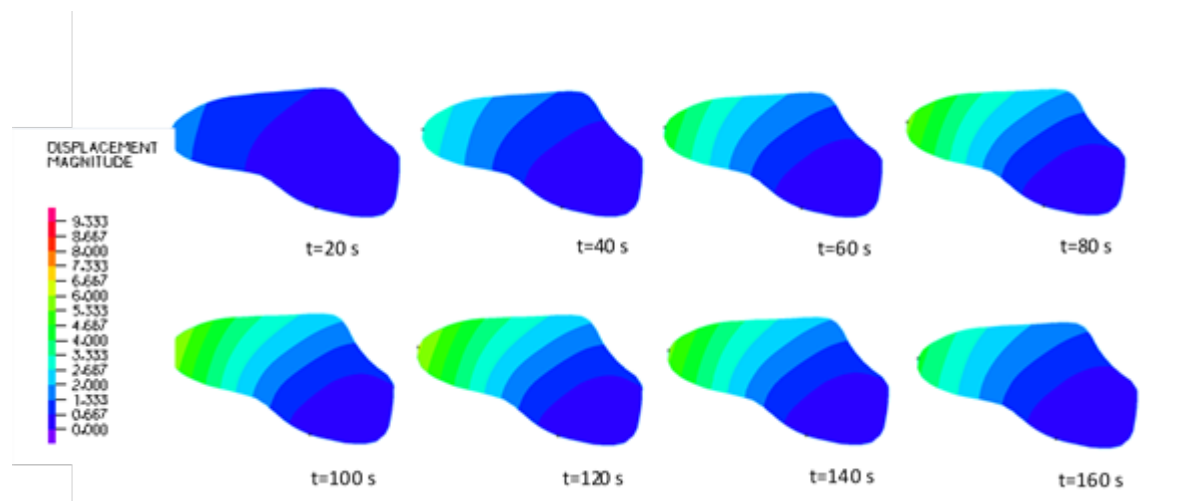


Figure 54: Predicted evolution of tongue deformation during propulsion stage of swallowing for tongue with severe cancer (Case 3)

Figure 55 compares the deformation at mid-point ($t=100$ ms) during the propulsion stage to the initial rest condition of the tongue for the three cases. Here, the light grey outline (in the background) represents the initial rest position of the tongue while the foreground of each figure represents the position at 100ms. In all cases larger deformations, representing upward displacement, were observed in the tongue tip compared to the tongue base. Among the three cases, the deformation was largest for the tongue without cancer (Case 1) and lowest for the tongue with late-stage cancer (Case 3), a finding consistent with those illustrated in Figures. 52, 53 and 54.

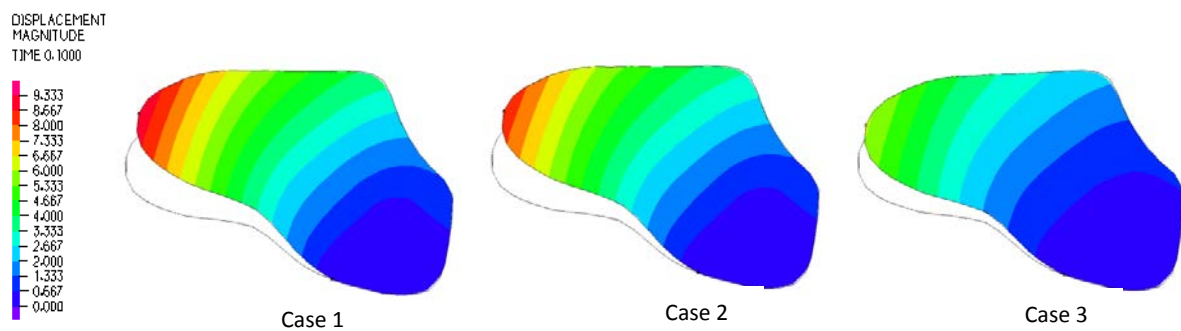


Figure 55: Predicted tongue deformation from initial rest state to intermediate state at $t = 100$ ms for normal tongue (Case 1), tongue with mild cancer (Case 2) and tongue with severe cancer (Case 3)

Three locations on the tongue were also selected and monitored to further quantify the effect of cancer on spatial deformation. These locations were selected to permit the effect of cancer of the tongue base to be readily assessed. These three locations are the tongue tip P1, top surface of the tongue P2 and the tongue base (P3) where cancer is visible as illustrated in Figure 56.

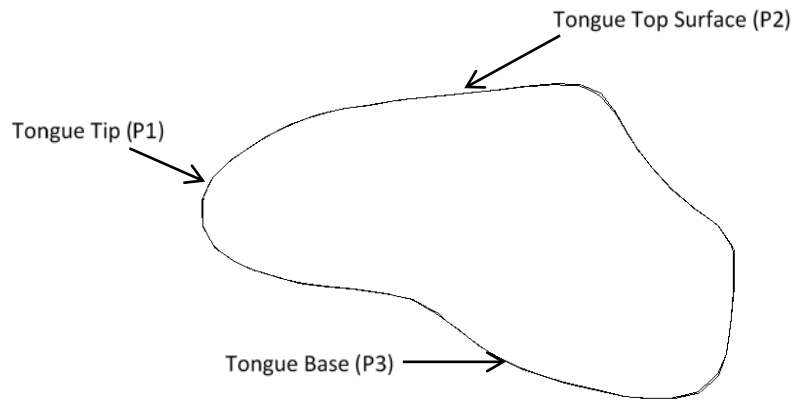


Figure 56: Three monitored locations on the tongue

Figure 57 shows the predicted tongue deformation at the three monitored locations for the three cases considered. It should be noted that the locations monitored for displacement are different from those used for loading. However, the displacement profile at each location generally mimics time sequence of the applied pressure, increasing to a maximum approximately midway through the propulsion stage ($t = 120$ ms), before decreasing to a resting state as the tongue is gradually relieved of the applied pressure. As expected, the deformation in all three cases is largest at the tip (P1) and smallest near the base (P3). The magnitude of the deformation decreases relative to increases in disease severity as well as distance between the monitored location and the modeled lesion, consistent with increasing tissue stiffness secondary to the presence of the lesion.

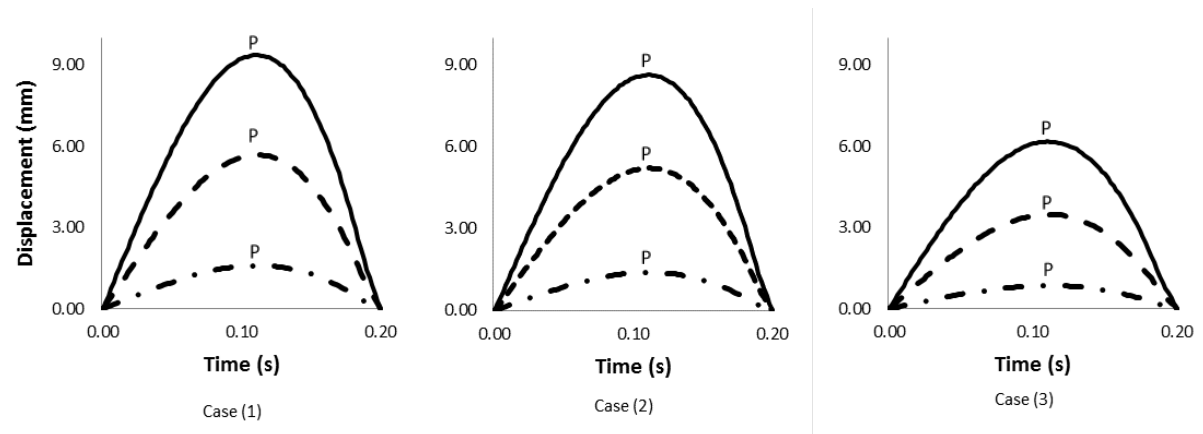


Figure 57: Displacement at three monitored locations for three cases: Case 1 (no cancer), Case 2 (early-stage cancer) and Case 3 (late-stage cancer)

The predicted maximum displacements at the three monitored locations are also presented in Table 18. The maximum deformation is observed at the tip of the tongue while the lowest is near the base. In addition, the magnitude of the deformation decreases with severity of the cancer in all cases. The results therefore predict that the tongue motion is abnormal in the presence of cancer and the extent of abnormality increases with increased severity of the cancer. These observed trends are in the consensus of the medical literature on dysphagia in patients with cancer of the tongue base [155].

Table 18: Predicted maximum displacement at three monitored locations on the tongue

	Displacement (mm)		
	Location P1	Location P2	Location P3
Case 1 (normal tongue)	9.38	5.70	1.60
Case 2 (tongue with early-stage cancer)	8.65	5.22	1.40
Case 3 (tongue with late-stage cancer)	6.17	3.48	0.85

7.4 Discussion

A biomechanical model has been developed and used to calculate the spatio-temporal deformation of the tongue during the oral (propulsion) stage of swallow. The model involves solution of the equations governing the stress-strain relation of the material of the tongue under applied load. The tongue is assumed to be a homogeneous muscular material with hyper-elastic property. The simulation involves several steps starting with the reconstruction of the three dimensional (3D) tongue geometry from MRI images of the upper airways acquired from real living human patients, discretization of the 3D geometry into finite elements and finally, integration of the governing equations over the finite elements in order to calculate the transient displacement of the tongue.

Three parametric cases were considered representing normal tongue with no tumor, tongue with early-stage cancer of the base, and tongue with late-stage cancer of the base. Localized cancer was represented by increasing the material stiffness at the affected region, with the stiffness level increasing with severity of the cancer. The transient deformation at landmark locations along and within the tongue were monitored and compared for the three cases. The simulation focused on the oral stage of swallow.

The major findings of the study can be summarized thus:

- a) Localized cancer reduces the deformation of the tongue and the extent of reduction depends on the severity of the cancer;
- b) Assuming the tongue is hyper-elastic adequately predicts the gross characteristics of tongue deformation during oral stage of swallow which are consistent with medical observation;

- c) The tongue deformation is spatially dependent with maximum at the tongue tip relative to the fixed base.

During swallowing, the tongue assists in controlling the bolus in the oral cavity and transport it to the pharynx in an efficient and timely manner [85, 156]. Previous studies have shown that the orderly sequence of tongue movements is necessary to have proper swallow[157]. This sequence begins with the tongue moving upward (propulsion stage), formation of palatal contact, and ending with return to a rest position. The findings in our study imply that the upward movement (propulsion stage) is diminished in the tongue stiffened by cancer. This will obviously impede the appropriate palatal contact of tongue dorsal to efficiently move the bolus through the oral cavity. In such a case, the bolus may not be held properly and also anterior leakages of liquid bolus may occur[158]. Thus the findings in this study are in the consensus of medical observations and are plausible in assessing the effect of tongue-base cancer on the swallowing process.

This study still relied on some assumptions which need to be relaxed in future studies. We assumed that the tongue muscle is hyper-elastic, but such a model may not completely describe the complex constitutive behavior of human tongue[132]. First, a sensitivity analysis of the data adopted to deduce material constants is desirable. The hyper-elastic model can be improved by using image registration to determine patient-specific elastic properties (specifically, the effective Young's modulus) of the tongue as has been successfully used to represent elastic property of lung[159, 160]. Specifically, such methods utilize an optical flow-based motion estimation, which is derived from 4DCT image data set. This approach enables estimation of the subject-specific deformation of the organ to be considered through

representation of the inter-nodal elastic interaction, and the surface elasticity in terms of the Young's modulus values.

Another stiff assumption is the loading applied to the tongue to initiate motion which has not considered the deformation of the tongue as the internal muscles contract in the fiber direction. Tongue deformation is primarily caused by intrinsic and extrinsic muscles. For example, the tongue is pulled upward by muscles located on the sides and the internal compression of the tongue tissue. However, delineation of these muscles is not readily achievable, since different muscle fibers often interweave with each other. The tongue movement was therefore induced in this study by applying normal stress to the elements on the top surface of the tongue in order to simulate the organ movement which was obtained using a sensor panel mounted on the hard palate. Using high resolution MRI images to delineate tongue tissues may permit imposition of more accurate loading conditions.

The boundary conditions defined in this study are not applied in a 3D representation of the oral cavity. The current structure of the model includes a "no-displacement constraint" applied on the nodes located at the tongue root near the hyoid bone. Boundary conditions such as contact between the tongue dorsal and the hard palate, connection of extrinsic muscles to surrounding bone structure, and fixation near mandible are required in more rigorous representations of tongue biomechanical model and desirable in subsequent work. The propulsion stage of oral swallow in the swallow model could be extended in subsequent studies to the oral preparatory stage of tongue and the pharyngeal stage as well.

The study has so far considered only the effect of cancer-induced hardening on swallowing. Cancer has been considered to be localized within the tongue base in this study. This approach can be extended to study the type, location and size of the tongue cancer. Additional data such

as MRI images may be needed to outline the tumor size and exact location. The tongue model developed can then be used as a tool to study the effect of disease on the swallowing process, and aid treatment planning for patients with cancer of the tongue base and swallowing dysfunction.

CHAPTER 8: CONCLUSIONS AND FUTURE WORK

8.1 Summary of Chapters

Summary of Chapters

The conclusions from the research are readily summarized from the findings in the relevant chapters of this dissertation as presented below.

Chapter 3, The key contribution of this chapter is the use of airway modeling to study aspiration in patients with impaired cough function including those with upper airway and neurological diseases. The study can be used to improve the understanding of cough flow dynamics within the airway and inform strategies for treatment with ‘cough assist devices’ or devices to improve cough strength. The proposed biomechanical model is the first of its kind to study cough-penetrant dynamics within the tracheal airway. As such it presents a “proof-of-concept” biomechanical modeling of human cough.

Chapter 4, This chapter presents cough flow modeling with improvement to the anatomy and physiology including oro-pharyngeal reconstruction beyond the laryngeal airway and allowance for deformable airway wall beyond the model developed in the previous chapter. The expiratory phase is the strongest phase of cough and results in very high observed airway velocities and pressures. At peak-expiratory flow instance, the velocity was predicted to be 130 m/s for the specific cases and conditions considered. The narrowest part of the airway had the highest velocities throughout the cough event. The results of parametric studies suggest that the variables of interest including penetrant density and size are primarily governed by the drag force.

Chapter 5, This chapter captures the effect of variation of liquid droplet characteristics in the upper airway under cough. The results suggest that the cough biomechanical model is better

able to represent droplet behavior and promote the airway clearance in the presence of droplets towards realistic cough mechanism. The analysis of the droplet trajectory indicated that a strong cough caused more droplet breakup events. The aerodynamic forces exerted on the droplets caused secondary breakups. In a strong cough event, the relative velocity between the droplet and airflow was quite high, which thus increased the aerodynamic forces acting on the droplet. The findings imply that more breakup events and smaller child droplet size aid the removal of penetrants from the airway. These findings shed light on an issue relevant to cough evaluation and management. The role of droplet collision, coalescence and re-formation may be a risk marker, and the impact of scattering for microaspiration events may need to be further explored.

Chapter 6, A two-dimensional (2D) finite element model of upper airway function relevant to Obstructive Sleep Apnea (OSA) was developed emphasizing the effects of dilator muscular activation on the human retro-lingual airway. Three cases were investigated: subject in standing position; supine position; and supine position coupled with dilator muscle activation. The biomechanical model can reproduce physiologic findings in humans concerning the effects of position on pharyngeal patency and neuromuscular activation. The predicted results suggests a decrease in the pharyngeal luminal opening from the standing position to the supine position, which results in a reduction in the pressure in the laryngopharynx. In addition, there occurs an increase in the resistance to the airflow which correlates with the relevant anatomical changes and outcomes relevant to patients with obstructive sleep apnea. In the supine position, the narrowing of the airway results in higher pressure differential between the internal pressure and the external pressure imposed by the weight of the surrounding tissues, which makes the upper airway behave like a collapsible vessel. The value of this model in going forward is to encourage the development of more sophisticated models that include more degrees of

freedom, the possibility of multi-site collapse and effects of specific muscles alone or in combination on upper airway size and shape, compliance, and stability to the point where predictions can be made.

Chapter 7, A biomechanical model was developed and used to calculate the spatio-temporal deformation of the tongue during the oral (propulsion) stage of swallow. The model involves solution of the equations governing the stress-strain relation of the material of the tongue under applied load. Three parametric cases were considered representing normal tongue with no tumor, tongue with early-stage cancer of the base, and tongue with late-stage cancer of the base. Localized cancer was represented by increasing the material stiffness at the affected region, with the stiffness level increasing with severity of the cancer. The predicted result suggest that the localized cancer reduces the deformation of the tongue and the extent of reduction depends on the severity of the cancer. This model can be extended to study the type, location and size of the tongue cancer. The tongue model developed can then be used as a tool to study the effect of disease on the swallowing process, and aid treatment planning for patients with cancer of the tongue base and swallowing dysfunction.

8.2 Challenges and Future Direction

The following summarizes recommendations for future work.

8.2.1 *Improvements to Cough CFD Model*

Integration of Theory/Modeling and Experiment:

The experimental program of study should be designed to provide data for validation of the cough model. The experimental data will include mean and transient airflow velocities, pressure, and turbulence characteristics. The key role of theory is to use the experimental

conditions to predict some of the dynamical characteristics of the flow and relate the latter to the measured properties. The feedback from experiment to modeling will result in a reliable classification of explosive cough flow in human airways, in particular, and laminar-turbulent transition in unsteady flow in general.

Specific Experiments to be performed:

1. Determine cough wave speed/Mach number using high-speed shadowgraph
2. Measure instantaneous fluid velocity using hot wire anemometer
3. Measure turbulent velocity field using Laser Doppler Velocimetry

Key physical parameters to be predicted from the experimental study

- Spatio-temporal velocity distribution
- Instantaneous velocity at several locations (Hot-Wire Anemometry)
- Pressure at several locations (Pressure Transducers)
- Cough wave propagation speed

8.2.2 Improvements to Obstructive Sleep Apnea Model

Extensive validation to the modeling results should be planned using abundantly available and published data relevant to OSA, with and without gravity. Facial morphology influences OSA and surgical success for OSA is accomplished with maxillomandibular advancement. Previous sleep apnea simulation data demonstrate the pre and post fluid dynamic changes achievable when modelling anatomical surgical alterations of the upper airway. Numerous data sets can be therefore used to validate varying effects of morphological deviations or manipulations on airflow dynamics in OSA obtained from our model.

Experimental validation of OSA model:

An experimental simulator can be developed and used to test the pressure and airflow distributions associated with the 3D geometrically-correct reconstruction of the upper airway sections involved in OSA. The simulator will be applied as a function of:

- Nasal dimensions change
- Pharyngeal dimensions change
- Mandibular advancement change
- Negative and positive oral pressure change as a function lung volume

8.2.3 Improvements to Swallow Model

Integration of heterogeneous elasticity from high speed 4D MRI image datasets:

The biomechanical modeling of the tongue requires identifying its complex myoarchitecture which consists of different muscle groups required to alter its shape and move the tongue in various directions. The constitutive behavior of the tongue tissues which exhibit anisotropic inhomogeneous viscoelastic properties has been a challenge in subject-specific tongue models as simulation results of such models depend on accurate representation of elastic properties within tongue anatomy including intrinsic and extrinsic muscles. Recent advances in the field of 4D imaging and high-performance computing facilitated by state-of-the-art graphics processing have led to quantification of real time tongue motion. This method can be used to obtain spatially varying heterogeneous elastic properties for tongue structures. The spatial variation of the elastic properties will also ensure that non-homogeneity is preserved in different muscle regions of the tongue. The integration of image-based elastic values can uniquely addresses the inaccuracies caused by assuming simplistic elastic properties in Finite Element models.

APPENDIX: AUTHOR'S BIOGRAPHY

Nadun Sachinthaka Kuruppumullage graduated from University of Moratuwa, Sri Lanka with a Bachelor of the Science (B.Sc.) degree in Mechanical Engineering in 2010. He moved to Orlando, Florida, USA to continue her education in Mechanical Engineering at the University of Central Florida. He earned a Master of Science (M.S.C.E.) and a Doctor of Philosophy (Ph.D.) degree in Mechanical Engineering with focus on Thermo-fluid in 2018.

REFERENCES

1. Person, A. and M.L. Mintz, *Anatomy and physiology of the respiratory tract*, in *Disorders of the Respiratory Tract*. 2006, Springer. p. 11-15.
2. McKinley, M.P., et al., *Human anatomy*. 2006: McGraw-Hill Higher Education Boston, MA.
3. Knowles, M.R. and R.C. Boucher, *Mucus clearance as a primary innate defense mechanism for mammalian airways*. The Journal of clinical investigation, 2002. **109**(5): p. 571-577.
4. Donner, M.W., J.F. Bosnia, and D.L. Robertson, *Anatomy and physiology of the pharynx*. Gastrointestinal radiology, 1985. **10**(1): p. 197-212.
5. Isono, S., et al., *Anatomy of pharynx in patients with obstructive sleep apnea and in normal subjects*. Journal of Applied Physiology, 1997. **82**(4): p. 1319-1326.
6. Negus, V.E., *The comparative anatomy and physiology of the larynx*. 1949: Hafner Pub. Company; New York.
7. Gray, H., *Anatomy of the human body*. Vol. 8. 1878: Lea & Febiger.
8. Chan, Y.K., *Physiology of the Airway*, in *Airway Management*. 2014, Springer. p. 1-14.
9. Malvè, M., et al., *FSI analysis of the coughing mechanism in a human trachea*. Annals of biomedical engineering, 2010. **38**(4): p. 1556-1565.
10. Widdicombe, J., et al., *Voluntary and reflex cough and the expiration reflex; implications for aspiration after stroke*. Pulmonary pharmacology & therapeutics, 2011. **24**(3): p. 312-317.
11. Boitano, L.J., *Management of airway clearance in neuromuscular disease*. Respiratory Care, 2006. **51**(8): p. 913-924.

12. Nguyen, N.P., et al., *Effectiveness of the cough reflex in patients with aspiration following radiation for head and neck cancer*. Lung, 2007. **185**(5): p. 243-248.
13. Lawson, T. and R. Harris, *Assessment of the mechanical efficiency of coughing in healthy young adults*. Clinical science, 1967. **33**(1): p. 209-224.
14. Pitts, T., et al., *Impact of expiratory muscle strength training on voluntary cough and swallow function in Parkinson disease*. Chest, 2009. **135**(5): p. 1301-1308.
15. Ross, B., R. Gramiak, and H. Rahn, *Physical dynamics of the cough mechanism*. Journal of Applied Physiology, 1955. **8**(3): p. 264-268.
16. Sant'Ambrogio, G., et al., *Activation of intrinsic laryngeal muscles during cough*. American journal of respiratory and critical care medicine, 1997. **155**(2): p. 637-641.
17. Yanagihara, N., H. Von Leden, and E. Werner-Kukuk, *The physical parameters of cough: the larynx in a normal single cough*. Acta oto-laryngologica, 1966. **61**(1-6): p. 495-510.
18. Hoffman Ruddy, B., et al., *Computational Modelling of Cough Function and Airway Penetrant Behavior in Patients with Disorders of Laryngeal Function*. Laryngoscope investigative otolaryngology, 2017. **2**(1): p. 23-29.
19. Leith, D.E., et al., *Cough*. Comprehensive Physiology, 1986.
20. Fontana, G.A., *Motor mechanisms and the mechanics of cough*. Cough: Causes, mechanisms and therapy, 2003: p. 193-205.
21. Hegland, K.W., M.S. Okun, and M.S. Troche, *Sequential voluntary cough and aspiration or aspiration risk in Parkinson's disease*. Lung, 2014. **192**(4): p. 601-608.
22. Myslinski, M. and C. Scanlan, *Wilkins RL, Sytoller JK. Bronchial hygiene therapy*. Egan's Fundamentals of Respiratory Care Mosby, St. Louis, 2003: p. 883-910.
23. Egan, D.F., *Fundamentals of respiratory therapy*. 1977: CV Mosby.

24. Kim, J., P. Davenport, and C. Sapienza, *Effect of expiratory muscle strength training on elderly cough function*. Archives of gerontology and geriatrics, 2009. **48**(3): p. 361-366.
25. Addington, W.R., R.E. Stephens, and K.A. Gilliland, *Assessing the laryngeal cough reflex and the risk of developing pneumonia after stroke: an interhospital comparison*. Stroke, 1999. **30**(6): p. 1203-1207.
26. Knudson, R.J., J. Mead, and D.E. Knudson, *Contribution of airway collapse to supramaximal expiratory flows*. Journal of Applied Physiology, 1974. **36**(6): p. 653-667.
27. Woodson, B.T., *Expiratory pharyngeal airway obstruction during sleep: a multiple element model*. The Laryngoscope, 2003. **113**(9): p. 1450-1459.
28. Cebral, J.R. and R.M. Summers, *Tracheal and central bronchial aerodynamics using virtual bronchoscopy and computational fluid dynamics*. IEEE transactions on medical imaging, 2004. **23**(8): p. 1021-1033.
29. Kim, C.S. and A.J. IGLESIAS, *Deposition of inhaled particles in bifurcating airway models: I. Inspiratory deposition*. Journal of Aerosol Medicine, 1989. **2**(1): p. 1-14.
30. KIM, C.S., A.J. IGLESIAS, and L. GARCIA, *Deposition of inhaled particles in bifurcating airway models: II. Expiratory deposition*. Journal of Aerosol Medicine, 1989. **2**(1): p. 15-27.
31. Luo, X., et al., *LES modelling of flow in a simple airway model*. Medical Engineering and Physics, 2004. **26**(5): p. 403-413.
32. Xu, C., et al., *Computational fluid dynamics modeling of the upper airway of children with obstructive sleep apnea syndrome in steady flow*. Journal of biomechanics, 2006. **39**(11): p. 2043-2054.

33. Sung, S.-J., et al., *Customized three-dimensional computational fluid dynamics simulation of the upper airway of obstructive sleep apnea*. The Angle Orthodontist, 2006. **76**(5): p. 791-799.
34. Luo, H. and Y. Liu, *Modeling the bifurcating flow in a CT-scanned human lung airway*. Journal of Biomechanics, 2008. **41**(12): p. 2681-2688.
35. Ma, B. and K.R. Lutchen, *An anatomically based hybrid computational model of the human lung and its application to low frequency oscillatory mechanics*. Annals of biomedical engineering, 2006. **34**(11): p. 1691-1704.
36. Li, Z., C. Kleinstreuer, and Z. Zhang, *Simulation of airflow fields and microparticle deposition in realistic human lung airway models. Part I: Airflow patterns*. European Journal of Mechanics-B/Fluids, 2007. **26**(5): p. 632-649.
37. Zhao, K., et al., *Numerical modeling of turbulent and laminar airflow and odorant transport during sniffing in the human and rat nose*. Chemical senses, 2005. **31**(2): p. 107-118.
38. Taherian, S., H. Rahai, and T. Waddington. *CFD modeling and analysis of pulmonary airways/particles transport and deposition*. in *41st AIAA Fluid Dynamics Conference and Exhibit*. 2011.
39. Kleinstreuer, C. and Z. Zhang, *Laminar-to-turbulent fluid-particle flows in a human airway model*. International Journal of Multiphase Flow, 2003. **29**(2): p. 271-289.
40. Mylavarapu, G., et al., *Validation of computational fluid dynamics methodology used for human upper airway flow simulations*. Journal of biomechanics, 2009. **42**(10): p. 1553-1559.

41. Stapleton, K.-W., et al., *On the suitability of $k-\epsilon$ turbulence modeling for aerosol deposition in the mouth and throat: a comparison with experiment*. Journal of Aerosol Science, 2000. **31**(6): p. 739-749.
42. Lin, C.-L., et al., *Characteristics of the turbulent laryngeal jet and its effect on airflow in the human intra-thoracic airways*. Respiratory physiology & neurobiology, 2007. **157**(2-3): p. 295-309.
43. Pope, S.B., *Turbulent flows*. 2001, IOP Publishing.
44. Zhang, Z., et al., *Comparison of micro-and nano-size particle depositions in a human upper airway model*. Journal of aerosol science, 2005. **36**(2): p. 211-233.
45. Troche, M.S., et al., *Respiratory-swallowing coordination and swallowing safety in patients with Parkinson's disease*. Dysphagia, 2011. **26**(3): p. 218-224.
46. Caruso, A.J., M.T. McClowry, and L. Max. *Age-related effects on speech fluency*. in *Seminars in speech and language*. 1997. © 1997 by Thieme Medical Publishers, Inc.
47. Warms, T. and J. Richards, *Wet voice as a predictor of penetration and aspiration in oropharyngeal dysphagia*. Dysphagia, 2000. **15**(2): p. 84-88.
48. Kelly, A.M., M.J. Drinnan, and P. Leslie, *Assessing penetration and aspiration: how do videofluoroscopy and fiberoptic endoscopic evaluation of swallowing compare?* The Laryngoscope, 2007. **117**(10): p. 1723-1727.
49. Addington, W.R., et al., *Assessing the laryngeal cough reflex and the risk of developing pneumonia after stroke*. Archives of physical medicine and rehabilitation, 1999. **80**(2): p. 150-154.
50. Smith, D., S. Hamlet, and L. Jones, *Acoustic technique for determining timing of velopharyngeal closure in swallowing*. Dysphagia, 1990. **5**(3): p. 142-146.

51. Sellars, C., C. Dunnet, and R. Carter, *A preliminary comparison of videofluoroscopy of swallow and pulse oximetry in the identification of aspiration in dysphagic patients.* Dysphagia, 1998. **13**(2): p. 82-86.
52. Wang, T.-G., et al., *Pulse oximetry does not reliably detect aspiration on videofluoroscopic swallowing study.* Archives of physical medicine and rehabilitation, 2005. **86**(4): p. 730-734.
53. Rosenbek, J.C., et al., *A penetration-aspiration scale.* Dysphagia, 1996. **11**(2): p. 93-98.
54. Robbins, J., et al., *Differentiation of normal and abnormal airway protection during swallowing using the penetration–aspiration scale.* Dysphagia, 1999. **14**(4): p. 228-232.
55. Troche, M., et al., *Aspiration and swallowing in parkinson disease and rehabilitation with EMST A randomized trial.* Neurology, 2010. **75**(21): p. 1912-1919.
56. Logemann, J.A., et al., *A randomized study of three interventions for aspiration of thin liquids in patients with dementia or Parkinson's disease.* Journal of Speech, Language, and Hearing Research, 2008. **51**(1): p. 173-183.
57. Ono, T., *Tongue and upper airway function in subjects with and without obstructive sleep apnea.* Japanese Dental Science Review, 2012. **48**(2): p. 71-80.
58. Kuna, S.T. and J.E. Remmers, *Neural and anatomic factors related to upper airway occlusion during sleep.* Medical Clinics of North America, 1985. **69**(6): p. 1221-1242.
59. Jordan, A.S., et al., *Mechanisms used to restore ventilation after partial upper airway collapse during sleep in humans.* Thorax, 2007.
60. Remmers, J., et al., *Pathogenesis of upper airway occlusion during sleep.* Journal of Applied Physiology, 1978. **44**(6): p. 931-938.

61. Worsnop, C., et al., *Activity of respiratory pump and upper airway muscles during sleep onset*. Journal of applied physiology, 1998. **85**(3): p. 908-920.
62. Mezzanotte, W.S., D.J. Tangel, and D.P. White, *Influence of sleep onset on upper-airway muscle activity in apnea patients versus normal controls*. American journal of respiratory and critical care medicine, 1996. **153**(6): p. 1880-1887.
63. Strohl, K.P., J.P. Butler, and A. Malhotra, *Mechanical properties of the upper airway*. Comprehensive Physiology, 2012.
64. Fogel, R., A. Malhotra, and D. White, *Sleep· 2: pathophysiology of obstructive sleep apnoea/hypopnoea syndrome*. Thorax, 2004. **59**(2): p. 159-163.
65. Strollo Jr, P.J., et al., *Upper-airway stimulation for obstructive sleep apnea*. New England Journal of Medicine, 2014. **370**(2): p. 139-149.
66. Bolser, D.C., T.E. Pitts, and K.F. Morris, *The use of multiscale systems biology approaches to facilitate understanding of complex control systems for airway protection*. Current opinion in pharmacology, 2011. **11**(3): p. 272-277.
67. Aittokallio, T., M. Gyllenberg, and O. Polo, *A model of a snorer's upper airway*. Mathematical biosciences, 2001. **170**(1): p. 79-90.
68. Banabilh, S.M., et al., *Assessment of 3-D nasal airway morphology in Southeast Asian adults with obstructive sleep apnea using acoustic rhinometry*. Clinical oral investigations, 2010. **14**(5): p. 491-498.
69. Banabilh, S., et al., *Dental arch morphology in south-east Asian adults with obstructive sleep apnoea: geometric morphometrics*. Journal of oral rehabilitation, 2009. **36**(3): p. 184-192.

70. Ito, Y., et al., *Patient-specific geometry modeling and mesh generation for simulating obstructive sleep apnea syndrome cases by maxillomandibular advancement*. Mathematics and computers in simulation, 2011. **81**(9): p. 1876-1891.
71. Subramaniam, D.R., et al., *Upper airway elasticity estimation in pediatric Down syndrome sleep apnea patients using collapsible tube theory*. Annals of biomedical engineering, 2016. **44**(5): p. 1538-1552.
72. Brown, E.C., et al., *Tongue stiffness is lower in patients with obstructive sleep apnea during wakefulness compared with matched control subjects*. Sleep, 2015. **38**(4): p. 537-544.
73. Toubiana, E., et al., *Large Eddy simulation and Reynolds-averaged Navier–Stokes modeling of flow in staggered plate arrays: Comparison at various flow regimes*. Applied Thermal Engineering, 2015. **89**: p. 405-420.
74. Zhao, M., et al., *Computational fluid dynamics for the assessment of upper airway response to oral appliance treatment in obstructive sleep apnea*. Journal of biomechanics, 2013. **46**(1): p. 142-150.
75. Wang, Y., et al., *Fluid–structure interaction modeling of upper airways before and after nasal surgery for obstructive sleep apnea*. International journal for numerical methods in biomedical engineering, 2012. **28**(5): p. 528-546.
76. Gillis, E., et al., *A novel implantable device for a minimally invasive surgical treatment of obstructive sleep apnea: design and preclinical safety assessment*. Nature and science of sleep, 2016. **8**: p. 249.
77. Pelteret, J.P.V. and B.D. Reddy, *Development of a computational biomechanical model of the human upper-airway soft-tissues toward simulating obstructive sleep apnea*. Clinical Anatomy, 2014. **27**(2): p. 182-200.

78. Logemann, J.A. and D.E. Bytell, *Swallowing disorders in three types of head and neck surgical patients*. Cancer, 1979. **44**(3): p. 1095-1105.
79. Lazarus, C.L., et al., *Swallowing disorders in head and neck cancer patients treated with radiotherapy and adjuvant chemotherapy*. The Laryngoscope, 1996. **106**(9): p. 1157-1166.
80. Logemann, J.A., et al., *Swallowing disorders in the first year after radiation and chemoradiation*. Head & neck, 2008. **30**(2): p. 148-158.
81. Logemann, J.A., et al., *Site of disease and treatment protocol as correlates of swallowing function in patients with head and neck cancer treated with chemoradiation*. Head & neck, 2006. **28**(1): p. 64-73.
82. Kendall, K.A., et al., *Structural mobility in deglutition after single modality treatment of head and neck carcinomas with radiotherapy*. Head & neck, 1998. **20**(8): p. 720-725.
83. Logemann, J.A., *The evaluation and treatment of swallowing disorders*. Current Opinion in Otolaryngology & Head and Neck Surgery, 1998. **6**(6): p. 395-400.
84. Gérard, J.-M., et al., *Non-linear elastic properties of the lingual and facial tissues assessed by indentation technique: application to the biomechanics of speech production*. Medical Engineering and Physics, 2005. **27**(10): p. 884-892.
85. Logemann, J.A. and J.A. Logemann, *Evaluation and treatment of swallowing disorders*. 1983.
86. Buchaillard, S., P. Perrier, and Y. Payan, *A biomechanical model of cardinal vowel production: muscle activations and the impact of gravity on tongue positioning*. The Journal of the Acoustical Society of America, 2009. **126**(4): p. 2033-2051.

87. Stavness, I., J.E. Lloyd, and S. Fels, *Automatic prediction of tongue muscle activations using a finite element model*. Journal of biomechanics, 2012. **45**(16): p. 2841-2848.
88. Yang, Y., et al., *Physics-based deformable tongue visualization*. IEEE transactions on visualization and computer graphics, 2013. **19**(5): p. 811-823.
89. McKeown, M.J., D.C. Torpey, and W.C. Gehm, *Non-invasive monitoring of functionally distinct muscle activations during swallowing*. Clinical Neurophysiology, 2002. **113**(3): p. 354-366.
90. Materialise, *Mimics 14.01*. 2010: Belgium.
91. Materialise, B. *3-matic 5.1*. 2010; Available from: <http://biomedical.materialise.com/3-matic>.
92. *Star CCM+*. 2015, Siemens PLM.
93. Menter, F.R., *Two-equation eddy-viscosity turbulence models for engineering applications*. AIAA journal, 1994. **32**(8): p. 1598-1605.
94. Wilcox, D.A., *Simulation of transition with a two-equation turbulence model*. AIAA journal, 1994. **32**(2): p. 247-255.
95. Dewan, A., *Tackling turbulent flows in engineering*. 2010: Springer Science & Business Media.
96. Subramaniam, S., *Lagrangian–Eulerian methods for multiphase flows*. Progress in Energy and Combustion Science, 2013. **39**(2-3): p. 215-245.
97. Bai, C. and A. Gosman, *Development of methodology for spray impingement simulation*. 1995, SAE Technical Paper.
98. Liu, A.B., D. Mather, and R.D. Reitz, *Modeling the effects of drop drag and breakup on fuel sprays*. 1993, WISCONSIN UNIV-MADISON ENGINE RESEARCH CENTER.

99. Martin-Harris, B., *Coordination of respiration and swallowing*. GI Motility online, 2006.
100. Fuller, R. and D. Jackson, *Physiology and treatment of cough*. Thorax, 1990. **45**(6): p. 425.
101. Sant'Ambrogio, G., *Role of the larynx in cough*. Pulmonary pharmacology, 1996. **9**(5-6): p. 379-382.
102. Lai, S.K., Y.-Y. Wang, and J. Hanes, *Mucus-penetrating nanoparticles for drug and gene delivery to mucosal tissues*. Advanced drug delivery reviews, 2009. **61**(2): p. 158-171.
103. Pitts, T., et al., *Voluntary cough production and swallow dysfunction in Parkinson's disease*. Dysphagia, 2008. **23**(3): p. 297-301.
104. Kulnik, S.T., et al., *Higher cough flow is associated with lower risk of pneumonia in acute stroke*. Thorax, 2016. **71**(5): p. 474-475.
105. Hammond, C.S., et al., *Assessment of aspiration risk in stroke patients with quantification of voluntary cough*. Neurology, 2001. **56**(4): p. 502-506.
106. Kendrick, A.H., *Airways Clearance Techniques in Cystic Fibrosis: Physiology, Devices and the Future*, in *Cystic Fibrosis-Renewed Hopes Through Research*. 2012, InTech.
107. Zayas, G., et al., *Cough aerosol in healthy participants: fundamental knowledge to optimize droplet-spread infectious respiratory disease management*. BMC pulmonary medicine, 2012. **12**(1): p. 11.
108. Mihaescu, M., et al., *Large eddy simulation of the pharyngeal airflow associated with obstructive sleep apnea syndrome at pre and post-surgical treatment*. Journal of biomechanics, 2011. **44**(12): p. 2221-2228.

109. Kleinstreuer, C., *Biofluid dynamics: Principles and selected applications*. 2006: CRC Press.
110. Sommerfeld, M., *Theoretical and experimental modelling of particulate flows*. Lecture series, 2000. **6**: p. 3-7.
111. Paz, C., E. Suárez, and J. Vence, *CFD transient simulation of the cough clearance process using an Eulerian wall film model*. Computer methods in biomechanics and biomedical engineering, 2017. **20**(2): p. 142-152.
112. Crowe, C.T., et al., *Multiphase flows with droplets and particles*. 2011: CRC press.
113. Bennett, W.D. and K.L. Zeman, *Effect of enhanced supramaximal flows on cough clearance*. Journal of Applied Physiology, 1994. **77**(4): p. 1577-1583.
114. Irwin, R.S., et al., *Managing cough as a defense mechanism and as a symptom: a consensus panel report of the American College of Chest Physicians*. CHEST Journal, 1998. **114**(2_Supplement): p. 133S-181S.
115. Star-CCM+. 2017; Star-CCM+]. Available from: <https://mdx.plm.automation.siemens.com/star-ccm-plus>.
116. Laine, P. and H.S. Siirilä, *Oral and manual stereognosis and two-point tactile discrimination of the tongue*. Acta Odontologica Scandinavica, 1971. **29**(2): p. 197-204.
117. Hoebler, M.-F.D., A. Karinhi, C. Belleville, J.-L. Barry, C, *Particle size of solid food after human mastication and in vitro simulation of oral breakdown*. International journal of food sciences and nutrition, 2000. **51**(5): p. 353-366.
118. Wierzbza, A., *Deformation and breakup of liquid drops in a gas stream at nearly critical Weber numbers*. Experiments in Fluids, 1990. **9**(1-2): p. 59-64.

119. Nomura, K., et al., *Numerical analysis of droplet breakup behavior using particle method*. Journal of Nuclear Science and technology, 2001. **38**(12): p. 1057-1064.
120. Reitz, R.D. and R. Diwakar, *Effect of drop breakup on fuel sprays*. 1986, SAE Technical Paper.
121. Reitz, R.D. and R. Diwakar, *Structure of high-pressure fuel sprays*. 1987, SAE Technical Paper.
122. Huang, Y., D.P. White, and A. Malhotra, *Use of computational modeling to predict responses to upper airway surgery in obstructive sleep apnea*. The Laryngoscope, 2007. **117**(4): p. 648-653.
123. Huang, Y., D.P. White, and A. Malhotra, *The impact of anatomic manipulations on pharyngeal collapse: results from a computational model of the normal human upper airway*. Chest Journal, 2005. **128**(3): p. 1324-1330.
124. Jeong, S.J., W.S. Kim, and S.J. Sung, *Numerical investigation on the flow characteristics and aerodynamic force of the upper airway of patient with obstructive sleep apnea using computational fluid dynamics*. Med Eng Phys, 2007. **29**(6): p. 637-51.
125. Zhang, Z. and C. Kleinstreuer, *Low-Reynolds-number turbulent flows in locally constricted conduits: a comparison study*. AIAA journal, 2003. **41**(5): p. 831-840.
126. Jayaraju, S.T., et al., *Effects of tracheal stenosis on flow dynamics in upper human airways*. 2006.
127. Pirnar, J., et al., *Computational fluid-structure interaction simulation of airflow in the human upper airway*. Journal of biomechanics, 2015. **48**(13): p. 3685-3691.
128. De Backer, J.W., et al., *Validation of computational fluid dynamics in CT-based airway models with SPECT/CT*. Radiology, 2010. **257**(3): p. 854-862.

129. Birch, M. and P. Srodon, *Biomechanical properties of the human soft palate*. The Cleft Palate-Craniofacial Journal, 2009. **46**(3): p. 268-274.
130. Ilegbusi, O.J., et al., *Mathematical modelling of tongue deformation during swallow in patients with head and neck cancer*. Mathematical and Computer Modelling of Dynamical Systems, 2016. **22**(6): p. 569-583.
131. Gérard, J.-M., et al., *Non-linear elastic properties of the lingual and facial tissues assessed by indentation technique: application to the biomechanics of speech production*. Medical engineering & physics, 2005. **27**(10): p. 884-892.
132. Cheng, S., et al., *Viscoelastic properties of the tongue and soft palate using MR elastography*. Journal of biomechanics, 2011. **44**(3): p. 450-454.
133. Lakatos, É., L. Magyar, and I. Bojtár, *Material properties of the mandibular trabecular bone*. Journal of medical engineering, 2014. **2014**.
134. Eisele, D.W., et al., *Direct hypoglossal nerve stimulation in obstructive sleep apnea*. Archives of Otolaryngology–Head & Neck Surgery, 1997. **123**(1): p. 57-61.
135. Yoo, P.B. and D.M. Durand, *Effects of selective hypoglossal nerve stimulation on canine upper airway mechanics*. Journal of Applied Physiology, 2005. **99**(3): p. 937-943.
136. Issa, F.G. and C.E. Sullivan, *Upper airway closing pressures in obstructive sleep apnea*. Journal of Applied Physiology, 1984. **57**(2): p. 520-527.
137. USA, A.R.D.I., *ADINA 9.01*. 2014.
138. Adina, R., *ADINA theory and modeling guide*. 1986: ADINA R & D.
139. Van de Graaff, W.B., et al., *Respiratory function of hyoid muscles and hyoid arch*. Journal of Applied Physiology, 1984. **57**(1): p. 197-204.

140. Fouke, J.M. and K.P. Strohl, *Effect of position and lung volume on upper airway geometry*. Journal of Applied Physiology, 1987. **63**(1): p. 375-380.
141. Pae, E.K., et al., *A cephalometric and electromyographic study of upper airway structures in the upright and supine positions*. Am J Orthod Dentofacial Orthop, 1994. **106**(1): p. 52-9.
142. Amatoury, J., et al., *Development and validation of a computational finite element model of the rabbit upper airway: simulations of mandibular advancement and tracheal displacement*. Journal of Applied Physiology, 2016. **120**(7): p. 743-757.
143. Cheng, G.C., et al., *Assessment of Surgical Effects on Patients with Obstructive Sleep Apnea Syndrome Using Computational Fluid Dynamics Simulations*. Math Comput Simul, 2014. **106**: p. 44-59.
144. Safiruddin, F., et al., *Effect of upper-airway stimulation for obstructive sleep apnoea on airway dimensions*. Eur Respir J, 2015. **45**(1): p. 129-38.
145. Strollo, P.J. and R.M. Rogers, *Obstructive sleep apnea*. New England Journal of Medicine, 1996. **334**(2): p. 99-104.
146. Bathe, K.J., *Finite Element Procedures*. 2006: ADINA Publications, Watertown, MA.
147. Napadow, V.J., et al., *Intramural mechanics of the human tongue in association with physiological deformations*. Journal of biomechanics, 1999. **32**(1): p. 1-12.
148. Gérard, J.-M., et al., *A 3D dynamical biomechanical tongue model to study speech motor control*. arXiv preprint physics/0606148, 2006.
149. Ophir, J., et al., *Elastography: imaging the elastic properties of soft tissues with ultrasound*. Journal of medical ultrasonics, 2002. **29**(4): p. 155.
150. Krouskop, T.A., et al., *Elastic moduli of breast and prostate tissues under compression*. Ultrasonic imaging, 1998. **20**(4): p. 260-274.

151. Wellman, P., et al., *Breast tissue stiffness in compression is correlated to histological diagnosis*. Harvard BioRobotics Laboratory Technical Report, 1999: p. 1-15.
152. Furuya, J., et al., *Tongue pressure production while swallowing water and pudding and during dry swallow using a sensor sheet system*. Journal of oral rehabilitation, 2012. **39**(9): p. 684-691.
153. Mizunuma, H., et al., *Numerical modeling and simulation on the swallowing of jelly*. Journal of texture studies, 2009. **40**(4): p. 406-426.
154. Bathe, K.-J. and G. Noh, *Insight into an implicit time integration scheme for structural dynamics*. Computers & Structures, 2012. **98**: p. 1-6.
155. Pauloski, B.R., et al., *Swallow function and perception of dysphagia in patients with head and neck cancer*. Head & neck, 2002. **24**(6): p. 555-565.
156. Dodds, W.J., *The physiology of swallowing*. Dysphagia, 1989. **3**(4): p. 171-178.
157. Martin, R.E., *A comparison of lingual movement in swallowing and speech production*. Vol. 2. 1991: University of Wisconsin--Madison.
158. Tasko, S.M., R.D. Kent, and J.R. Westbury, *Variability in tongue movement kinematics during normal liquid swallowing*. Dysphagia, 2002. **17**(2): p. 126-138.
159. Ilegbusi, O.J., et al., *Modeling airflow using subject-specific 4DCT-based deformable volumetric lung models*. Journal of Biomedical Imaging, 2012. **2012**: p. 4.
160. Ilegbusi, O.J., B. Seyfi, and R. Salvin, *Patient-specific model of lung deformation using spatially dependent constitutive parameters*. Mathematical and Computer Modelling of Dynamical Systems, 2014. **20**(6): p. 546-556.